

# A meso-scale computational approach to dynamic failure in concrete

THÈSE N° 5642 (2013)

PRÉSENTÉE LE 24 MAI 2013

À LA FACULTÉ DE L'ENVIRONNEMENT NATUREL, ARCHITECTURAL ET CONSTRUIT  
LABORATOIRE DE SIMULATION EN MÉCANIQUE DES SOLIDES  
PROGRAMME DOCTORAL EN STRUCTURES

ÉCOLE POLYTECHNIQUE FÉDÉRALE DE LAUSANNE

POUR L'OBTENTION DU GRADE DE DOCTEUR ÈS SCIENCES

PAR

Leonardo SNOZZI

acceptée sur proposition du jury:

Prof. E. Brühwiler, président du jury  
Prof. J.-F. Molinari, directeur de thèse  
Prof. P. Lura, rapporteur  
Prof. A. Muttoni, rapporteur  
Prof. F. Ragueneau, rapporteur



ÉCOLE POLYTECHNIQUE  
FÉDÉRALE DE LAUSANNE

Suisse  
2013





# Abstract

The aim of the present thesis is to provide a numerical tool for the mechanical modeling of dynamic failure in concrete. This widely used construction material is characterized by a non-linear failure behavior, which is consequently difficult to describe with macroscopic quantities. In order to grasp the mechanical damage response of this heterogeneous brittle material, our approach is based on a meso-mechanical point of view. The whole research work is, therefore, mainly focused on the understanding of the mechanisms that are linked with the material's heterogeneous composition. The advantage of this level of observation is that it allows to represent the most important concrete constituents (e.g. aggregates and cement paste), thus facilitating the physical identification of the material parameters of the model and of the mechanisms (interaction between matrix and inclusions) that characterize its constitutive behavior.

For this purpose we exploit the capabilities of a two-dimensional finite-element model. The onset of fracture is explicitly modeled using the well-known cohesive approach. We first investigate the dynamic tensile response of concrete specimens. Different simulations are carried out to assess the influence of aggregates properties on peak strength and dissipated fracture energy at different strain rates. The model aims to explain the strain-rate strengthening through structural effects. However, to capture the full extent observed experimentally, our results suggest that is not possible to discard the combination of inertial with material rate hardening mechanisms. Next, in order to account for crack-interactions as well as path dependent behavior, the model is enriched with the introduction of an explicit contact algorithm and a mode-dependent fracture energy. To demonstrate the capability of the proposed approach to provide accurate results, the model is first applied to two benchmark tests in masonry engineering. Afterwards, the developed framework is applied to reproduce dynamic compressive failure of meso-scale concrete samples. Simulations involving different strain rates and levels of lateral confinement are conducted. An energetic analysis shows that dissipation of energy through fracture and friction is an increasing function of the applied confinement and strain rate. Our results underline thus the importance of capturing frictional mechanisms, which appear to dissipate a raising amount of frictional energy with increasing strain and applied pressure.

Finally, a multi-scale computational framework is developed to up scale the obtained fine scale response to the coarse scale. The selected approach considers concrete macroscopically as being homogeneous and to behave linear elastically aside from the propagating cracks. The cohesive macroscopic tractions are however extracted from the response of meso-scale repre-

---

sentative volume elements, which are activated on the fly when a macroscopic discontinuity propagates. Parallel simulation shows the capability of the model to predict the structural response of a tested unit including the physical mechanisms occurring at the fine scale.

**Keywords:** numerical methods, dynamic fracture, cohesive zone, frictional contact, concrete, meso-scale, parallel computing

# Résumé

Ce mémoire de thèse a pour objectif de développer un outil numérique pour la modélisation mécanique du béton (sous sollicitation dynamique). Ce matériau couramment utilisé dans la construction est caractérisé par un comportement non linéaire à la rupture. De plus, ce matériau fragile est très hétérogène conduisant à une délicate description macroscopique de sa réponse mécanique. Dans ce travail, le point de vue mésoscopique du comportement du béton a été adopté. L'ensemble de l'étude s'est focalisé principalement sur la compréhension des phénomènes liés à la composition hétérogène du matériau. L'avantage de ce niveau d'observation est de représenter les constituants les plus importants du béton (granulats et matrice cimentaire) pour faciliter l'identification physique des paramètres matériels du modèle et la description des mécanismes (interaction entre la matrice et les inclusions) caractérisant son comportement constitutif. La réponse mécanique du béton a été simulée dans un cadre bidimensionnel et la fissuration est explicitement modélisée en utilisant la méthode des éléments cohésifs.

Une première partie de ce travail a été consacrée à la réponse dynamique d'échantillons en béton sujets à une traction simple. Différentes simulations ont été effectuées pour évaluer l'influence des propriétés des granulats sur la résistance du béton et l'énergie dissipée par la variation de la vitesse de chargement. Ces simulations ont permis d'expliquer le durcissement du béton produit par les effets de vitesse à travers un phénomène structural (microfissuration diffusée). De plus, les résultats ont montré que la combinaison entre les effets d'inertie et les mécanismes de durcissement du matériau est inéluctable.

Dans la seconde partie de ce mémoire, le modèle a été enrichi par l'introduction d'un algorithme de contact et d'une énergie de rupture dépendant du mode d'ouverture pour prendre en compte les interactions entre les fissures et de la dépendance du chemin suivi. Cette nouvelle approche numérique a d'abord été validée sur deux tests de référence en génie de la maçonnerie. Par la suite, le comportement dynamique du béton en compression a été reproduit. Différents niveaux de vitesse de chargement et de pression de confinement latéral ont été menés. L'analyse dynamique a montré que la dissipation d'énergie obtenue par frottement et par la rupture est une fonction croissante du niveau de confinement et de la vitesse de déformation. Ces résultats ont révélé l'importance d'inclure les mécanismes de frottement dans le modèle.

Enfin, dans la troisième partie de ce travail, un modèle d'homogénéisation numérique a été développé pour transférer, au niveau macroscopique, la réponse mécanique obtenue à l'échelle mésoscopique. Dans cette approche, hors endommagement, le béton est considéré comme

---

étant macroscopiquement homogène (avec un comportement linéaire élastique). De plus, la propagation d'une discontinuité macroscopique est contrôlée par l'activation dynamique de volumes élémentaires représentatifs, dans lesquels se propagent les fissures. A partir de ce nouveau modèle, un calcul parallèle a été réalisée et a démontré ainsi la capacité de cette approche à prédire la réponse mécanique d'une structure tout en incluant les mécanismes physiques à l'échelle mésoscopique.

**Mots Clés** : méthodes numériques, fissuration dynamique, approche cohésive, contact frottant, béton, échelle mésoscopique, calcul haute performance

# Acknowledgements

This research work has been carried out at the computational solid mechanics' laboratory (LSMS) of the École Polytechnique Fédérale de Lausanne (EPFL) under the supervision of Prof. Jean-François Molinari. First and foremost, I would like to thank my advisor for his valuable guidance and having offered me the opportunity to realize this research work. I also appreciated his enthusiasm, passion and energy, which contributed to the thesis' success. I also appreciated the independence and trust that he accorded to me during the entire investigation process.

I own special acknowledgment to Prof. Eugen Brühwiler, president of the defense jury, as well as all other thesis committee members: Prof. Aurelio Muttoni, Prof. Pietro Lura and Prof. Frédéric Ragueneau.

During the four years spent at the EPFL, I benefit to work in a privileged and dynamic environment such as the LSMS. This lab has grown and evolved considerably since my arrival. I had the opportunity to be in a multi-cultural milieu and to take advantage of the numerous visiting researchers hosted in this lab. Among them I especially wish to thank Prof. Fabrice Gatuingt, with whom I could start a fruitful collaboration and whose generous advices contributed significantly to this investigation.

I am in debt with Nicolas Richart, for the time and patience he dedicated to me, as well as with Guillaume Anciaux, without both them the computational development of this thesis would have been almost impossible. I also want to thank all my colleagues for their friendship and advices.

I own special acknowledgement to the Swiss National Foundation for its financial support. In addition, a significant contribution was brought to me from my friends, which I all wish to thanks for their friendship and support.

Finally, I am very grateful to my family and partner Giulia, for their presence and support and for what they have transmitted to me during my life, which has shaped my character and allowed me to overcome the difficulties encountered during my studies.



This work is dedicated to the loving memory of my father Giorgio





# Contents

<b>Abstract (English/Français)</b>	<b>iii</b>
<b>Acknowledgements</b>	<b>vii</b>
<b>List of figures</b>	<b>xiii</b>
<b>List of tables</b>	<b>xix</b>
<b>Introduction</b>	<b>1</b>
<b>1 Introduction</b>	<b>1</b>
1.1 Context . . . . .	1
1.2 Challenges and objectives . . . . .	2
1.3 Computational approach . . . . .	3
1.4 Outline of the chapters . . . . .	5
<b>2 Modeling of concrete</b>	<b>7</b>
2.1 Experimental characterization . . . . .	7
2.2 Macro and meso modeling of concrete . . . . .	9
2.2.1 Damage models . . . . .	10
2.2.2 Plasticity Models . . . . .	11
2.2.3 Particle (lattice) models . . . . .	12
2.2.4 Finite Element with fracture capability . . . . .	13
2.3 Meso-structure . . . . .	14
2.3.1 Mesh-generator . . . . .	15
<b>3 Numerical framework</b>	<b>17</b>
3.1 Fundamental concepts of the Finite-Element Method . . . . .	17
3.1.1 Strong form: governing equations . . . . .	17
3.1.2 Weak form and discrete formulation . . . . .	20
3.1.3 Time integration . . . . .	20
3.2 The cohesive zone approach . . . . .	22
3.2.1 Origins of the cohesive approach . . . . .	22
3.2.2 Intrinsic and extrinsic cohesive approach . . . . .	24
3.2.3 Xu and Needleman exponential cohesive law . . . . .	25

## Contents

---

3.2.4	Camacho-Ortiz linear irreversible cohesive law . . . . .	26
3.2.5	Formulation involving an interface . . . . .	28
<b>4</b>	<b>Influence of the meso-structure in dynamic tensile loading</b>	<b>31</b>
4.1	Introduction . . . . .	31
4.2	Meso-structure characteristics . . . . .	32
4.2.1	Measure of damage . . . . .	33
4.3	Results . . . . .	34
4.3.1	Geometry and boundary conditions . . . . .	34
4.3.2	Effect of mesh size, geometry and material parameters . . . . .	35
4.3.3	Soft vs. Hard aggregates and strain rate effect . . . . .	39
4.3.4	Ordered vs disordered meso-structure . . . . .	43
4.3.5	Influence of aggregate's size . . . . .	46
4.4	A rate-dependent cohesive law . . . . .	48
4.5	Additional analysis on rate dependency . . . . .	51
4.5.1	Extended material parameters and meso-structure . . . . .	52
4.5.2	Influence of the specimen size . . . . .	53
4.5.3	Loading rate effect and dissipation . . . . .	56
4.6	Discussion . . . . .	58
<b>5</b>	<b>Mixed mode loading</b>	<b>61</b>
5.1	Introduction . . . . .	61
5.2	Modified cohesive law for mixed mode loading . . . . .	62
5.2.1	Work of separation under combined normal shear loading . . . . .	64
5.3	Contact enforcement . . . . .	66
5.3.1	Frictional impact . . . . .	68
5.3.2	Coupling with cohesive zone model . . . . .	69
5.4	Numerical validation . . . . .	71
5.4.1	Application to a masonry wallette . . . . .	71
5.4.2	Application to a masonry wall . . . . .	75
5.5	Conclusions . . . . .	78
<b>6</b>	<b>Compressive behavior of concrete under dynamic loading</b>	<b>79</b>
6.1	Meso-scale geometry . . . . .	79
6.1.1	Mesh generation and aggregate distribution . . . . .	79
6.1.2	Material parameters . . . . .	81
6.2	Uniaxial compressive loading . . . . .	81
6.2.1	Initial and boundary conditions . . . . .	81
6.2.2	Identification of model's interface parameters through simulations . . . . .	82
6.2.3	Rate effect . . . . .	84
6.3	Influence of lateral confinement . . . . .	86
6.4	Discussion and Conclusions . . . . .	90

<b>7 Multi-Scale modeling</b>	<b>93</b>
7.1 Multi-Scale framework . . . . .	95
7.1.1 Macroscopic modeling . . . . .	95
7.1.2 Meso-scale formulation . . . . .	96
7.2 Upscaling . . . . .	106
7.2.1 Computational aspects . . . . .	109
7.3 Numerical results . . . . .	110
7.3.1 DCB specimen . . . . .	110
7.3.2 Push-off application . . . . .	113
7.3.3 Perspectives: application to a reinforced concrete beam . . . . .	116
7.4 Conclusions . . . . .	117
<b>8 Conclusions and Outlook</b>	<b>119</b>
8.1 Summary and conclusions . . . . .	119
8.2 Perspectives . . . . .	122
<b>Bibliography</b>	<b>140</b>
<b>Curriculum Vitae</b>	<b>141</b>



# List of Figures

2.1	Characteristic behavior of concrete under (a) tension and (b) simple compression.	8
2.2	Examples of different meso-structure geometries: (a) obtained with a Voronoi mesher, while (b) and (c) are generated according to a grading curve with circular and polygonal inclusions respectively.	15
3.1	Lagrangian deformation of the body $B_0$ .	18
3.2	Body $B_0$ .	19
3.3	Debonding process between the atoms at the crack tip.	22
3.4	Cohesive approach and integration path for the $\mathcal{J}$ integral.	23
3.5	(a) Intrinsic and (b) extrinsic approach.	24
3.6	Needleman exponential cohesive law [Xu 93].	25
3.7	Camacho-Ortiz linear decreasing cohesive law [Camacho 96].	26
3.8	Representation of a crack with a cohesive zone fictitious crack tip subjected to far field loading $\sigma_\infty$ .	27
3.9	Body $B_0$ with a cohesive surface $S_0$ .	29
4.1	Schematics of the generation of concrete's meso-structure.	33
4.2	Boundary (left) and initial (right) conditions.	35
4.3	Macroscopic peak strength $\sigma_{max}$ [MPa] versus average element size $l_m$ [mm] for (a) $\dot{\epsilon} = 10\text{s}^{-1}$ and (b) $\dot{\epsilon} = 1000\text{s}^{-1}$ (with soft aggregates).	36
4.4	(a) Mesh of the pre-cracked specimen. (b) Evolution of the macroscopic peak strength $\sigma_{max}$ varying $\sigma_c$ . The square and triangular symbols are located in the plot with the same cohesive length as for soft respectively hard aggregates.	37
4.5	Pre-cracked specimen with variable width.	38
4.6	(a) Macroscopic normalized peak strength $\sigma_{max}$ versus specimen with $h$ [m] and (b) specimens with double and quadruple size.	39
4.7	Concrete meso-geometry with 79 aggregates (left). Zoom of the corresponding finite-element mesh (right).	39
4.8	Macroscopic stress-strain ( $\sigma - \epsilon$ ) comparison between hard and soft aggregates: (a) at low strain rate ( $\dot{\epsilon} = 10 \text{ s}^{-1}$ ) and (b) at high strain rate ( $\dot{\epsilon} = 1000 \text{ s}^{-1}$ ).	40

## List of Figures

---

4.9	(a) Macroscopic peak strength $\sigma$ [MPa] – strain rate $\dot{\epsilon}$ [ $s^{-1}$ ] for soft and hard aggregates for a rate independent law. (b) Comparison with experimental values extract from [Brara 06], which itself has used the following experimental data: [Brara 99, Ross 95, Birkimer 68, Toutlemonde 94, Mc Vay 88, John 92] (note that the vertical axis is normalized by the static strength). . . . .	41
4.10	Crack propagation in the mesh: at low strain rate for hard (a) and soft (b) aggregates, at high strain rate (c) just one zoom is showed (crack nucleation occurs everywhere in the matrix independently of aggregate type). . . . .	41
4.11	Damage on aggregates, matrix and interfaces vs. tensile-strain. Comparison between soft and hard aggregates: (a) low strain rate, (b) high strain rate. . . . .	42
4.12	Different meso-structures: (a) uniform aggregates (U), (b) rotated aggregates ( $U_{Rot}$ ) and c) completely random (R). . . . .	44
4.13	Stress-strain diagrams obtained for the three different meso-structures under (a) low and (b) high strain rate. . . . .	45
4.14	Dissipated fracture energy for the matrix (in green) and interfaces (in red) vs. tensile strain. Comparison between specimens with the three different meso-structures. . . . .	45
4.15	Specimens with different mean size of aggregates: (a) 66 aggregates, (b) 297 aggregates and (c) 1198 aggregates. . . . .	46
4.16	Stress-strain diagrams obtained for the different aggregate sizes under (a) low and (b) high strain rate. . . . .	47
4.17	Dissipated fracture energy vs. tensile-strain. Comparison between specimens with 66, 297 and 1198 aggregates: (a) at low strain rate and (b) at high strain rate. . . . .	47
4.18	Two rate-dependent cohesive laws: (a) generalized cohesive law with crack opening displacement as a function of crack opening rate, (b) cohesive stress and crack opening are both function of strain rate. . . . .	49
4.19	(a) Macroscopic peak strength $\sigma$ [MPa] – strain rate $\dot{\epsilon}$ [ $s^{-1}$ ] for soft and hard aggregates for a rate dependent cohesive law. (b) Comparison with experimental values extract from [Brara 06], which itself has used the following experimental data: [Brara 99, Ross 95, Birkimer 68, Toutlemonde 94, Mc Vay 88, John 92] (note that the vertical axis is normalized by the static strength). . . . .	50
4.20	Experimental stress-displacement curves for static, SHB and Modified SHB tests (from [Weerheijm 07]). . . . .	52
4.21	Two different meso-structures generated with the same aggregates size distribution. . . . .	52
4.22	Large vs small size of the specimen. . . . .	53
4.23	Influence of the specimen size on the stress-strain curves: (a) $\dot{\epsilon} = 1 s^{-1}$ (b) $\dot{\epsilon} = 10 s^{-1}$ . . . . .	54
4.24	Influence of the specimen size on the dissipated fracture energy: (a) total energy and (b) normalized energy. . . . .	55
4.25	Influence of the specimen size on the fracture path: a/ $\dot{\epsilon} = 1 s^{-1}$ b/ $\dot{\epsilon} = 100 s^{-1}$ . . . . .	55
4.26	Rate effect in tension for the two meso-structures depicted in Figure 4.21: (a) Figure 4.21a and (b) Figure 4.21b. . . . .	57

4.27 Influence of the meso-structure on the dissipated fracture energy for different strain rates for the two different meso-structures: (a) Figure 4.21a and (b) Figure 4.21b. . . . .	57
4.28 Influence of the loading rate on the final cracking for the meso-structure depicted in Figure 4.21a: (displacement has been magnified by a factor of 100): (a) $\dot{\epsilon} = 0.1 \text{ s}^{-1}$ , (b) $\dot{\epsilon} = 100 \text{ s}^{-1}$ . . . . .	58
5.1 Cohesive zone loaded with two different paths leading potentially to two distinct values of dissipated energy. . . . .	63
5.2 Cohesive traction in (a) normal direction and (b) tangential direction (with $\beta > 1$ ). 64	64
5.3 (a) Cohesive zone loaded under a constant angle $\alpha$ as in [Von den Bosch 05] and (b) resulting dissipated work as function of the loading angle expressed in units of $G_{c,I}$ (with $\kappa > 1$ ). . . . .	65
5.4 Interface non proportionally loaded: (a) first in normal direction until $\Delta_{n,max}$ and then broken in shear and (b) first in tangential direction until $\Delta_{t,max}$ and then broken in normal direction as in [Von den Bosch 05]. . . . .	65
5.5 (a) Work of separation when loading first in (a) normal direction and (b) in tangential direction respectively expressed in units of $G_{c,I}$ (with $\kappa > 1$ ). . . . .	66
5.6 (a) Impact-time resolved exactly and (b) approximation of the DCR. . . . .	67
5.7 Shear stress-tangential opening displacement relationship for a growing crack in mode II with full onset of friction. . . . .	69
5.8 Adopted shear stress-tangential opening displacement relationship for a growing crack in mode II with increasing frictional capability. . . . .	70
5.9 (a) Experimental test setup of the wallette [courtesy of Beyer [Beyer 10], [Beyer 11]] and (b) corresponding finite-element mesh, corresponding to one half of the experimental setup (all dimensions in mm). . . . .	71
5.10 Shear stress plotted against shear displacement: (a) for different values of $\sigma_c$ ( $G_{c,I}$ kept constant) and (b) for different values of $G_{c,I}$ ( $\sigma_c$ kept constant). . . . .	73
5.11 Regularization of damping on (a) the stress-displacement curve and (b) the amount of kinetic energy in the system. . . . .	74
5.12 Shear stress plotted against shear displacement: comparison between experimental envelope (dotted gray area) and simulation (continuous red line). . . . .	74
5.13 Experimental setup of the masonry wall tested in [Ganz 84] (all dimensions in mm). . . . .	75
5.14 Adopted finite-element mesh. . . . .	76
5.15 Comparison of the horizontal force-displacement curves for the masonry wall between the finite-element analysis (continuous red line and dotted blue line) and the experimental results (dashed gray line) of Ganz [Ganz 84]. . . . .	77
5.16 Deformed mesh configuration (at $u = 14.5 \text{ mm}$ ) for shear velocity of (a) $0.05 \frac{\text{m}}{\text{s}}$ and (b) $0.5 \frac{\text{m}}{\text{s}}$ (magnification factor 25). . . . .	77
6.1 (a) Computed cumulated aggregates size distribution of the concrete meso-structure (b). . . . .	80

## List of Figures

---

6.2	Boundary and initial conditions for specimen loaded in compression. . . . .	82
6.3	(a) Influence of the $\beta$ parameter on the compressive stress-strain behavior of concrete (for $\kappa = 10$ ) and (b) influence of $\kappa$ (with $\beta = 3.5$ ) for $\dot{\epsilon} = 1 \text{ s}^{-1}$ . . . . .	83
6.4	(a) comparison with empirical model of [Fernández Ruiz 07] and (b) asymmetric tensile/compressive behavior of concrete ( $\dot{\epsilon} = 1 \text{ s}^{-1}$ ). . . . .	84
6.5	Stress-strain response for different strain rates under compressive loading. . . . .	85
6.6	Influence of strain rate on the crack path in compression: (a) $\dot{\epsilon} = 1 \text{ s}^{-1}$ , (b) $\dot{\epsilon} = 100 \text{ s}^{-1}$ . Note that the displacement field has been magnified by two different factors: 4 in (a) and 2 (b). . . . .	85
6.7	(a) Dissipated fracture energy and (b) dissipated frictional work for different loading rates. . . . .	86
6.8	(a) Influence of confining pressure on the stress-strain behavior ( $\dot{\epsilon} = 1 \text{ s}^{-1}$ ) and (b) experimental results of [Sfer 02]. . . . .	87
6.9	(a) Dissipated fracture energy and (b) frictional work for $p_x = 0, 4.5, 9$ and $12 \text{ MPa}$ ( $\dot{\epsilon} = 1 \text{ s}^{-1}$ ). . . . .	88
6.10	Deformed specimens for confinement pressures of (a) $4.5 \text{ MPa}$ and (b) $12 \text{ MPa}$ . Displacement has been magnified by a factor of 5. . . . .	89
6.11	(a) Maximal cluster length normalized over specimen size $h$ and (b) number of cracks for $p_x = 0, 4.5, 9$ and $12 \text{ MPa}$ . The length at which softening starts, represented by circles on graph (a), does not depend on the amount of confinement. . . . .	89
7.1	(a) parallel computational framework exploited for multi-scale simulations (the master nodes queues the jobs distributing them between the cluster nodes). (b) Homogenization scheme. . . . .	94
7.2	Deformed RVE showing a characteristic meso-structure. The numbers from 1 to 4 represent the index of the corner nodes. . . . .	96
7.3	Schematic of a two-dimensional RVE. . . . .	98
7.4	(a) Geometry of the meso-structure with the selected RVE regions and (b) resulting macroscopic Young's modulus for homogenized elastic behavior as a function of edge size. TCB, PBC and DBC stand for traction, periodic and displacement BCs respectively. . . . .	99
7.5	(a) stress-strain behavior for different RVE-sizes and (b) homogenized stress-displacement relationship. . . . .	101
7.6	Crack path for three RVEs: edge size of (a) $25$ , (b) $50$ and (c) $75 \text{ mm}$ (displacement has been magnified by a factor of 20). . . . .	101
7.7	Schematic of a RVE crossed by a crack with applied aligned PBC on lateral faces. . . . .	103
7.8	One dimensional bar discretized with two different meshes: (a) with inter-element boundaries aligned with the loading direction and (b) with interfaces oriented at an angle of $30^\circ$ . The thick red line indicates the location of the discontinuity. . . . .	104



7.9	Crack path (displacement magnified by a factor of 15) for the RVE: (a) interface aligned with loading direction, (b) interface at 30° with aligned PBC (c) interface at 30° and classical PBC. . . . .	104
7.10	(a) Extracted TSL from the three RVEs of Figure 7.9 and (b) computed regression line for the RVE depicted in Figure 7.9b . . . . .	105
7.11	Homogenized macroscopic stress (traction) versus (a) meso-scale displacement and (b) homogenized opening displacement of Equation 7.14. The dot ( $\sigma_o$ ) represents the status in the RVE at cohesive insertion. . . . .	106
7.12	Cracked macro-body with crack tip normal $N$ and corresponding rotated RVE .	107
7.13	Geometry (all units in mm) and boundary conditions of the DCB test . . . . .	110
7.14	DCB specimen for the virtual experiments: (a) Macroscopic mesh for the multi-scale simulation and (b) adopted geometry for the direct numerical simulation. . . . .	111
7.15	Developed crack path in the DCB specimen (displacement has been magnified by a factor of 80). Comparison between (a) the multi-scale cohesive solution and (b) the DNS. . . . .	112
7.16	Deformed configuration (displacements have been magnified by a factor of 15) of two RVEs corresponding to two different integration points located: (a) near the crack tip (circle 1 in Figure 7.15a) and (b) more distant (circle 2 in Figure 7.15a) respectively. . . . .	112
7.17	Comparison of the vertical force-displacement relationships for the multi-scale scheme and the DNS . . . . .	113
7.18	(a) Geometry of the tested unit by Sagaseta <i>et al.</i> [Sagaseta 11] with diameter of reinforcement bars (all dimensions in mm). (b) Corresponding coarse-scale mesh for the multi-scale analysis (the red dashed lines represent stirrups that have been modeled with bar elements). . . . .	114
7.19	Macroscopic deformed mesh configuration and shearing in a RVE located on the vertical macroscopic crack. . . . .	115
7.20	Comparison of the shear stress-displacement curves for the push-off test between the FE <sup>2</sup> analysis (dotted line) and the experimental results (continuous red line) of Segaseta [Sagaseta 11]. . . . .	116
7.21	A possible future application of interest. Beam geometry of the tested unit by [Leonhardt 62] with boundary conditions (all dimensions in mm). . . . .	117



## List of Tables

4.1	Summary of fracture material properties. . . . .	34
4.2	Cohesive zone lengths of the concrete meso-scale model. . . . .	36
4.3	Interface length between aggregates and matrix for the three different specimens. . . . .	48
4.4	Strength, fracture energy and dynamic/static ratio for these values for concrete at different loading rates (from [Weerheijm 07]). . . . .	51
4.5	Material properties of concrete. . . . .	53
5.1	Material properties of the masonry bricks. . . . .	72
5.2	Cohesive properties for interface elements. . . . .	72
6.1	Material properties of the concrete's components. . . . .	81
6.2	Cohesive properties and selected parameters for the interfaces. . . . .	81



# 1 Introduction

## 1.1 Context

Concrete is a widely used material around the world in civil and industrial structures. The constitutive behavior of this construction material is often described by macroscopic models that assume concrete as being homogeneous. However, this assumption entails the introduction of complex modeling variables into the description in order to accurately reproduce the non-linear behavior that concrete shows during failure.

Another possibility is to consider concrete at a lower scale of observation, where the heterogeneous structure can be explicitly represented. The advantage of this approach is that it allows monitoring the interactions between constituents, which finally originate the observed macroscopic response. In addition, the explicit representation of the concrete heterogeneities facilitates the characterization of the dynamic response of concrete. During its life a structure might be indeed exposed to dynamic solicitations (either accidental or intentional). Relevant examples include nuclear power plants, which must be designed to sustain terrorist explosions or impact of a falling aircraft, and common civilian structures, which can be subjected to violent solicitations during earthquakes.

Besides those catastrophic events, the kinematic aspects should be taken into account also during failure modes that might originate under static loads, but that entail rapid crack propagation (the dynamic aspects of damage are often evident by the noise accompanying the failure process).

Since failure events are difficult to predict, it is important to develop analytical and numerical models to understand them better. This could lead to better design of structures to prevent failure and make them more resistant against such events. An accurate modeling provides indeed a complementary analysis tool to the verification through design codes, which sometimes fail to provide adequate guidelines to assess the load carrying capacity of a structural member to withstand unexpected situations, especially under extreme dynamic loading.

### 1.2 Challenges and objectives

Failure of concrete is characterized by complex phenomena that originate at the micro-scale. Nucleation of cracks takes place at the weakest links (between matrix and aggregates) as a result of the applied solicitations. As this process occurs, micro-cracks are originated at different locations (seemingly random) within the material. The meso-structure together with the line forces in statics and stress wave's network in dynamics constitute the main ingredients of the nucleation phase. For instance coalescing cracks respect the arrangement of the (inclusions) geometry. The micro-cracks coalescence leads to cracks that, in general, tend to open following the principal direction of loading (perpendicularly to the maximum tensile stress direction). However, they do not necessarily continue to open in the direction perpendicular to the crack plane, since, as a consequence of cracking, the distribution of stresses is affected when comparing to the un-cracked regime causing the material to behave more anisotropically. Besides this, it should also be pointed out that cracks with different orientations might propagate within the material, since the motion of a crack alters the stress field leading to dependence between propagating crack direction and surrounding cracks. Additionally, the heterogeneous composition increases this effect.

As a consequence, the stress state can produce parallel motion between cracks. The relative displacement, experienced by the opposite surfaces of the crack, leads thus the asperities that characterize the shape of the crack surface to intercept the opposite ones. Therefore cracks are required to transmit, apart from normal forces, shear forces. This mechanism that causes shear stresses to develop if any relative displacement is applied, is known as aggregate-interlock [Walraven 80].

In addition, the deformation rate that the material undergoes during the damaging process highly affects the micro-structural evolution. Experimental observation indicates that concrete is bounded with a higher dissipation of energy with increasing rate of loading. It is therefore important to understand the dynamic evolution of the damage mechanisms, which govern the behavior of the material. The characterization of the rate-dependent behavior of concrete and the evolution of the stress state presents a crucial point if the safety of industrial or civil structures needs to be assessed against the dynamic loadings produced by extreme conditions such as earthquakes, explosions or accidental collisions (*e.g.* [Brühwiler 90]). A fine scale level of observation allows us to avoid the introduction of a dynamic increase factor (a fit parameter) directly into the macroscopic model.

All the outlined aspects need a careful treatment in order to reach an accurate description of such level of complexity. Aside from analytical models, advances in computational mechanics and the increase of available computational power offer a rigorous tool to tackle these issues. However, several challenges need to be addressed within the development of a computational model. This includes the modeling of:

- Time-dependent non-linear evolution of the meso-structure.

- A dense network of micro-cracks interacting with the complex meso-structural composition.
- A frictional contact algorithm to account for the interactions between multiple propagating cracks.

In this thesis we are choosing to evaluate the constitutive behavior of concrete starting from a meso-mechanical point of view. This should allow us to predict macroscopic behavior, avoiding the use of complex phenomenological laws to describe the material constitutive response. Indeed, the modeling at the meso-scale can in principle be achieved by representing more fundamental physical mechanisms, which are strictly related to the micro-structural details of the material composition. Moreover, the constitutive behavior extracted at this scale needs to be transferred at the macro-scale to simulate the damaging process at a bigger scale. We propose to couple multiple time and length scales using a multi-scale framework that resorts to computational homogenization. Our objective is to provide an accurate numerical solution while preserving an efficient use of computational resources.

We will limit our analysis to a concrete with conventional material properties in a two dimensional plane-strain setting.

### 1.3 Computational approach

The objective of this research work is to develop a computational model for concrete behavior avoiding the use of phenomenological macroscopic constitutive laws. At the structural level concrete is often considered as a homogeneous material. However, to reproduce the non-linear behavior of concrete the adopted constitutive models need to have recourse to phenomenological modeling such as (visco)-plasticity and/or continuum damage formulation.

To avoid such assumptions, we have started our investigation from a biphasic approach, which represents mortar and aggregates. At this level it is possible to observe and explicitly model the interactions between these two constituents that lead to the characteristic behavior of this construction material. Concrete can be thus analyzed at the mesoscopic scale, which is an intermediate scale situated in between the micro-mechanical observation of the phenomena taking place in the cement paste and the macroscopic assumption of concrete homogeneity. Commonly, two main computational approaches are employed for the meso-modeling of concrete. The first class is represented by discrete approaches, commonly referred as lattice models. The particularity of this popular method, is to represent the material through a network of beams (or lattice) relating discrete points. Those beams are thus responsible for the forces that generate between the material points. This implies that the constitutive response of the lattice model is defined by the behavior of the beams. Though able to provide good estimates of concrete behavior for several loading conditions, in this thesis we have

not selected this methodology since it introduces a non physical length scale in the material description (lattice beam spacing between fictitious particles).

This problem disappears in the second class of methods, which is represented by finite element models with fracture capability. The bulk material is there represented by means of classical elements, while cracking is explicitly represented having recourse to cohesive zone theories. With this approach cracks generate from the nucleation and coalescence of micro-cracks. We indeed believe that most sources of the non-linear behavior, which concrete displays, can be traced back to an accurate modeling of the cracks and to the correlated mechanisms. For instance, depending on the applied loading condition, a frictional contact algorithm might be necessary to model the interaction between two cracked surfaces. In addition, to be able to reproduce the strengthening effect, that concrete shows when subjected to increasing loading velocities, a dynamic framework has been selected. More precisely, the coupling between cohesive zone modeling and the impenetrability constrain has been performed within an explicit dynamics scheme.

The selected meso-mechanical model enables us to physically identify the material parameters. However, a disadvantage of this technique is that to achieve a precise representation of the aggregates a fine-mesh is needed, which is bounded with high computational costs. There is thus a need to up scale the constitutive behavior extracted at this scale to the coarse-scale. Computationally, there are different approaches to model the behavior of materials that are involving processes at multiple spatial scales, or temporal scales simultaneously. As a result different techniques have been developed to tackle such problems.

A common method, that has been widely employed to analyze the behavior of complex structures, resorts to the hierarchical approach. This approach is characterized by the sequential modeling at different time and length scales. The relationship extracted from a model is then injected into the next model to compute the global response (usually having recourse to finite element methods). The hierarchical approach allows thus for a global-local analysis. The obtained constitutive behaviors are, therefore, characterized by parameters that are chosen according to the selected phenomena that need to be included in the formulation. This method is attractive since it can predict well the behavior in many cases.

However, one of the drawbacks of this approach is that it requires a high number of parameters to model highly heterogeneous materials such as concrete. This implies that it becomes difficult to clearly identify the parameters from simple experiments. Another problem is that this coupling scheme supposes a strict separation of scales.

A second class of methods is represented by the family of homogenization techniques, which resorts to the simultaneous presence of both micro and macro-scale within the same simulation. The incorporation of the micro-structure within the formulation allows the incorporation of relevant information in the modeling, with the aim to describe as accurately as possible the interactions at the micro-level.

Two main (computational) classes can be distinguished in homogenization analysis. In both approaches it is assumed that the scales are separated, but the formulations are conceptually different. The first one is known as asymptotic homogenization. This approach applies



microscopic fields as expansion of the macroscopic displacement and stress fields. However, this approach is usually restricted to simple microscopic models and geometries. Another drawback of asymptotic mean field is that it requires two completely separated length scales for the treated problems. However, industrial applications often do not allow this hypothesis. This is also the case in concrete where the size of the inclusions might not be negligible compared to the dimensions of the structure (depending on the specimen size which is analyzed).

On the other hand, the second class, which is based on the notion of so-called unit-cell or Representative Volume Element (RVE), allows a higher complexity of the micro-structural mechanical behavior of the cell. The RVE size is chosen according to the heterogeneous composition of the micro-structure and is much smaller than the dimensions of the macro-structure.

The idea of homogenization is to introduce two computational scales that are resolved. The first scale is the so-called macro-scale which represents the whole structure of interest. The second one contains the micro-structure and is strictly linked with the integration points of the first one. It is used to extract the constitutive behavior for the macro-scale, and it thus replaces the classical constitutive laws. We will follow this second class of approach.

### 1.4 Outline of the chapters

The thesis is structured as follows.

At first (Chapter 2), a brief review of the experimental behavior of concrete and of the available computational tools to simulate its behavior are presented. Moreover, we describe the heterogeneous composition of concrete, which represents an important feature in the modeling of this material and one that is increasingly taken into account in current research.

The third chapter is dedicated to the description of the chosen numerical framework used. The finite element method, which represents the general skeleton, and the cohesive approach, which handles the fracture process, are described.

Chapter 4 presents a first application on a meso-scale concrete specimen. Samples are subjected to tensile loading under different strain rates. In addition, we focus on different distributions of aggregates, in their mechanical properties and sizes showing the influence of these factors on peak strength and dissipated fracture energy.

Mixed mode loading is tackled in Chapter 5. In this chapter we present the coupling between the cohesive approach and a contact algorithm to prevent penetration of the generated cracked surfaces. The methodology includes a novel initially rigid extrinsic traction separation law, which enables us to define two separate values for the dissipated fracture energy, in mode I and II. The method is then validated by comparing the numerical results to experimental data (recorded in masonry engineering) at the meso-level and structural level.

In Chapter 6 the method is applied to meso-scale concrete specimens subjected to compres-

## **Chapter 1. Introduction**

---

sive loading. The chapter focuses on the influence of lateral confinement on the response and provides comparison with available experimental data on triaxial loading. The influence of strain rates is considered too.

The multi-scale dynamic framework is finally discussed in Chapter 7. It reports a description of the adopted technique, which couples cohesive macroscopic fracture modeling with meso-scale failure behavior (in a  $FE^2$  settings). The applicability of the proposed framework is illustrated by means of a numerical example.

The last chapter states the conclusions that can be drawn from this research work and proposes research perspectives.

## 2 Modeling of concrete

This chapter focuses on the meso-scale representation of concrete. More precisely, the purpose of this section is to underline the importance of including an explicit description of the material's heterogeneities into the model. Indeed, this level of observation enables to model the influence of the inclusions properties on the overall behavior, which emerges from experimental observations with different concrete mixtures.

The chapter is divided as follows. The first section is devoted to a brief description of the experimental settings that are commonly adopted to characterize concrete behavior and thus to extract the relevant macroscopic material properties. Afterwards, a review of existing numerical models for concrete is presented. A comparison between approaches, that includes those in which information about the heterogeneous composition are comprised and those that consider the material as being homogeneous, is provided. This leads to a more detailed description of some characteristics of the adopted meso-mechanical numerical framework (which is further described in Chapter 3).

### 2.1 Experimental characterization

The stress-strain relationship of concrete is characterized by an asymmetric behavior between tension and compression. This can be extracted from different experimental tests; ranging from uniaxial compression or tension, triaxial compression, cyclic loading, dynamic loading, . . . From the experiments carried out under quasi-static regime it is possible to obtain the elastic properties of concrete, *i.e.* tensile  $f_t$  and compressive strength  $f_c$ , Young's modulus  $E$  and Poisson's ratio  $\nu$ . Dynamic tests (*e.g.* split Hopkinson bar) are performed to investigate the dynamic mechanical response of concrete. Experimental data show indeed a rate effect on strength, and on the dissipated fracture energy, in the high loading rate regime. Typically, dynamic tests provide increase factors that quantify the raise in strength and dissipated fracture energy of concrete subjected to high strain rates.

There are various tests to obtain the tensile strength of concrete, which is approximately ten times lower than the one in compression. A first possibility is given by direct tensile test

## Chapter 2. Modeling of concrete

(e.g. [Toutlemonde 94]).

The direct test consists in loading a concrete sample in its axial direction under traction. Due to the difficulties to properly attach the specimen to the loading machine (guaranteeing a uniform stress distribution) and the brittle post-peak behavior of concrete, it is a difficult test to achieve. On the contrary, indirect tests are simpler to achieve. Commonly the Brazilian (for instance [Fairhurst 64]) and the three points bending test (for instance [Monteiro 93]) are performed. In addition, in those experiments it is easier to measure other quantities, such as the dissipated fracture energy. The specimen in the bending test is indeed notched allowing the propagation of a clear single crack.

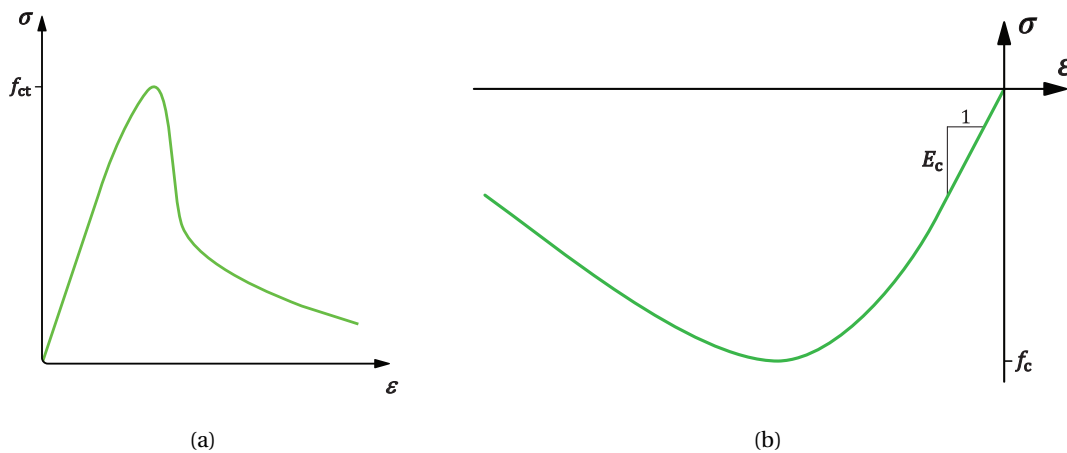


Figure 2.1: Characteristic behavior of concrete under (a) tension and (b) simple compression.

The compressive behavior is recorded through a simple direct compression test (e.g. [Monteiro 93, Sfer 02]). The compressive strength is one of the main characteristic of concrete. Usually experiments are performed 28 days after casting of the samples. We illustrate the constitutive behavior by means of a typical response illustrated in Figure 2.1b. At early stage of loading (30-40 % of  $f_c$ ) concrete behaves linear elastically. Then micro-cracks nucleate and the response becomes non-linear. The micro-cracks align parallel to the loading direction in the proximity of the peak strength. This phase is followed by a non-linear softening (“ductile”) with subsequent additional dilatation of the sample.

It should be pointed out that the applied boundary conditions highly influence the concrete response. The specimen response is, indeed, sensitive to friction between the plates as well as the final cracking path, which can show a characteristic x.

The application of a lateral confinement significantly affects the stress-strain relationship. The peak strength as well as the ductility of the specimen increase with increasing levels of lateral confinement. Experimentally biaxial and triaxial tests are widely used to quantify the influence of lateral confinement. Conventional triaxial tests are performed by applying a compressive loading under a constant radial compressive pressure. Another possibility is to

use an odometer, which blocks the radial deformation (for instance [Burlion 01]). Among the several tests performed by different authors ([Bazant 86, Candappa 01]), in this manuscript we refer to the series conducted by Sfer [Sfer 02]. During these experiments it is observed that the more the confining pressure is increased the more inclined to the loading direction the rupture crack becomes.

Another effect that strongly influences the constitutive response, under every loading condition, is represented by the speed at which concrete is loaded. Indeed the strain rate influences various properties of concrete, but  $f_c$  and  $f_t$  are mostly affected. It has been observed that dynamically-loaded samples can carry larger loads than their static strength. This increase is explained by two mechanisms: the presence of free water in the pores, which generates the so-called Stefan effect ([Rossi 94]), and inertial effects [Janach 76]. The behavior is recorded in experiments having recourse to split Hopkinson bars (*e.g.* [Rossi 94, Ross 95, Brara 99]). The influence of dynamic loading is tackled in Chapter 4.

The concrete composition influences the mechanical properties giving different peak values in the aforementioned experimental tests. Indeed, various factors can affect its strength: for instance the ratio of cement paste to aggregate, the bond strength between mortar and aggregates, the adopted grading, the shape and the strength of the aggregates itself, water to cement ratio, type of cement used, . . . . The variation of just one parameter can indeed influence the behavior of the obtained concrete. For instance in [Wu 01] the results of a series of tensile and compressive test carried out by selecting a different coarse aggregate type revealed that the strength, stiffness, and fracture energy of concrete depend on the type of aggregate, especially for high-strength concrete. The experimental evidence of the constituents influence underlines thus the importance of selecting a fine scale level of observation for the modeling.

## 2.2 Macro and meso modeling of concrete

Concrete is a material, which is made of cement (8-15%), water (2-5%), air (5-7%) and about (70-75%) of aggregates including gravel, sand, limestone filler and finally other chemical additives in proportions smaller than 0.5%. The result of this mixture is a quasi-brittle material, whose wide range of ingredients defines the mechanical behavior. Furthermore the interactions between these constituents, highly influence the constitutive response. Although all the ingredients influence the final mechanical behavior, it seems that every ingredient has an influence according to its characteristic length. In this sense, and according to the levels of observation proposed by Wittman ([Wittmann 83]), meso-scale ( $m^{-3}$ ) and micro-scale ( $m^{-6}$ ) should be the logical working scales for material scientists in concrete research. Nevertheless, the micro-scale is still far from the computational capabilities if real size specimens needs to be analyzed. Thus, different meso-scale models have been tested by several authors for the simulation of concrete behavior and fracture (see subsection 2.2.3 and 2.2.4).

At the macro scale, the ingredients that characterize concrete's heterogeneity are not repre-

sented and one considers it as a homogeneous material. In this class fall damage models, (visco-) plastic models and fracture based models. However, this leads to models with a relatively high number of fit parameters, which are difficult to relate to physical mechanisms that occur during failure.

The second class focuses on the explicit representation of the concrete composition at a meso-level of observation. At this scale two principal phases are represented: aggregates and mortar. The main methods in this category are so-called particle models (lattice) and finite-element with cohesive capability. So it is possible to assign to every material phase a specific constitutive behavior, which enables reducing the number of fit parameters. Indeed this permits a physical identification of all material parameters of the model. Another particularity of this level of observation is that it allows the simulation of the fracturing process within the specimen. Fracture of these materials involves the opening of local micro-cracks, which may propagate, coalesce and subsequently enter into contact influencing the nonlinear failure process. The evolving damaging process is strictly related to the geometry of the meso-structure.

Furthermore meso-modeling enables to reproduce the influence of different arrangements of the meso-structure. Nonetheless, it should be noted that the computational cost increases considerably with increasing specimen size and thus, simulation at this scale are limited to small samples. As a consequence, as already stated, there is a need to transfer the obtained constitutive behavior from the meso-scale to the macro-scale through an appropriate multi-scale technique.

### 2.2.1 Damage models

Damage models have been widely used to describe the constitutive response of concrete at the macro-scale, taking into account the effects of cracking. In addition, the current available models are often coupled with (visco-) plasticity formulations (see next subsection).

In case of isotropic damage (*i.e.* equal distribution of damage in all directions) and considering an arbitrary section within the material, the presence of micro-defects contributes to the reduction of the surface that can be subjected to loads ( $F$ ). The surface  $S$  can thus be divided into two distinct areas; one called undamaged or effective area ( $S$ ) and another one, which contains all the micro-cracks, damaged surface ( $S_D$ ). This leads directly to the concept of effective stress, which is given by (for the one-dimensional case):

$$\tilde{\sigma} = \frac{F}{S - S_D} = \frac{F}{S \left(1 - \frac{S_D}{S}\right)} = \frac{F}{S(1 - D)} = \frac{\sigma}{1 - D} \quad (2.1)$$

where  $\sigma$  is the stresses associated with deformation  $\varepsilon$  and  $D$  is the local scalar variable that describes the attained damage within an element. This enables to define a relationship between the Young's modulus of the damaged material and the undamaged one ( $E$  and  $\tilde{E}$

respectively).

$$\sigma = \tilde{E}\varepsilon \quad \text{with} \quad \tilde{E} = (1 - D)E \quad (2.2)$$

The damage approach is thus based on a stiffness reduction with increasing deformation, whenever the strain exceeds a threshold value.  $D$  is computed with the help of a damage law, which depends on the amount of experienced deformation and a threshold law. Two popular threshold functions, which resort to the same free energy, are represented by the model defined by Mazars [Mazars 84] and the one of Marigo [Marigo 81]. Damage models have been introduced initially to simulate the phenomenon of micro-cracking in metallic materials ([Lemaitre 78]). Mazars ([Mazars 84]) extended the model to account for the tensile-compressive asymmetric behavior of concrete.

In fact the use of damage within a numerical scheme entails some problems. For instance the strain-softening in tension should differ from the one in compression, but this is not represented by the basic damage models. In addition, a damage law in conjunction with a finite-element framework, results in a generally small area where large deformation occurs. This leads to a spurious localization zone, with consequent mesh dependency and a dissipated energy that tends to zero with increasing level of mesh refinement.

To avoid this problem different methods have been developed. A first possibility is to fix the mesh size to an optimal value, so-called simple crack band model ([Pietruszczak 81]). A second approach foresees a density of energy that is variable depending on the selected size of the finite elements ([Willam 86]). Yet, a third approach introduces an internal length scale directly into the constitutive behavior. This is the so-called non-local theory (developed in [Pijaudier-Cabot 87]). An exhaustive study of different non-local approaches can be found in [Jirásek 98]. Damage models are not often coupled with a meso-structural representation, nevertheless an example can be found in [N'Guyen 10a].

### 2.2.2 Plasticity Models

As damage models, plasticity theories have been conceived first for metals. The main problem that arises, in their application to concrete, is that they fail to capture the brittle nature of this material in tension. On the contrary, under compression (unconstrained as well as constrained) concrete undergoes non-reversible deformation and thus its representation through plasticity modeling is straightforward.

In the elastic range concrete is assumed to be an isotropic linear elastic solid. However, with increasing applied deformation concrete undergoes both elastic and non-reversible deformations. The total strain increment ( $d\varepsilon$ ) can thus be decomposed into elastic ( $d\varepsilon^e$ ) and plastic ( $d\varepsilon^p$ ) increment, which is given for the one dimensional case by:

$$d\varepsilon = d\varepsilon^e + d\varepsilon^p \quad (2.3)$$

The limit of elasticity is defined by a failure surface (usually referred as the yield or loading surface in traditional plasticity theory). Beyond this surface the material undergoes plastic

deformations. This can be expressed as follows:

$$Y < 0 \quad \text{elastic behavior} \quad (2.4)$$

$$Y = 0 \quad \text{and} \quad \dot{Y} = 0 \quad \text{yielding} \quad (2.5)$$

$$Y = 0 \quad \text{and} \quad \dot{Y} < 0 \quad \text{elastic unloading} \quad (2.6)$$

The yield surface depends clearly on stress variables, but can also depend upon other variables, such as the plastic strain, or constant parameters, often called hardening parameters. Besides the well-know Tresca and Von Mises criterion, a widely used criterion is the model of Drucker-Prager. The problem of the choice of the failure surface can be traced back to the fact that concrete does not exhibit distinct yielding.

The hardening function defines the behavior after yielding. This allows for the failure surface to expand and change shape as the concrete is plastically loaded (plastic flow). This function is a variable part of the loading function that depends on some hardening parameters. Those hardening parameters account for different behavior of concrete such as effective plastic strain, plastic work, and volumetric strain.

Among the various works that resort to this method we can recall [Murray 79, William 84, Feenstra 96].

### Plasticity and damage

In the last decades, plasticity models have been coupled with damage models in order to reproduce more accurately the behavior of concrete in a wide range of loading ([Ottosen 79, Sercombe 98, Bažant 00, Gatuingt 02, Grassl 06, Pedersen 08, Gatuingt 08, Desmorat 10b, Pontiroli 10, Desmorat 10a]). In this approach it is also possible to introduce rate effects through introduction of visco-plasticity (*e.g.* [Dubé 96]) as well as cyclic loading response (*e.g.* [Rague-neau 98]). [Bažant 02] provides a survey over plasticity and damage models.

#### 2.2.3 Particle (lattice) models

Particle models represent a popular method to simulate concrete behavior at the meso-scale. The particularity of this approach consists in the discontinuous formulation. Indeed the material is represented through a network of beams (or lattice) relating discrete points (hence the alternative name lattice model). Therefore, the displacement field can be determined only at the center of those particles. The first application to concrete of this model can be traced back to the work of Schlangen and van Mier [Schlangen 92].

The basic idea of those models consists in representing the concrete meso-structure through a lattice system that is obtained starting from the aggregates disposition. The disposition is obtained, usually, through the grading curve of the chosen concrete or, alternatively, reconstructing the distribution of aggregates of an experimental sample depicted in a digitalized



image. So, on the basis of the heterogeneities center Delaunay triangulation (for 2D) tetrahedralization (3D) can be performed. Each edge of the generated triangle or face of tetrahedrons respectively gives the number of interactions with the neighborhood particles. The domain tessellation (*e.g.* Voronoi) defines the geometrical interaction between the aggregates, *i.e.* the section of the beams that connect the points and consequently the interaction forces that are transmitted from one to the other aggregate. During this process each heterogeneity is included in a single polyhedral cell and different material properties are assigned to the various lattice elements according to the meso-structural phases.

The constitutive response of this meso-mechanical approach is defined by the behavior of the beams. Normal forces, shear forces and moments are calculated using a conventional simple beam theory. In addition other simple rheological models account for non-reversible deformations, viscous effects and fracture. This is achieved by degradation of the beams, whose tensile strength has been exceeded, and consequent removal.

Among the numerous researchers that have had recourse to this models we may recall [Schlangen 92, Bolander Jr. 98, Cusatis 06, Kozicki 07, Grassl 10].

Particle models can thus provide good estimates of concrete behavior for several loading conditions, however, they introduce a non physical length scale in the material description (lattice beam spacing), since they are based on fictitious particles. In addition, they face difficulties in reproducing exactly simple elastic deformations (see for instance [Jerier 12]). Moreover, in case of compressive shearing, the broken stiffness connections should be recovered in order to model aggregates interlock. Thus, we have chosen to select a meso-mechanical model that does not show the aforementioned problems and that resorts to simple constitutive assumptions, avoiding phenomenological modeling.

### 2.2.4 Finite Element with fracture capability

Meso-modeling of concrete within a finite-element framework with an explicit representation of cracks can be traced back to the work of [Roelfstra 85]. Similarly to the lattice approach, this class of models aims to represent accurately the concrete components at a meso-scale level of observation. However, to achieve a precise representation of the aggregates a fine-mesh is needed. For this reason, most researchers have focused on two-dimensional models that allow reducing the high computational cost and thus achieving better modeling ([Carol 01, Tijssens 01, Willam 04, Wriggers 06]) while only few have moved to 3D (*e.g.* [Caballero 06]).

This approach describes concrete as composed by mortar and aggregates with an interfacial transition zone between them. Cracking is represented having recourse to cohesive zone theories. The cohesive crack model has been first applied to concrete by [Hillerborg 76] under the name of fictitious crack model. This method resorts to classical cohesive approach, but considers that micro-cracks can initiate anywhere in the specimen and not only along a pre-determined path. The propagation of cracks is, indeed, controlled by the interfacial strength of the cohesive elements. The bulk elements around the interfacial transition zone behave elastically or following a more phenomenological constitutive relationship (*e.g.* [Grassl 08]). The inclusions can be represented following, more or less, a realistic distribution. Specimens

with inclusions showing a fixed size, irregular sizes, and spherical shape of the heterogeneities or polygonal form have been adopted in the different models. The size of the smallest inclusions is related to the mesh size too. In general 2D models allow greater mesh refinement and thus to better follow a grading curve. Examples of early applications for mixed-mode fracturing in homogeneous concrete samples include the works of [Planas 91] and [Carol 92].

In this thesis we have elected this class of models with an explicit representation of cracks. We have chosen to allow cohesive insertion anywhere in the mesh, while bulk elements are assumed to behave linear elastically. Therefore all source of non-linearity is assumed to be concentrated in the cohesive elements. This strategy has been chosen in order to avoid recourse to more phenomenological laws, which entail a larger number of parameters that might be difficult to identify physically.

### 2.3 Meso-structure

As already stated, the meso-modeling of concrete enables one to describe the heterogeneous internal material structure of concrete. During failure of concrete micro-cracks initiate and propagate characterizing the nonlinear stress-strain response of concrete. The fracture behavior is clearly influenced by the diameters of the biggest inclusions, which can show sizes up to the order of some centimeters. For instance one might think about the composition's influence on the final shape of the crack path. Indeed, if normal-strength concrete is considered, damage tends to initiate at the interfaces between cement paste and aggregates. The interface between these two components is usually called Interfacial Transition Zone (ITZ). Afterwards cracks tend to propagate along the ITZs and to bridge the gap between these failure zones developing within the matrix. Therefore, at this scale concrete can be represented as a biphasic material made of inclusions embedded in a cement paste matrix. In our approach the interface transition zone is represented (when cracking starts) by means of dynamically inserted cohesive elements. Cracks are represented explicitly in the matrix phase and inclusions too, while other authors have recourse to cohesive elements only at the inter-element boundary between matrix and particles.

Usually only big and medium aggregates are modeled, while all particles with a diameter smaller than 2 mm (*i.e.* sand) are assumed to be mixed up with mortar and small pores establishing the matrix phase. Therefore this phase is considered as a homogeneous component at the meso-scale. The material properties of the mortar phase are thus strongly depended on the type of cement used, amount of pores, water to cement ratio and other additives present in the concrete. The bond strength of the ITZs is also influenced by these parameters, as well as by the shape of the inclusions. Experimentally and numerically it has been observed that spherical particles have a negative influence on the tensile and compressive strength of concrete. In the experimental literature, it is possible to find different values for an estimation of the strength and fracture energy of this transition zone (*e.g.* [Aquino 95, Caliskan 02]).

### 2.3.1 Mesh-generator

The aggregate fraction in concrete, if only particles with a diameter above 2 mm are considered, is around 30% and can rise up above 70 %, if smaller inclusions are considered too. Aggregates can be made of different types of stones, which gives a large scatter in the measured experimental properties. Moreover they can show various kind of geometry, according to their manufacturing process, from rounded ones to more irregular shapes if the particles have been obtained through crushing. In numerical simulations, both kinds of inclusions have been employed by different authors. Besides the shape, the size distribution and spatial arrangement of the aggregates within the specimen highly influences the behavior of concrete. Usually the grading of the particles is chosen according to a Fuller and Thompson density curve ([Fuller 06]). In order to reproduce a meso-structure for the numerical model it is possible to have either recourse to a (random) generator of aggregates or to recover an experimental arrangement through an image processing technique. The first approach has been undertaken in this investigation. In this work the geometry has been obtained with different generator: one based on a Voronoi mesher (see Chapter 4), another that creates regular circles following experimental reported values for the grading (Chapter 4) and a third one that produces irregular polygons following a Fuller curve (Chapter 6).

Figure 2.2 depicts three examples of specimen obtained with the different meso-structure

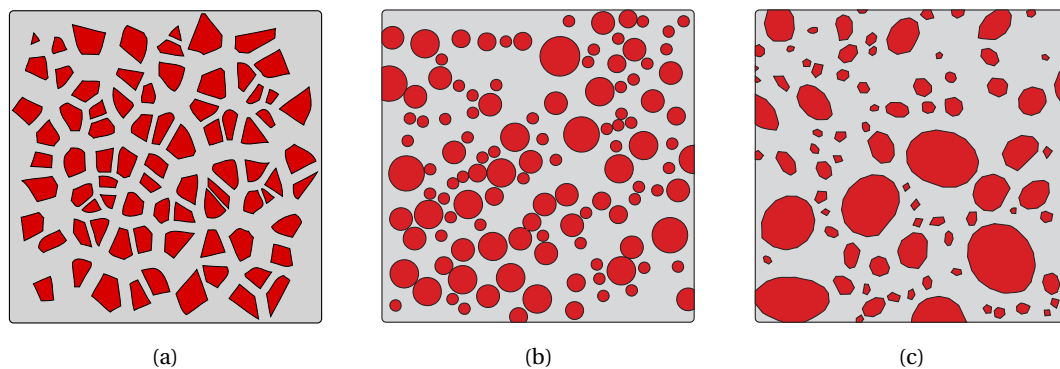


Figure 2.2: Examples of different meso-structure geometries: (a) obtained with a Voronoi mesher, while (b) and (c) are generated according to a grading curve with circular and polygonal inclusions respectively.

generators. It is possible to notice that for the second and third samples there are inclusions, which intersect the specimen edges. In order to avoid an artificial increase of the volume matrix due to this boundary effect, the heterogeneities are placed in a larger sample with a final cut of all parts outside of the concrete specimen. Once the geometry has been created it is possible to generate the mesh with a finite-element mesher.



## 3 Numerical framework

### 3.1 Fundamental concepts of the Finite-Element Method

As stated in the Introduction Chapter, the representation of complex material behavior that undergoes several physical processes during brittle failure, needs a careful numerical treatment. A very popular and powerful tool to tackle such problems is offered by means of numerical simulations. Those have originated with the start of the computational mechanics branch during the 50's, when pioneer engineers worked closely with the aircraft and aerospace industry. The birth of the Finite-Element Method (FEM) can be traced back to these years. It is generally attributed to the seminal work of [Turner 54].

From this time up to the present, much effort has been devoted to the development of computational techniques. Nowadays, thanks to this progress and the raising computational power of the machines, many complex engineering problems, involving elaborate multi-physical behavior (that would be impossible to be solved analytically), can be addressed. In the following we will first describe the adopted general FE-framework, and then present a review of the cohesive approach for fracture mechanics.

#### 3.1.1 Strong form: governing equations

The dynamic motion of a continuum body, as the one depicted in Figure 3.1, is considered. The figure illustrates two different configurations: the initial one also called reference configuration (time  $t_0$ ), and the current or deformed configuration (time  $t$ ). In the Lagrangian description the reference configuration plays an important role in the analysis, since all equations are referred to it. Associated with these two states are the material (Lagrangian) coordinate denoted by  $\mathbf{X}$  and the spatial (Eulerian) coordinate, indicated with  $\mathbf{x}$ . All variables referred to the initial configuration will be identified by a subscript zero. At every time  $t$  ( $t \in [t_0, t_{end}]$ ) the current configuration and subsequent motion of the body are described by the following function:

$$\mathbf{x} = \boldsymbol{\varphi}(\mathbf{X}, t) \quad \forall \mathbf{X} \in B_0 \quad (3.1)$$

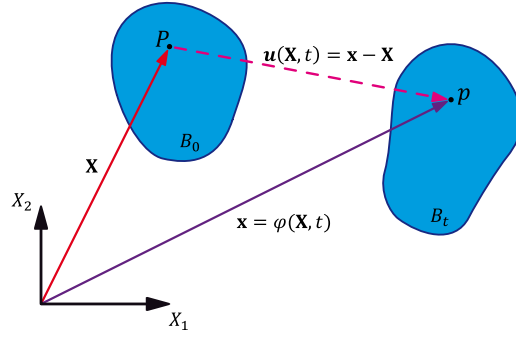


Figure 3.1: Lagrangian deformation of the body  $B_0$ .

where  $\boldsymbol{\varphi}$  is called deformation mapping between the initial and current positions. The displacement  $\boldsymbol{u}(\boldsymbol{X}, t)$  is given by the difference between the deformed and reference configuration

$$\boldsymbol{u}(\boldsymbol{X}, t) = \boldsymbol{\varphi}(\boldsymbol{X}, t) - \boldsymbol{X} = \boldsymbol{x} - \boldsymbol{X} \quad \forall \boldsymbol{X} \in B_0 \quad (3.2)$$

The deformation of infinitesimal material neighborhoods is described by the deformation gradient

$$\mathbf{F} = \nabla_0 \boldsymbol{\varphi}(\boldsymbol{X}, t) \quad \forall \boldsymbol{X} \in B_0 \quad (3.3)$$

where  $\nabla_0$  is the material gradient operator. Let  $J$  be the Jacobian, which represents the ratio of an infinitesimal volume in the deformed configuration to the corresponding volume in the undeformed body

$$J = \det(\mathbf{F}) > 0 \quad \forall \boldsymbol{X} \in B_0 \quad (3.4)$$

To transform quantities that are defined with respect to the area in deformed configuration to those relative to the area in the reference configuration, and vice versa, we use the Nanson's relation

$$dA \boldsymbol{n} = J dA_0 \mathbf{F}^{-T} \boldsymbol{N} \quad (3.5)$$

where  $dA$  is an area of a region in the deformed configuration,  $dA_0$  is the same area in the reference configuration, and  $\boldsymbol{n}$  is the outward normal to the area element in the current configuration while  $\boldsymbol{N}$  is the outward normal in the reference configuration.

The stress measure, which is used in the Lagrangian formulation, relates the forces in the current configuration with the cross section in the reference configuration and is called first Piola-Kirchoff stress tensor. This can be related to the Cauchy stress tensor ( $\boldsymbol{\sigma}$ ) as follows:

$$\mathbf{P} = J \boldsymbol{\sigma} \mathbf{F}^{-T} \quad (3.6)$$

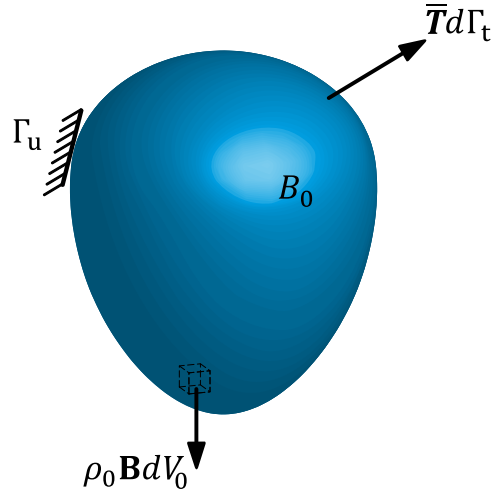


Figure 3.2: Body  $B_0$ .

Let us consider the body of Figure 3.2 with body forces acting per unit reference denoted with  $\rho_0 \mathbf{B}$ . Its surface is characterized by a traction boundary  $\Gamma_t$ , Neumann part, and a displacement boundary  $\Gamma_u$ , Dirichlet part. The continuum problem is governed by the balance of linear momentum and the boundary conditions

$$\nabla_0 \cdot \mathbf{P} + \rho_0 \mathbf{B} = \rho_0 \ddot{\boldsymbol{\varphi}} \quad \forall \mathbf{X} \in B_0 \quad (3.7)$$

$$\mathbf{P} \cdot \mathbf{N} = \bar{\mathbf{T}}(\mathbf{X}, t) \quad \forall \mathbf{X} \in \Gamma_t \quad (3.8)$$

$$\boldsymbol{\varphi} = \bar{\boldsymbol{\varphi}} \quad \forall \mathbf{X} \in \Gamma_u \quad (3.9)$$

To complete the problem, initial conditions must be provided:

$$\boldsymbol{\varphi}(\mathbf{X}, t_0) = \mathbf{x}_0 \quad \forall \mathbf{X} \in B_0 \quad (3.10)$$

$$\dot{\boldsymbol{\varphi}}(\mathbf{X}, t_0) = \mathbf{v}_0 \quad \forall \mathbf{X} \in B_0 \quad (3.11)$$

It remains to define the constitutive behavior of the material that can be obtained by deriving the strain energy density function  $\hat{W}$  with respect to the deformation gradient  $\mathbf{F}$

$$\mathbf{P} = \frac{\partial \hat{W}}{\partial \mathbf{F}} \quad (3.12)$$

### 3.1.2 Weak form and discrete formulation

The momentum equation presented above (also called strong form, Equation 3.7) cannot be applied directly to the FEM formulation and needs, therefore, to be reformulated in a weak form. The weak form is obtained by multiplying the moment equation with a test function and integrating over the domain. The test function has to satisfy continuity conditions and the displacement boundary conditions and it represents, therefore, a virtual displacements  $\partial \mathbf{u}$ . Hence, each terms in the weak form represents a virtual work due to the virtual displacement  $\partial \mathbf{u}$  ( $=\partial \boldsymbol{\varphi}$ ). The weak form can be written as (plane )

$$\int_{B_0} (\mathbf{P} : \nabla_0 \partial \mathbf{u} + \rho_0 \ddot{\boldsymbol{\varphi}} \cdot \partial \mathbf{u}) dV_0 - \int_{B_0} \rho_0 \mathbf{B} \cdot \partial \mathbf{u} dV_0 - \int_{\Gamma_t} \bar{\mathbf{T}} \cdot \partial \mathbf{u} d\Gamma_t = 0 \quad (3.13)$$

The equilibrium above represents the principle of virtual work (also called principle of virtual displacements), which is the basis of the FEM. The principle requires that for any small virtual displacements (imposed on the body in its state of equilibrium) the sum between internal and external work has to vanish. The discrete equations are obtained from the principle of virtual work by using finite-element interpolants for the virtual displacements. The domain is discretised in elements. In our case, we work in two dimensions with six node triangular elements. Thus, we can describe the virtual displacements using the element interpolation

$$\partial \mathbf{u}_e = \sum_{a=1}^6 N_a(\mathbf{X}) \partial \mathbf{u}_a \quad (3.14)$$

where  $\partial \mathbf{u}_a$  are the nodal values of the virtual displacements and  $\partial \mathbf{u}_e$  those within each element, of which  $N_a$  represent the shape functions.

When the discretization (Equation 3.14) is inserted into Equation 3.13 and the integrations are carried out, the discretized equation of motion becomes

$$\mathbf{M} \ddot{\mathbf{a}} + \mathbf{f}^{int} = \mathbf{f}^{ext} \quad (3.15)$$

where  $\mathbf{M}$  is the mass matrix,  $\mathbf{a}$  ( $=\ddot{\boldsymbol{\varphi}}$ ) is the nodal acceleration vector,  $\mathbf{f}^{int}$  and  $\mathbf{f}^{ext}$  represent the internal and external forces vectors.

### 3.1.3 Time integration

In order to find the solution of the equilibrium equation (3.15), we need to use a convenient finite-difference expression to approximate the accelerations and velocities in terms of displacements. One popular procedure of time integrators is the Newmark  $\beta$ -method [New-



mark 59]:

$$\mathbf{u}_{n+1} = \mathbf{u}_n + \Delta t \mathbf{v}_n + \Delta t^2 \left[ \left( \frac{1}{2} - \beta \right) \mathbf{a}_n + \beta \mathbf{a}_{n+1} \right] \quad (3.16)$$

$$\mathbf{v}_{n+1} = \mathbf{v}_n + \frac{1}{2} \Delta t [(1 - \gamma) \mathbf{a}_n + \gamma \mathbf{a}_{n+1}] \quad (3.17)$$

$$\mathbf{M} \mathbf{a}_{n+1} = \mathbf{f}^{ext}(t_{n+1}) - \mathbf{f}^{int}(t_{n+1}) \quad (3.18)$$

where  $\mathbf{u}$ ,  $\mathbf{v}$  and  $\mathbf{a}$  denote the material displacement, velocity and acceleration fields.  $\beta$  and  $\gamma$  are Newmark's parameters, which control the algorithm's stability and accuracy. By setting  $\gamma$  equal 0.5 the algorithm has no damping, and if  $\beta$  is equal to zero, we obtain the second order explicit scheme (adopted in this work)

$$\mathbf{u}_{n+1} = \mathbf{u}_n + \Delta t \mathbf{v}_n + \frac{1}{2} \Delta t^2 \mathbf{a}_n \quad (3.19)$$

$$\mathbf{a}_{n+1} = \mathbf{M}^{-1} (\mathbf{f}^{ext}(t_{n+1}) - \mathbf{f}^{int}(t_{n+1})) \quad (3.20)$$

$$\mathbf{v}_{n+1} = \mathbf{v}_n + \frac{1}{2} \Delta t (\mathbf{a}_n + \mathbf{a}_{n+1}) \quad (3.21)$$

Whereas, if  $\beta$  is set different to zero, the time integration is indicated as implicit. This solution method has the advantage to be unconditionally stable for linear problems and to allow large time step. On the other hand, an explicit scheme requires a smaller time step but having recourse to a lumped mass matrix, the equations are not coupled and can be solved directly (no matrix inversion). This algorithm is stable under the condition that the time step is below a critical time step, which is

$$\Delta t_{stable} = \alpha \left( \frac{l_e}{\sqrt{\frac{\lambda_e + 2\mu_e}{\rho_e}}} \right)_{min} \quad (3.22)$$

where  $l_e$  is the length of the element,  $\lambda_e$  and  $\mu_e$  are the Lamé coefficients of the element and  $\rho_e$  its density ( $\sqrt{\lambda_e + 2\mu_e} / \sqrt{\rho_e}$  is the longitudinal wave speed). The stable time step is chosen equal to the smaller value over all elements in the mesh multiplied with a security coefficient  $\alpha$  (typically around 0.1).

## 3.2 The cohesive zone approach

### 3.2.1 Origins of the cohesive approach

As introduced in Chapter 2, in order to model dynamic fracture and damage in brittle materials, two main classes of computational methods have been developed during the last decades. One method is based on continuum damage models and the other one on cohesive zone theories. In the first method the fracture process is included in the material constitutive behavior. The accumulated damage in an element is responsible for the degradation of the material elasticity. This means that fracture is modeled in a continuum sense and the discrete nature of cracks is lost (however this homogenization allows modeling of large scale problems).

The second approach is the cohesive one, and was introduced by Dugdale [Dugdale 60] and Barenblatt [Barenblatt 62] in the 1960' s. The model basically describes fracture as a separation process, which occurs at the crack tip (Figure 3.3). The debonding process is assumed to

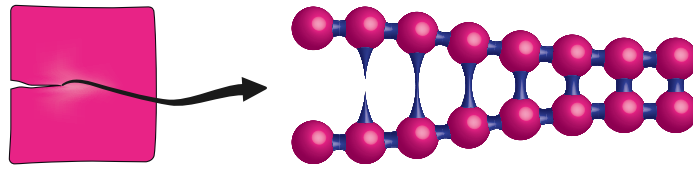


Figure 3.3: Debonding process between the atoms at the crack tip.

be confined in a small region of material called the cohesive zone, which accounts for the breaking of the atomic bonds during crack propagation. In this region, crack face separation occurs producing a displacement jump  $\Delta$  (Equation 3.24). The constitutive relationship, which relates the traction acting on the separating surfaces to the relative opening displacement vector ( $\Delta$ ), is called the Traction Separation Law (TSL):

$$\mathbf{T} = \mathbf{T}(\Delta) \quad (3.23)$$

with

$$\Delta = \varphi^+ - \varphi^- = \llbracket \varphi \rrbracket \quad (3.24)$$

where  $\varphi^+$  and  $\varphi^-$  represent the deformation mappings of the two cohesive surfaces of the body (depicted in Figure 3.3). Therefore damage is accumulated in the cohesive zone via degradation of the cohesive tractions, while the bulk material outside the cohesive zone remains undamaged and continues to behave linear elastically without a crack tip singularity. In a computational framework, the cohesive zone is represented by interface elements (in which the TSL is implemented). These elements, called cohesive elements, are placed at the boundaries between bulk elements, constraining the cracks to propagate following the

interelement boundaries, which are determined by the discretisation (mesh dependency). In order to avoid this problem, it is necessary to have recourse either to fine meshes or adaptive meshing techniques. Other solutions are offered by different methods like the extended Finite-Element Method (X-FEM), where the crack can propagate within the elements. Usually the TSL is related to a potential ( $\phi$ ), which represents the stored fracture energy for a specific interface. Because of this formulation it is possible to obtain the components of the traction vector ( $\mathbf{T}$ ) simply by differentiating the potential with respect to the opening displacement vector:

$$\mathbf{T} = \frac{\partial \phi}{\partial \Delta} \quad (3.25)$$

Rice [Rice 68] demonstrated the non-dependency of the TSL from the bulk material using the  $\mathcal{J}$ -integral, which is independent from the bulk material that surrounds the crack. The situation is schematically illustrated in Figure 3.4 for a two-dimensional crack problem with the crack tip aligned with the  $x_1$ -axis. The  $\mathcal{J}$ -integral is defined as

$$\mathcal{J} = \int_{\Gamma} W dx_2 - \int_{\Gamma} T_i \frac{\partial u_i}{\partial x_1} dS \quad (3.26)$$

where  $S$  denotes the curve length along  $\Gamma$  (which is a contour going around the crack in counter-clockwise direction around the tip),  $T_i$  are the components of the traction vector and  $W$  is the strain energy density. As shown in Figure 3.4 the integration path  $\Gamma$  can be chosen

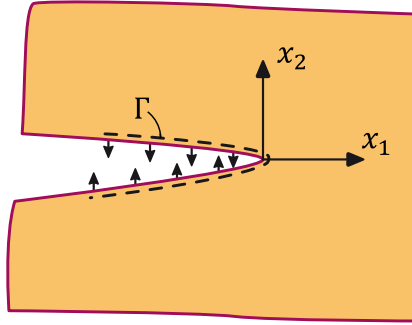


Figure 3.4: Cohesive approach and integration path for the  $\mathcal{J}$  integral.

just outside the failure process zone. The integral reduces in this case as follows

$$\mathcal{J} = - \int_{\Gamma} T_i \frac{\partial u_i}{\partial x_1} dS = \int_0^{\Delta^*} \mathbf{T}(\Delta) \cdot d\Delta \quad (3.27)$$

where  $\Delta^*$  is the separation distance beyond which complete debonding has occurred. Using the assumption of Equation 3.25, coupling it with the last equation and performing the

integration enables one to relate value  $\phi(\Delta^*)$  with the  $\mathcal{J}$ -Integral. This is called the work of separation.

$$\mathcal{J} = G_c = \int_0^{\Delta^*} T(\Delta) \cdot d\Delta = \phi(\Delta^*) = \phi_{sep} \quad (3.28)$$

If  $\mathcal{J}$  is evaluated far away from the process zone (*e.g.*  $\Gamma$  matches the external boundaries of the fractured specimen) it can be calculated from the applied far-field loading. As the  $\mathcal{J}$ -integral is path independent the two computed values must be identical. Thus, the dissipated fracture energy during decohesion corresponds to the available (through far field loading) elastic energy (and is equal to the potential energy decrease rate of the uncracked system). Moreover, since the area under the TSL is equal to two times the surface energy, the cohesive zone theory gives the same prediction in terms of fracture behavior as the energy-based approach postulated by Griffith [Griffith 20].

### 3.2.2 Intrinsic and extrinsic cohesive approach

In the computational framework, the cohesive zone is represented by interface elements (in which the TSL is implemented). These elements, called cohesive elements, are placed at the boundaries between bulk elements.

It is possible to distinguish between two main categories of TSL, depending on the response of the interface before the softening behavior. With the extrinsic approach (see Figure 3.5b), which is used in this work, the surface shows only a softening behavior (the response of the surface prior crack initiation is assumed to be rigid). Whereas, with the intrinsic approach (see Figure 3.5a), the TSL exhibits generally an initial linear elastic behavior prior to softening, which requires cohesive elements to be present from the beginning of the simulation.

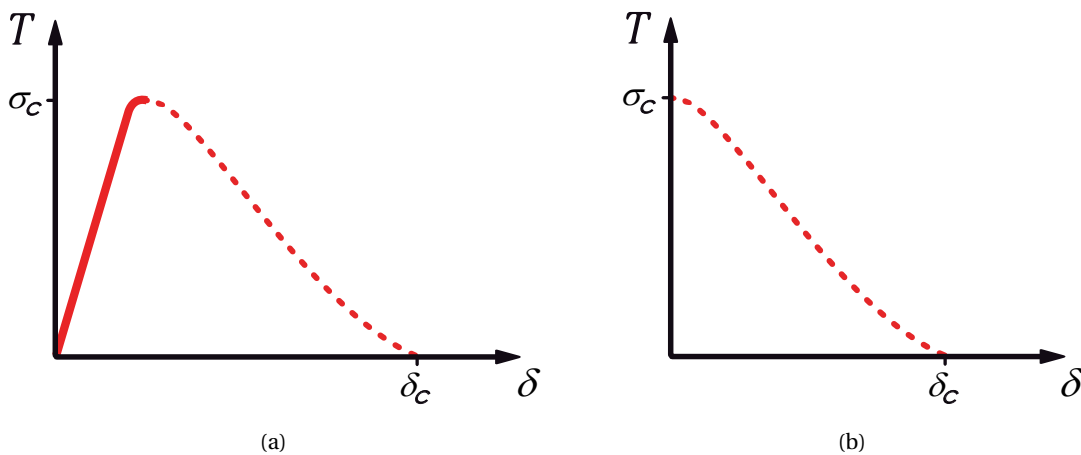


Figure 3.5: (a) Intrinsic and (b) extrinsic approach.

Therefore, this implies that the crack path is determined a priori. A common application is the modeling of the delamination process in material composites, where the separation occurs at the well-known material interfaces (*e.g.* [Chaboche 97, Geubelle 98]).

#### 3.2.3 Xu and Needleman exponential cohesive law

Among the several intrinsic TSLs (with different shapes) that have been proposed, we present here one of the most popular version: the Needleman [Xu 93] exponential cohesive law. In a one-dimensional setting is expressed as:

$$\phi(\Delta) = \sigma_c \delta_n \exp \left[ 1 - \left( 1 + \frac{\Delta}{\delta_n} \right) e^{-\frac{\Delta}{\delta_n}} \right] \quad (3.29)$$

where  $\delta_n$  is the value of the opening displacement, beyond which softening begins.  $\sigma_c$  is the maximum normal cohesive stress ( $\sigma_c = f_t$  is often chosen for concrete), which can be attained for an opening equal to  $\delta_n$  (Figure. 3.6). As a free energy function is assumed, the cohesive traction can be obtained, according to Equation 3.25, simply by differentiation.

$$T = \sigma_c \frac{\Delta}{\delta_n} e^{1 - \frac{\Delta}{\delta_n}} \quad (3.30)$$

The potential form for two-dimensional cases with coupling between normal and tangential opening was presented by Xu and Needleman [Xu 93].

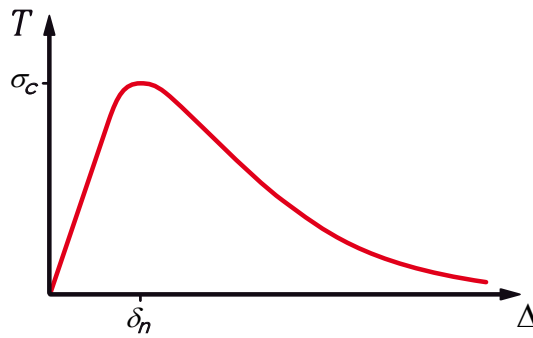


Figure 3.6: Needleman exponential cohesive law [Xu 93].

The presence of the cohesive elements, with an initial elasticity in the uncracked body at the beginning of the simulation, causes an artificial elasticity at the element interfaces. This leads to a partial reflection of incident stress waves at the inter-element boundaries and to an unrealistic reduction of the stiffness. This phenomenon is denoted as artificial compliance. In order to reduce this effect, the initial slope of the elastic response can be increased. However, the bigger problem is that if the initial slope increases, the critical time step must be reduced to avoid numerical instabilities. This issue is resolved with the extrinsic approach.

### 3.2.4 Camacho-Ortiz linear irreversible cohesive law

As previously mentioned the characteristic of the extrinsic approach is the initial rigid response before reaching a critical stress value. To achieve this within a computational framework, a cohesive element is inserted between an inter-element boundary only after the stress at the boundary of the two elements has reached a critical value (this process is called dynamic insertion). The inserted elements have initially a thickness equal to zero. In two dimensions the mid-node at the inter-element edge is duplicated, whereas the end-node of the segment are duplicated only if they are shared by an adjacent cohesive elements. In this case the end-node is duplicated allowing the crack tip propagation. One of the most popular TSL for

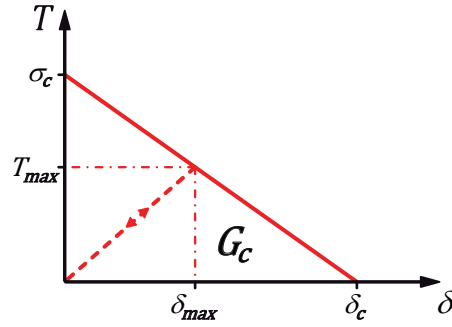


Figure 3.7: Camacho-Ortiz linear decreasing cohesive law [Camacho 96].

the extrinsic approach was proposed by Camacho and Ortiz [Camacho 96] in 2D (and Pandolfi and Ortiz [Pandolfi 99] in 3D). There, the cohesive law is a linear decreasing function (depicted in Figure 3.7) of the effective opening displacements and is derived from a free potential energy.

$$\phi(\delta) = \frac{1}{2} \sigma_c \delta \left( 2 - \frac{\delta}{\delta_c} \right) \quad (3.31)$$

Where  $\sigma_c$  represents the local material strength and  $\delta_c$  represents the effective relative displacement beyond which complete de-cohesion occurs. The potential is assumed to depend not directly on the relative displacement vector,  $\Delta$ , but on an effective scalar displacement, which has the following form:

$$\delta = \sqrt{\beta^2 \Delta_t^2 + \Delta_n^2} \quad (3.32)$$

where  $\Delta_n$  and  $\Delta_t$  represent the normal and the tangential separation over the surface with unit outward normal  $\mathbf{n}$  and unit tangential vector  $\mathbf{t}$  respectively. The parameter  $\beta$  accounts for the coupling between normal and tangential displacements. The derivation of the free potential energy with respect to the opening displacement leads to the cohesive tractions (2D):

$$\mathbf{T} = \frac{\partial \phi}{\partial \Delta} = \frac{T}{\delta} (\beta^2 \Delta_t \mathbf{t} + \Delta_n \mathbf{n}) \quad (3.33)$$

### 3.2. The cohesive zone approach

This traction in case of crack opening is given by:

$$T(\delta, \delta_{max}) = \sigma_c \left(1 - \frac{\delta}{\delta_c}\right) \quad \text{for } \delta = \delta_{max} \quad (3.34)$$

Where  $\delta_{max}$  stores the maximal effective opening displacement attained. Whereas for crack closure or reopening ( $\delta$  smaller than  $\delta_{max}$ ) the functional form is assumed to have the form ([Pandolfi 99]):

$$T(\delta, \delta_{max}) = \frac{T_{max}\delta}{\delta_{max}} \quad \text{for } \delta < \delta_{max} \quad (3.35)$$

Where  $T_{max}$  is the value of the effective traction when  $\delta$  is equal to  $\delta_{max}$ . Moreover,  $\delta_{max}$  also accounts for the irreversibility of the law allowing successive loading/unloading steps.

Note that the definition of  $\sigma_c$  and  $\delta_c$  implicitly establish the existence of an effective fracture energy  $G_c$ , which corresponds to the area under the curve of Figure 3.7.

$$G_c = \frac{1}{2}\sigma_c\delta_c \quad (3.36)$$

It is well known that the relationship between the cohesive law and the critical energy release rate  $G_c$  introduces a length scale into the material description. The size of the mesh elements has to be chosen taking into account this length. This means that the cohesive zones are sensitive to the size of the specimen. The derivation of this length scale can be found in the work of Palmer [Palmer 73] and is called cohesive zone length  $l_z$ . As shown in Figure 3.8 the

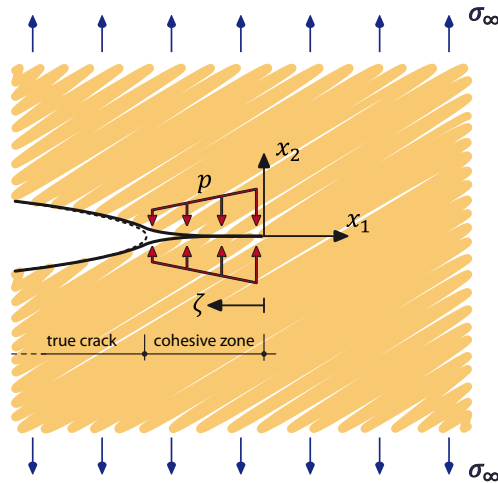


Figure 3.8: Representation of a crack with a cohesive zone fictitious crack tip subjected to far field loading  $\sigma_\infty$ .

introduction of a cohesive zone eliminates the stress singularity predicted by LEFM at the crack tip by introducing a stress distribution (traction) across a virtual crack tip. An estimate of

the cohesive length can be obtained by superposing the stress acting on a traction-free crack subjected to far-field loading  $\sigma_\infty$ , with the stress distribution generated by the distributed load ( $p$ ), acting on the cohesive zone.

$$K_I = K_{I,\sigma_\infty} + K_{I,p} = 0 \quad (3.37)$$

where  $K_I$  is the mode-I stress intensity factor (subscripts  $\sigma_\infty$  and  $p$  stand for far-field loading and distributed load respectively). Assuming a linear decreasing law that act on the cohesive zone and relating  $K_I$  with the energy release rate of the material  $G_c$

$$K_I^2 = G_c E^* \quad (3.38)$$

where  $E^*$  is the Young-modulus ( $E^* = E$  for plane stress,  $E^* = E/(1 - \nu^2)$  for plane strain). The resulting cohesive zone length can be written as

$$l_z = \frac{9\pi E G_c}{32(1 - \nu^2)\sigma_c^2} \quad (3.39)$$

This length has an important influence on the mesh size around the crack tip in numerical simulations. In general the following relation, proposed by Falk *et al.* [Falk 01], has to be satisfied

$$l_e \ll l_z \ll W \quad (3.40)$$

where  $l_e$  is the maximal element size in the fracture area and  $W$  is the size of the specimen. This relation implies that the mesh size has to be chosen according to this length scale in order to fully resolve the decohesion process and that the cohesive length should be small, compared to the specimen size.

Another characteristic measure, which was first derived by Camacho and Ortiz in [Camacho 96], is the characteristic opening time

$$\Delta t_c = \frac{\rho c \delta_c}{2\sigma_c} \quad (3.41)$$

where  $c$  is the longitudinal wave speed and  $\rho$  the mass density. According to this characteristic time, the material response is different when subjected to fast or slow strain rates. This phenomenon reproduces in fact the real dynamic behavior of brittle solids.

### 3.2.5 Formulation involving an interface

Let us consider again the body of Figure 3.2, but crossed by an interface (as depicted in Figure 3.9). The body is thus partitioned into two sub bodies  $B_0^\pm$ , which are situated on the top or bottom surface of the cohesive surface  $S_0$ . These surfaces are denoted with  $S_0^\pm$ . Therefore, we can add to the balance of linear momentum (Equation 3.7) the following condition over



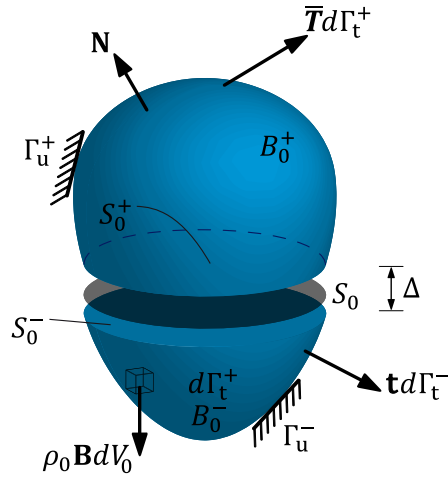


Figure 3.9: Body  $B_0$  with a cohesive surface  $S_0$ .

the discontinuity to ensure equilibrium

$$\llbracket \mathbf{P} \cdot \mathbf{N} \rrbracket = \llbracket \mathbf{T} \rrbracket \quad \forall \mathbf{X} \in S_0^\pm \quad (3.42)$$

The introduction of an interface also results in an additional term in the weak formulation of Equation 3.13. The weak form can thus be rewritten as

$$\int_{B_0} (\mathbf{P} : \nabla_0 \partial \mathbf{u} + \rho_0 \dot{\boldsymbol{\varphi}} \cdot \partial \mathbf{u}) dV_0 + \int_{S_0} \mathbf{T} \cdot \llbracket \partial \mathbf{u} \rrbracket dS_0 - \int_{B_0} \rho_0 \mathbf{B} \cdot \partial \mathbf{u} dV_0 - \int_{\Gamma_t} \bar{\mathbf{T}} \cdot \partial \mathbf{u} d\Gamma_t = 0 \quad (3.43)$$

This formulation will be applied to a tensile test of a two-dimensional concrete specimen in the next chapter.



## 4 Influence of the meso-structure in dynamic tensile loading

In this chapter we investigate the dynamic behavior of concrete in relation to its composition within the adopted computational framework. In order to understand the loading-rate sensitivity of concrete, we simulate direct tensile-tests for strain rates ranging  $1\text{--}1000\text{ s}^{-1}$ . We investigate the influence of aggregate properties (internal ordering, size distribution and toughness) on peak strength and dissipated fracture energy. We show that a rate independent constitutive law captures the general increase of peak strength with strain rate. However, a phenomenological rate-dependent cohesive law is needed to obtain a better agreement with experiments. Furthermore, at low rates, peak strength is sensitive to the inclusions' toughness, while the matrix dominates the mechanical behavior at high rates. The results presented here have been published in [Snozzi 12b]. While the last section of the chapter before the conclusions summarizes a later investigation, which is reported in [Gatuingt 12].

### 4.1 Introduction

Structures made of concrete, a highly heterogeneous material, are often subjected to dynamic loads. These may include impact, explosions and seismic loads. Although it is well known that the mechanical behavior of concrete depends on strain rate, the rate dependency of this material under dynamic loading conditions is usually not taken into account in the design codes.

Among others, peak strength, strain at peak strength and total dissipated fracture energy have been shown to be dependent on strain rate, ([Malvar 98, Ross 95]). In general, concrete exhibits a higher peak strength when it is loaded at higher strain rates and this increase has been shown to grow linearly with the strain rate. Fortunately, the augmentation of strength is accompanied by a larger dissipation of fracture energy, so concrete does not become more brittle.

Nevertheless, the dynamic behavior of concrete under high-strain-rate tensile loading has still not completely been understood. For instance it is not yet clear what the physical origins of this stress increase are. In addition, the influence of the internal micro structure of concrete,

and the mechanisms which lead to different crack patterns when varying the loading rate, remain open questions. Unfortunately performing a proper dynamic experimental test in direct tension brings some difficulties. One of the biggest limitations is how to attach properly the specimen to the testing machine. Therefore, some authors have used, for high strain rates, an indirect method employing the Hopkinson bar ([Rossi 94, Brara 07]). In this case, a compressive wave, sent to the specimen, travels through the sample until it finds the free boundary and reflects back already as a tensile wave. Then, the specimen breaks by spalling. However, it is still not clear whether or not the incident compressive wave could have affected the material before the tensile wave initiates its way back.

This chapter aims at exploiting the capabilities of the meso-mechanical model of concrete. The objectives of our work are twofold. First, we wish to make explicit the influence of the toughness of aggregates on the macroscopic response. To this end, we consider two different types of aggregates differing in their properties (called hard and soft aggregates). The spatial ordering of the meso-structure and the aggregates size are investigated as well. Second, we study the rate dependence of concrete in relation with its meso-structure composition. We propose to adopt a rate dependent cohesive law to reproduce with better accuracy the experimental observations of strain-rate strengthening. While rate dependency has been taken into account in several concrete models, using either a rate-dependent damage formulation ([Dubé 96, Ju 89]), visco-plasticity ([Sluys 92]) or a coupling between both formulations ([Gatuingt 02]), little attempts have been made to couple rate dependency with a meso-scale modeling of concrete. A noteworthy exception includes some recent work, for instance [Cusatis 06] within the lattice framework and [Pedersen 07] within a (viscoelastic viscoplastic) damage formulation with interfacial transition zone. Our work will extend this line of thought to the finite-element/cohesive-element approach.

This chapter gathers a mesh convergence analysis and parametric studies showing the influence of aggregates properties, spatial ordering, sizes, and strain rates. A discussion on the advantage of a rate-dependent cohesive law formulation is brought towards the end of the chapter.

### 4.2 Meso-structure characteristics

As already explained in Chapter 2 our model considers concrete as a material made only of two components. In this study the large aggregates have been initially represented by means of Voronoï polyhedrons. To generate them, a program starting from a Voronoï mesher has been developed.

To prevent the final Voronoï geometry of presenting tiny edges ([Caballero 06]) a Body Centered Cube (BCC) was chosen for the initial distribution of points. The generation points code is linked to the Voronoï generator program and the resulting geometry (in terms of Delaunay mesh) is linked to another code which detects each polyhedron, shrinks, moves and rotates it following an uniform random distribution. As a result, a set of Voronoï polyhedrons

surrounded by a box is obtained, Figure 4.1.

The matrix phase is created automatically using the capabilities of a mesh generator program by considering the specimen surface (external box) and excluding the Voronoï polyhedrons (aggregates). Notice that this is possible since the cohesive element methodology does not require an a priori definition of the possible fracture planes, since cracks are constrained to propagate following the inter-element boundaries ( [Roelfstra 85, Stankowski 90, Vonk 93, Caballero 06]).

With this method, we generated 2D (plane strain) square specimens with an external size  $h$  of  $0.1 \times 0.1 \text{ m}^2$ .

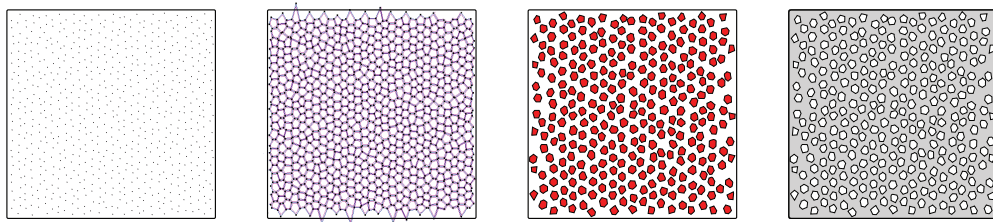


Figure 4.1: Schematics of the generation of concrete's meso-structure.

Meso-mechanical models need to be fed with specific material parameters, which may require specific experiments. In particular, fracture properties of the components (aggregate, matrix, which includes mortar and small aggregates, and aggregate-matrix interface) are needed.

In real concrete, the value of those parameters influences strongly the macroscopic mechanical behavior. In particular, the strength and stiffness of large aggregates (with respect to the matrix's ones) and the strength of the aggregate-matrix interface are directed correlated with the final experimental results, *i.e.* cracking patterns, fracture energy, critical crack opening, softening curve and Young's modulus ( [Guinea 02]).

This work only considers mean values of those parameters. Nevertheless two different types of aggregates have been considered. In Table 4.1, a summary of the chosen material parameters is given. In order to validate our model, we have performed two simulations using the same specimen geometry of the quasi-static tests presented in one of the references ( [Rosselló 04]) from which the aggregate and matrix properties have been taken. The numerical results lie within the experimental scatter and were therefore in good agreement with the experimental load displacement behavior.

### 4.2.1 Measure of damage

When using continuum damage models, damage is defined as a variable at the constitutive level. The visualization of this variable can therefore give an approximate idea about the irreversible deformation of a structure and the underlying damage. On the contrary, with the

## Chapter 4. Influence of the meso-structure in dynamic tensile loading

Table 4.1: Summary of fracture material properties taken from [Rosselló 06, Rosselló 04].

Material properties	Density [Kg/m <sup>3</sup> ]	E [GPa]	$\nu$	$G_c$ [J/m <sup>2</sup> ]	$\sigma_c$ [MPa]
Hard Aggregate	2700 <sup>a</sup>	19	0.2	60	16
Soft Aggregate	2700 <sup>a</sup>	2.1	0.2	20	1.7
Matrix	2200 <sup>a</sup>	31	0.2	52	4.7
Aggretate-Matrix	-	-	-	30	4.7 <sup>b</sup>

<sup>a</sup>These values are generic and chosen from [Caballero 05]

<sup>b</sup>This is an estimated value, set equal to the matrix-matrix interface strength, as direct experimental data was not found.

cohesive element approach, cracks are modeled explicitly, giving an opportunity to construct relevant damage indicators and to monitor their time evolution. To this effect, we defined the following variable.

### Damage normalized fracture work (DNFW)

The index accounts for the ratio between the work fracture spent (already dissipated fracture energy  $W$ ) and the fracture energy necessary to split the interior specimen in two. I.e. it is the fracture energy corresponding to a length equal to  $h$ , which is the specimen width (this allows to have an index insensitive to the mesh size).

$$DNFW = \frac{\sum_{i=1}^{nb \text{ interfaces}} \int_{l_i} W_i dl_i}{\bar{G}_c \cdot h} \quad (4.1)$$

Where  $l_i$  is the length of cohesive element  $i$ ,  $W_i$  the partially dissipated cohesive energy and  $\bar{G}_c$  represents a mean fracture energy, weighted with respect to the amount of fracture energy potentially released by each inter-element component. In order to distinguish and to localize damage, the above damage variable has been also defined for each material phase: aggregates, matrix and aggregate matrix, and can be identified (as for the other variables) with a corresponding subscript:  $a$ ,  $a-m$  and  $m$ .

## 4.3 Results

### 4.3.1 Geometry and boundary conditions

All the specimens are loaded under displacement control. To avoid stress wave propagation from the boundaries and early fracture near the boundaries, all the nodes are given an initial velocity, ([Miller 99]), see Figure 4.2. Nodes of the finite-element mesh which are located on

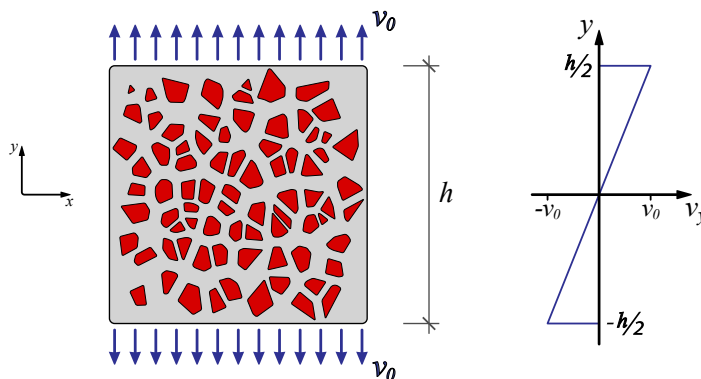


Figure 4.2: Boundary (left) and initial (right) conditions.

the upper and lower boundaries are forced to move at a certain constant velocity  $v_0$ :

$$v_0 = \dot{\epsilon} \frac{h}{2} \quad (4.2)$$

where  $\dot{\epsilon}$  is the strain rate and  $h$  the height of the specimen. The initial velocity of the nodes is therefore given by

$$v_y(y) = \frac{2v_0}{h} y \quad (4.3)$$

In the following subsections the work is focused first on the convergence of the simulations 4.3.2; later an investigation on the influence of the aggregates toughness 4.3.3 and their ordering 4.3.4 and size 4.3.5 is given.

#### 4.3.2 Effect of mesh size, geometry and material parameters

The fracture process in brittle solids is usually assumed to be a toughness controlled phenomenon, which means that the process is controlled by  $G_c$  and is therefore independent of  $\sigma_c$  of the cohesive zone.

Conversely, if the macroscopic strength is linked with  $\sigma_c$ , the process is said to be strength controlled. This must be valid not only theoretically but also when running a numerical simulation, which uses the cohesive zone approach. As already exposed in Subsection 3.2.4, the relationship between the cohesive law and the critical energy release rate  $G_c$  introduces a length scale into the material description, which is called cohesive zone length (see Equation 3.39). This imposes a constraint on the mesh size. This length has an important influence around the crack tip in numerical simulations. In general, for toughness-controlled fracture, the relation of Equation 3.40 has to be satisfied. This means that the cohesive zone must contain several elements (typically around four) and that the cohesive zone should be small in

## Chapter 4. Influence of the meso-structure in dynamic tensile loading

comparison to the specimen size. Table 4.2 shows the calculated values of the cohesive zone length for the different components of concrete. Note that it is not possible to clearly calculate a

Table 4.2: Cohesive zone lengths  $l_z$  [mm] for the different components of concrete meso-scale model. For Aggregate-Matrix interfaces:  $E_M$ ,  $E_{HA}$  and  $E_{SA}$  refer to the Young's Modulus of the matrix, the hard aggregates and the soft aggregates respectively.

Material	Hard Aggregate	Soft Aggregate	Matrix	Aggregate-Matrix		
				$E_M$	$E_{HA}$	$E_{SA}$
$l_z$ [mm]	4.1	13.4	67.2	38.8	23.7	2.6

cohesive zone length for the interfaces between aggregates and matrix (because the choice of Young's modulus is ambiguous). The cohesive zone length for the hard aggregates and the one between soft aggregates and matrix have the smallest values; therefore they will determine an upper limit for the size of the elements when generating the mesh. In order to verify the relationship between the different length scales a series of numerical tests was carried out. A first test was simply to load the 0.1x0.1 m concrete specimen varying the degree of refinement of the mesh in order to verify the mesh sensitivity. We ran several simulations for concrete with soft and hard inclusions for different loading rates. The results for two different loading rates and concrete with soft aggregates are reported in Figure 4.3. From Figure 4.3a it is possible to

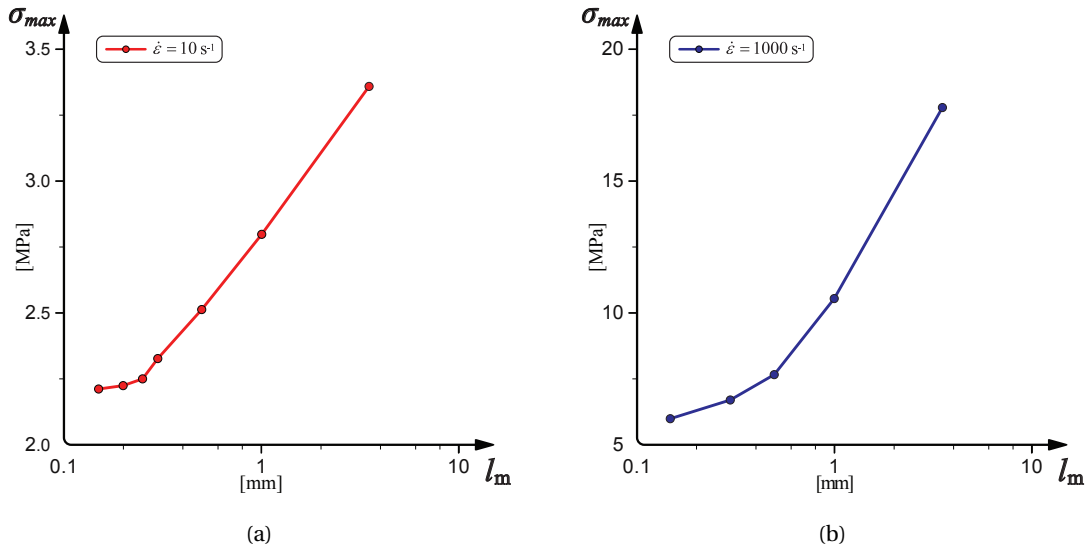


Figure 4.3: Macroscopic peak strength  $\sigma_{max}$  [MPa] versus average element size  $l_m$  [mm] for (a)  $\dot{\epsilon} = 10 \text{ s}^{-1}$  and (b)  $\dot{\epsilon} = 1000 \text{ s}^{-1}$  (with soft aggregates).

observe that there is convergence for an average element length ( $l_m$ ) smaller than about 0.25 mm. Considering this length and looking back at Table 4.2 we can remark that  $l_m$  should be at



least roughly ten times smaller than the Rice's cohesive zone length of the interface, which was derived for pre-cracked specimen with homogeneous materials and without meso-structure. Most published work having recourse to the cohesive-element framework use an estimate of  $l_m \leq l_z/3$ . Our work demonstrates the importance of using a more conservative estimate in the absence of a complete mesh-convergence study. The scenario is similar at high strain rates (e.g. beyond  $100 \text{ s}^{-1}$ ), Figure 4.3b, although the peak strength is higher and apparently a finer mesh is needed to reach fully converged results. The chosen mesh-size for the simulations presented in this chapter is set to 0.4 mm. Although this value seems to be related with some limited mesh dependency, it allowed us to save some computational time.

A closer inspection of Table 4.2 reveals yet another challenge. The matrix cohesive length has roughly the same dimension of the tested specimen; therefore the relation of Equation 3.39 is not respected. We carried out a second study in order to highlight the influence of this second requirement on the macroscopic strength. A pre-cracked specimen (Figure 4.4a), made only of one component, has been chosen for this test. The specimen is loaded with a strain rate of  $10 \text{ s}^{-1}$ , the horizontal displacements of the left-boundary nodes were blocked and the matrix-component was selected as reference material. We ran different calculations keeping  $G_c$  constant ( $52 \text{ J/m}^2$ ) and varying the critical opening strength  $\sigma_c$  between 1.175 MPa ( $0.25 \times \sigma_{c,m}$ ) and 75.2 MPa ( $16 \times \sigma_{c,m}$ ). According to the previous investigation of convergence, the mesh has been refined in the fracture area, where the elements have an average edge length of 0.5 mm.

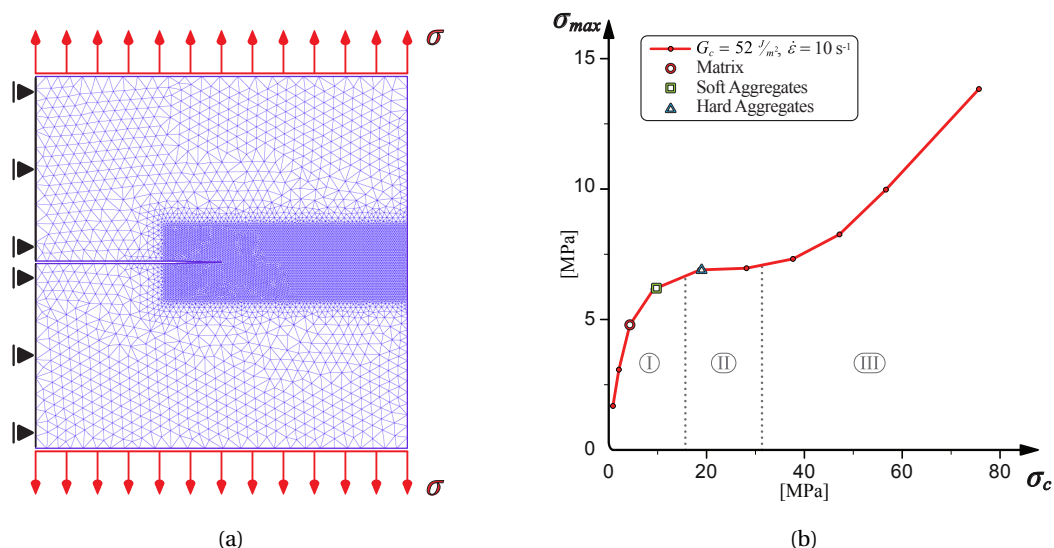


Figure 4.4: (a) Mesh of the pre-cracked specimen. (b) Evolution of the macroscopic peak strength  $\sigma_{max}$  varying  $\sigma_c$ . The square and triangular symbols are located in the plot with the same cohesive length as for soft respectively hard aggregates.

The results are displayed in Figure 4.4b. One can distinguish three domains. On the first one as

## Chapter 4. Influence of the meso-structure in dynamic tensile loading

on the third one, the macroscopic strength is clearly an increasing function of  $\sigma_c$ , while region two is staying quite constant. The domain two is clearly the toughness-controlled regime, whereas domain one and three are strength-controlled.

On domain one,  $l_z$  is bigger than 0.01 m, which is a too big value compared to the specimen size  $h$  (0.1 m). On the third domain the cohesive zone becomes too small compared to the size of the chosen mesh ( $l_z < 2.5$  mm), which means that the mesh is not fine enough to capture the cohesive zone. The cohesive lengths for matrix (round symbol) and soft aggregates (square symbol) are included in domain one. Whereas, for hard aggregates (triangular symbol), the cohesive length is located in the toughness-controlled region (domain two).

We further carried out two tests to quantify the influence of the chosen specimen size on the peak strength. Both tests are conducted for a fixed mesh size. One consists in taking a specimen with a regular meso-structure and the standard geometry tested in this chapter (0.1 x 0.1 m), but with a pre-crack. The specimen width has been increased by keeping the height constant (Figure 4.5). We could observe (Figure 4.6a) that the peak strength decreases

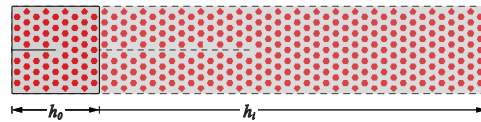


Figure 4.5: Pre-cracked specimen with variable width.

with increasing  $h$  and converges to a fixed value for a width of approximately 0.6 m (which corresponds roughly to ten times the cohesive zone length for the matrix).

The other test consists in enlarging the size of the specimen keeping the same degree of mesh refinement (Figure 4.6b). We have run simulations with double and quadruple specimen sizes. In this case the size does not seem to affect the peak strength (only a small variation in order of two percent could be observed). When comparing the results of the two specimens, one can remark that, if there is a pre-crack, the size of the specimen clearly affects the peak strength as the cohesive length of the matrix is in the same order as the chosen specimen width. Whereas, if the sample is not pre-cracked, it seems that the chosen size has not the same influence (as long as the chosen specimen size can be considered a representative volume element). For the chosen specimen geometry, and material parameters, the presented results are not in a well-defined regime. We have tried to reduce as much as possible the mesh dependency, but this is complicated by the presence of a meso-structure. The concept of toughness-controlled regime applies well for homogeneous materials and pre-cracked specimen. However, in our case, where multiple cracks are opening (during the simulations) and interacting, the upper limit for the specimen size of Equation 3.40 has to be relaxed. Moreover, because of the meso-structure, which is composed of different materials, it is not possible to clearly define a cohesive zone length. Without a rigorous estimate, it was decided to use a mesh size smaller than a quarter than the smallest cohesive zone estimate.

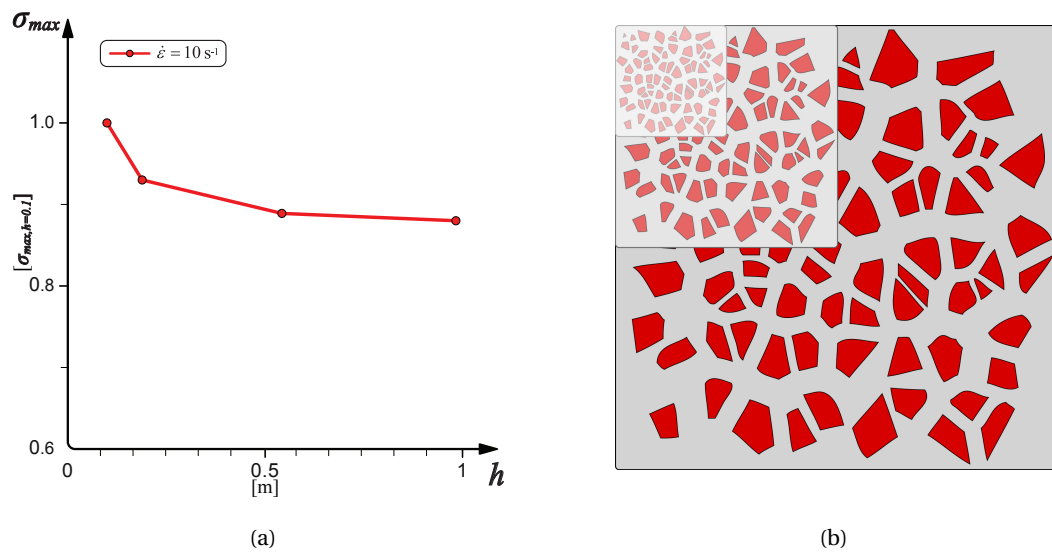


Figure 4.6: (a) Macroscopic normalized peak strength  $\sigma_{max}$  versus specimen with  $h$  [m] and (b) specimens with double and quadruple size.

Thus, it can be concluded that, for the geometry of the concrete specimens presented in this chapter, the present work lies in a mixed strength-controlled and toughness-controlled regime.

#### 4.3.3 Soft vs. Hard aggregates and strain rate effect

To study the influence of the mechanical properties of the aggregates on the behavior of concrete, two different types of aggregates, differing in their material properties, have been considered: soft and hard (see Table 4.1). The concrete meso-structure is modeled with the geometry and mesh presented in Figure 4.7. The response of the two types of concrete

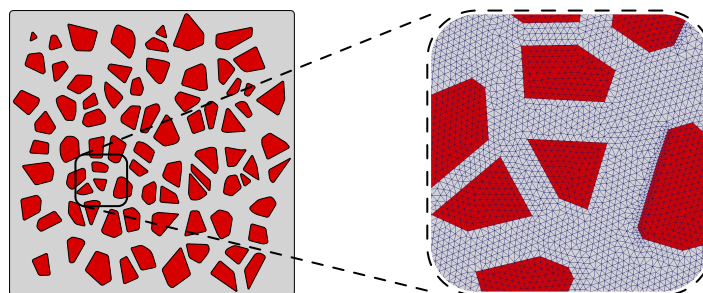


Figure 4.7: Concrete meso-geometry with 79 aggregates (left). Zoom of the corresponding finite-element mesh (right).

depends on the strain rate at which the specimen is loaded. For instance, two stress-strain

## Chapter 4. Influence of the meso-structure in dynamic tensile loading

diagrams are plotted in Figure 4.8; (a) for a low strain rate ( $\dot{\epsilon} = 10 \text{ s}^{-1}$ ), (b) for a high strain rate ( $\dot{\epsilon} = 1000 \text{ s}^{-1}$ ). From Figure 4.8a one can recognize that the aggregate type influences the

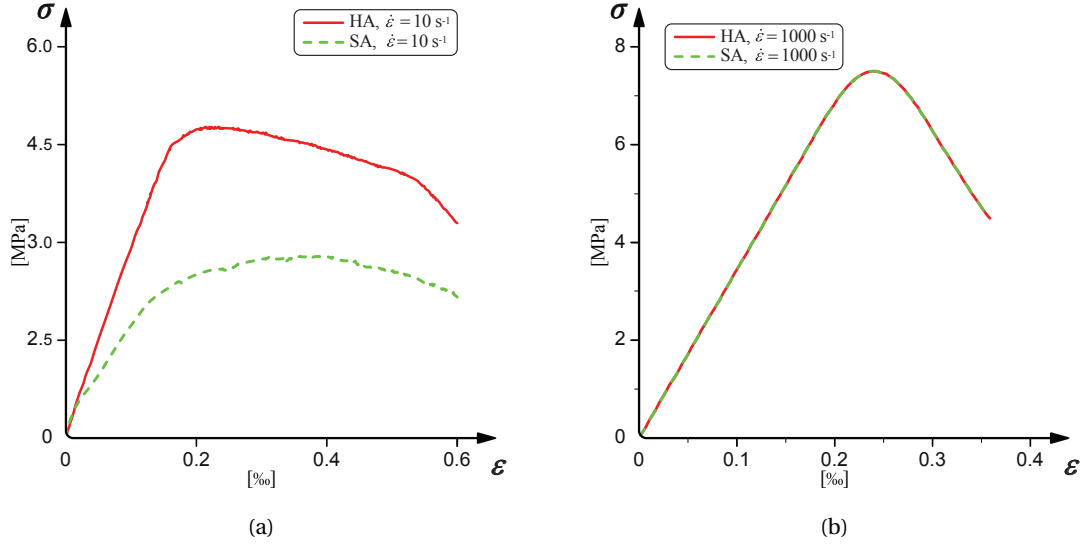


Figure 4.8: Macroscopic stress-strain ( $\sigma - \epsilon$ ) comparison between hard and soft aggregates: (a) at low strain rate ( $\dot{\epsilon} = 10 \text{ s}^{-1}$ ) and (b) at high strain rate ( $\dot{\epsilon} = 1000 \text{ s}^{-1}$ ).

response of the concrete specimen only at low strain rates. As mentioned previously, we keep the value of  $\beta$ , the coupling parameter in the cohesive law, equal to 1. Since we are in mode I, this parameter does not influence significantly the peak strength (a study of the influence of  $\beta$  was conducted but is not shown here). The variation of peak strength with strain rate for the two different aggregates is highlighted in Figure 4.9a. The results display a strain rate hardening. However, the computed increase of strength is smaller than the experimental one, see Figure 4.9b. We will go back to this point in the discussion section, where we motivate the use of a phenomenological rate dependent cohesive law.

Under a low strain rate, the presence of soft aggregates within concrete makes the material softer in its pre-peak behavior. However, this effect starts to disappear when the strain rate is increased above  $10 \text{ s}^{-1}$ . The peak strength is also decreased by the presence of soft aggregates when concrete is loaded under low strain rates (the peak strength for hard aggregates is approximately double than for the soft ones). Finally, at low  $\dot{\epsilon}$  the softening branch shows a more attenuated decay when comparing soft vs. hard aggregates.

This scenario changes completely when analyzing the same specimens under high strain rate, Figure 4.8b. The results show that there are no differences between soft and hard aggregates in terms of stress-strain diagrams. The stress-strain plots are, almost identical, exhibiting same elastic slope, peak strength and softening decay up to the last computed time.

The same distinction between the behavior at low and high strain rates can be done when

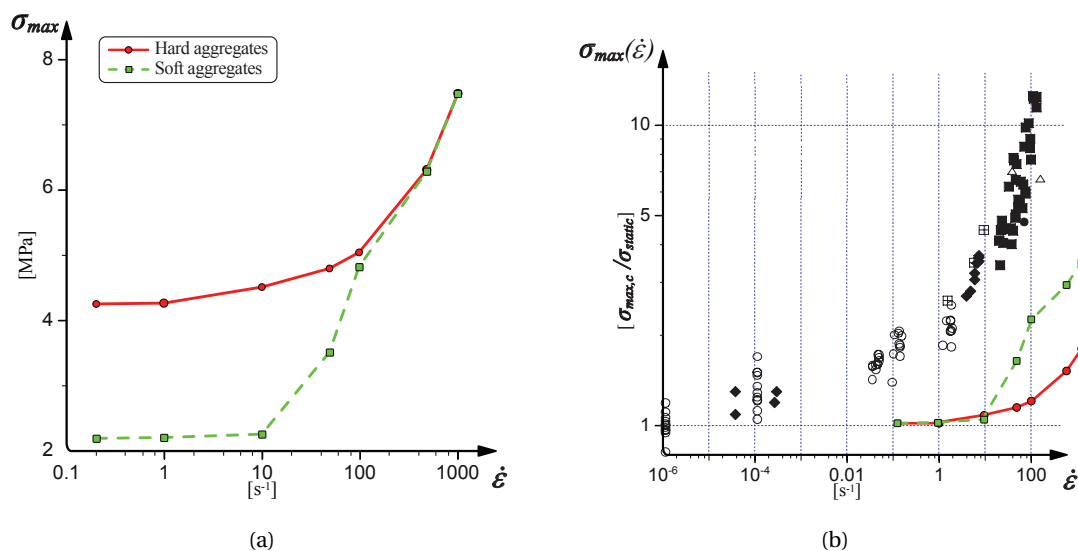


Figure 4.9: (a) Macroscopic peak strength  $\sigma$  [MPa] – strain rate  $\dot{\epsilon}$  [s<sup>-1</sup>] for soft and hard aggregates for a rate independent law. (b) Comparison with experimental values extract from [Brara 06], which itself has used the following experimental data: [Brara 99, Ross 95, Birkimer 68, Toutlemonde 94, Mc Vay 88, John 92] (note that the vertical axis is normalized by the static strength).

looking at the deformed mesh configuration, which is plotted in Figure 4.10 for the two different types of aggregates. One can remark in the case of hard aggregates, that at low strain

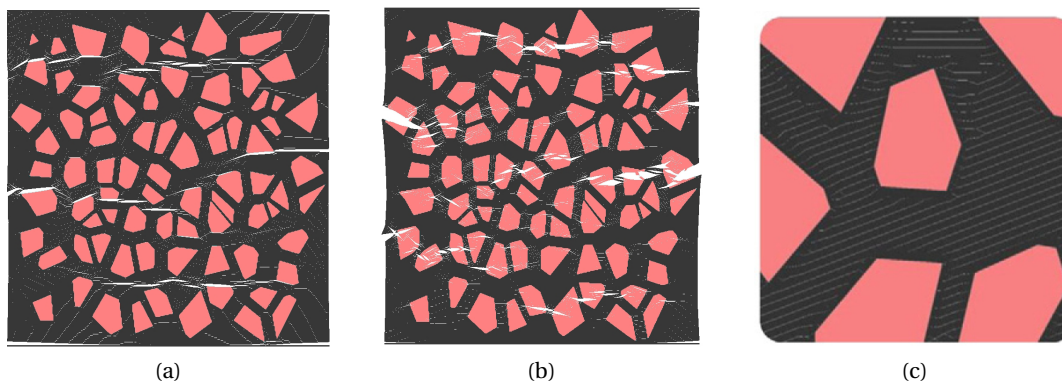


Figure 4.10: Crack propagation in the mesh: at low strain rate for hard (a) and soft (b) aggregates, at high strain rate (c) just one zoom is showed (crack nucleation occurs everywhere in the matrix independently of aggregate type).

rates some macro-cracks propagate in the matrix avoiding the aggregates, whereas the cracks cross the aggregates if soft inclusions are chosen. Therefore the failure process is dominated by crack propagation. By increasing the loading rate cracks start to nucleate in the matrix and

## Chapter 4. Influence of the meso-structure in dynamic tensile loading

have less time to propagate before the peak strength is reached. At high strain rates ( $1000 \text{ s}^{-1}$ ) the crack path for soft and hard aggregates is the same. This means that there the peak strength is dominated by crack initiation.

This phenomenon can also be highlighted when considering the damage normalized fracture work. Figure 4.11 shows the damage diagrams for each of the different concrete phases:

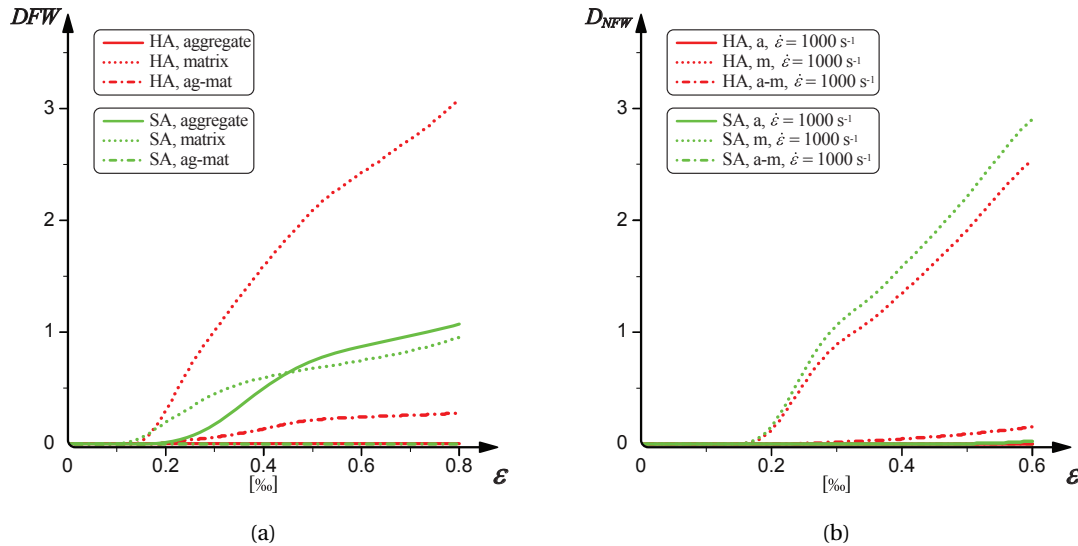


Figure 4.11: Damage on aggregates, matrix and interfaces vs. tensile-strain. Comparison between soft and hard aggregates: (a) low strain rate, (b) high strain rate.

aggregates, matrix and aggregate-matrix interfaces respectively. In all figures, damage is plotted against the total tensile strain applied to the specimen, which is measured as the total elongation divided by the original length of the specimen. Soft aggregates (SA) are compared vs. hard aggregates (HA) under both: (a) low and (b) high strain rates.

As noticed from the deformed mesh configuration, under a low strain rate, hard aggregates do not experience any damage, whereas the damage on soft aggregates increases with increasing strain level. For both aggregates the damage in the matrix appears first. This is congruent with the fact that at early stages of loading, *i.e.* before peak strength, a large amount of micro-cracks starts to be nucleated within the matrix. With increasing strain those micro-cracks begin to propagate and therefore damage outside from the matrix phase can begin.

When a tensile wave travelling throughout the matrix reaches an aggregate, it induces a tensile strain on it. However, the deformation that the aggregate will experience will depend on the Young's modulus ratio between the matrix and the aggregate. Thereby, the stiffer is the aggregate with respect to the matrix, the lower the deformation on the aggregate will be. This implies a larger opening of the interface. Therefore, the introduction of aggregates much harder than the surrounding matrix will concentrate the damage on the interfaces rather than

in the inclusions as in the case of soft aggregates.

Damage in the matrix for hard aggregates is also higher when compared with soft aggregates. This agrees with a larger value of dissipated fracture energy and higher peak strength. After the peak strength has been reached and the softening behavior starts to be more accentuated the rate of fracture energy dissipation decreases for the damage indicators of the three components.

At high strain rates the damage is localized mainly in the matrix. The high loading rate does not allow cracks to propagate before the peak strength has been reached. Micro-cracks start to nucleate everywhere in the matrix, which displays the highest stress wave speed and therefore crack propagation speed too. This more diffuse micro-cracking is related to the intrinsic characteristic opening time of the cohesive law (derived in [Camacho 96]). Therefore, for our computations, we cannot explain the increase of strength with a more transgranular fracture ([Yan 06]).

Interestingly, the dissipated fracture energy at peak strength seems to be only slightly affected by the loading rate. However, post-peak dissipation of energy rises with increasing strain rate and is clearly an increasing function of the loading velocity.

The presence of two different types of inclusions not only affects the damage value but also the crack pattern and its evolution. To this fact we consider the variable,  $N_{clusters}$ , which accounts for the number of “clusters” present in the specimen. A cluster is a group of cracks (*i.e.* a group of fully broken interfaces for which the opening of the cohesive elements is beyond  $\delta_c$ ), which are interconnected to each other.

In general there is a relation between strain rate and when the clusters appear. Relatively, a higher strain rate delays the formation of the first clusters. At low strain rates ( $10 \text{ s}^{-1}$ ), the first clusters appear for soft aggregates just before the peak strength has been reached, whereas for hard aggregates they appear immediately after (the process being more energy consuming). With increasing strain rate, the clusters will appear only when a bigger amount of fracture energy has been spent and the peak strength will be reached with a more diffuse nucleation of micro-cracks. Unlike for ceramics where the material breaks down when a cluster has reached a length corresponding approximately to the specimen size ([Kraft 08]), it seems that it is not possible to find a critical cluster length to be related with the failure of the material.

#### 4.3.4 Ordered vs disordered meso-structure

This section discusses the effect that the meso-structure has on the final fracturing behavior of concrete. The main target is to evaluate what is the influence of the location of aggregates and their external shape. Three different meso-structures are considered:

- Fully uniform, where all the aggregates have the same shape (excepted those located near to the borders due to the Voronoï generation process), same orientation and are



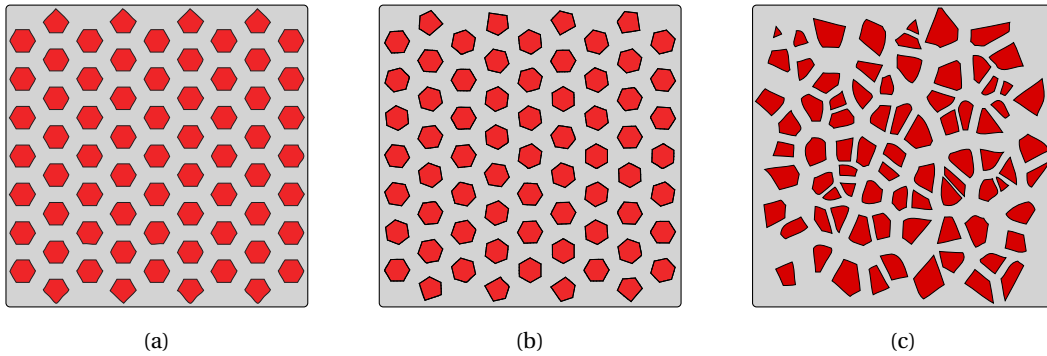


Figure 4.12: Different meso-structures: (a) uniform aggregates (U), (b) rotated aggregates ( $U_{Rot}$ ) and c) completely random (R).

uniformly distributed. This distribution will be referred as U.

- Fully uniform plus random rotation, where as in the previous distribution all the aggregates have same external shape but they are randomly rotated with respect to their own center. This distribution will be referred as  $U_{Rot}$ .
- Fully random, aggregate's shape and position are randomly assigned. This distribution will be referred as R.

Figure 4.12 shows the three different meso-structures considered. All the meso-structures have the same ratio of aggregate volume, 30%, although due to the randomness they differ in the number of aggregates. Thus, U and Rot meso-structures have 67 aggregates of approximately 8.5 mm whereas R distribution has 79 aggregates, where most aggregates have sizes between 6 and 10 mm. All the computations have been carried out considering particles as hard aggregates, since the influence of the meso-structure is not significant for the soft inclusions (which are weaker than matrix grains interfaces). Figure 4.13 plots the stress-strain diagrams for the different meso-structures under low (Figure 4.13a) and high (Figure 4.13b) strain rate. From Figure 4.13 we can extract the following conclusions.

The initial elastic slope is not affected by the meso-structure.

The peak strength is always lower for the U distribution. This is probably due to the fact that, in the U distribution, all the aggregates have two faces orthogonally aligned to the loading direction, which reduces the maximum strength. Indeed, considering the dissipated fracture energy of the interfaces (Figure 4.14) for the U specimen, one can remark that it is larger than those of the other two meso-structures ( $U_{Rot}$  and R). On the contrary, the dissipated fracture energy of the matrix is smaller for the U specimen.

The preferential direction of failure is avoided in the  $U_{Rot}$  and R distributions. Comparing  $U_{Rot}$  and R specimens, the fully disordered meso-structure increases the possibility of having



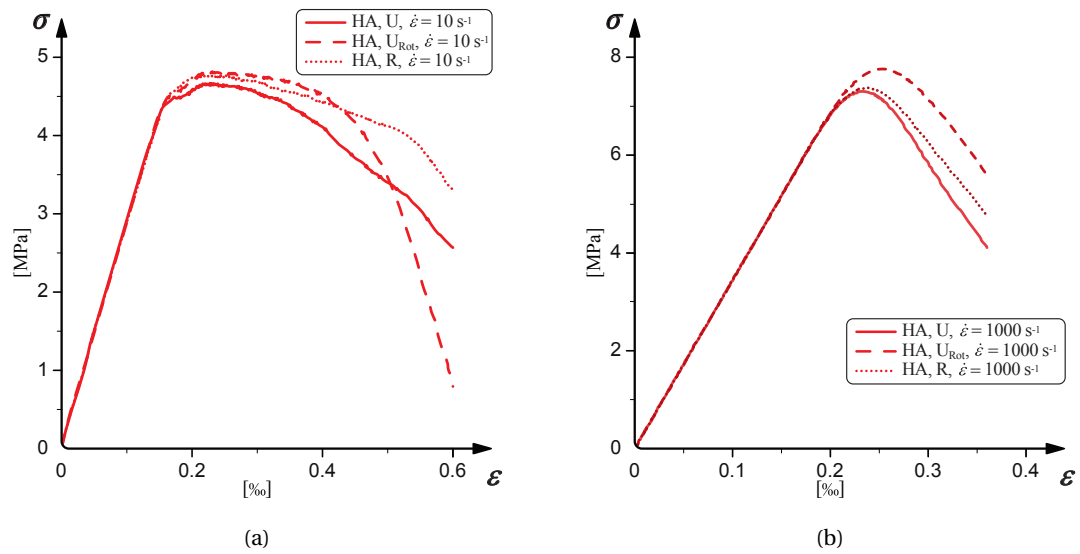


Figure 4.13: Stress-strain diagrams obtained for the three different meso-structures under (a) low and (b) high strain rate.

weak zones (grain-matrix interfaces are closer in some places). In such regions, damage might grow faster and therefore the global mechanical response softens earlier.

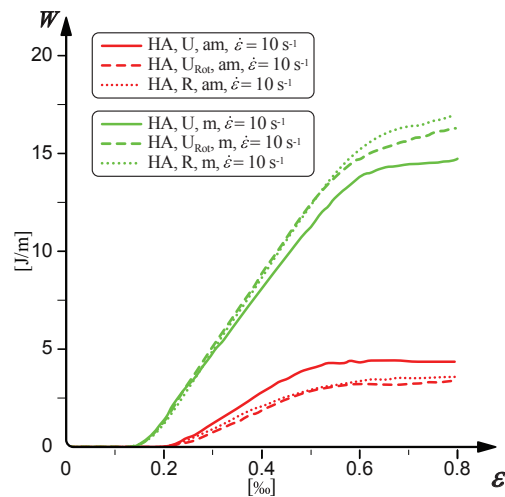


Figure 4.14: Dissipated fracture energy for the matrix (in green) and interfaces (in red) vs. tensile strain. Comparison between specimens with the three different meso-structures.

Finally, material softening is slightly more attenuated in the R distribution. As mentioned before, the R distribution contains “weak zones”, which facilitates the initiation of cracks and

their local growth. However, after an initial growth and nucleation of cracks, the disordered meso-structure may obstruct the further propagation of cracks (we are under the assumption of hard aggregates), and forces the cracks to deviate around the aggregates, which requires more energy (the dissipated fracture energy in the matrix of the R distribution is slightly higher compared with the one of  $U_{Rot}$  distribution).

### 4.3.5 Influence of aggregate's size

In this section the effect of the aggregate's size is analyzed. Three different specimens with the

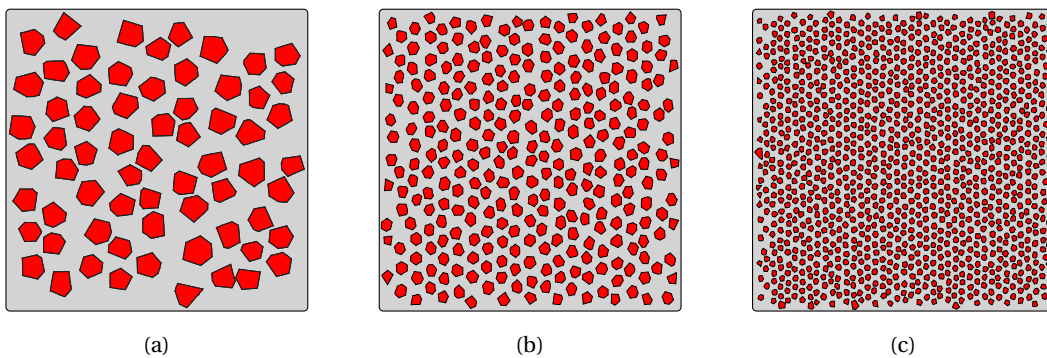


Figure 4.15: Specimens with different mean size of aggregates: (a) 66 aggregates, (b) 297 aggregates and (c) 1198 aggregates.

same standard geometry of  $0.10 \times 0.10 \text{ m}^2$  are considered. In all specimens, volume ratio of aggregates is kept constant and equal to 30%, whereas the size of the aggregate is decreased as the number of inclusions is increased. The average aggregate size of each specimen is: 8.5 mm, 3.9 mm and 2 mm (corresponding to a number of aggregates of 66, 297 and 1198). The three different specimens considered are shown in Figure 4.15. Both types of aggregates, soft and hard, are considered.

Figure 4.16 shows the obtained stress-strain diagrams for the different concrete specimens under low and high strain rates. At both loading rates the elastic modulus appears to be independent of the aggregate size. At low loading speed the peak strength for hard aggregates is not significantly affected by the number of inclusions (not shown in figure). Whereas, for soft aggregates, it is possible to notice an increase in peak strength with increasing number of aggregates (Figure 4.16a).

In a concrete material with large aggregates (which represent weak zones in the case of soft aggregates) cracks can nucleate before and propagate easier within the inclusions than in a concrete with small aggregates. Indeed, cracks nucleate first in the matrix and then propagate from the matrix in the aggregates too. Therefore, if the aggregates are bigger, the cracks will cross them easier breaking a larger area of aggregates leading to lower peak strength.

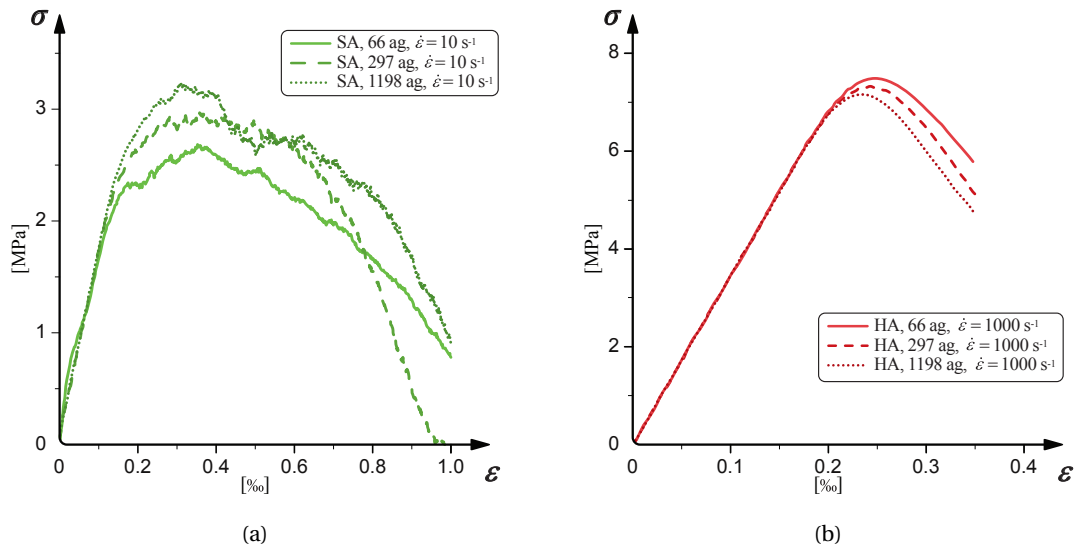


Figure 4.16: Stress-strain diagrams obtained for the different aggregate sizes under (a) low and (b) high strain rate.

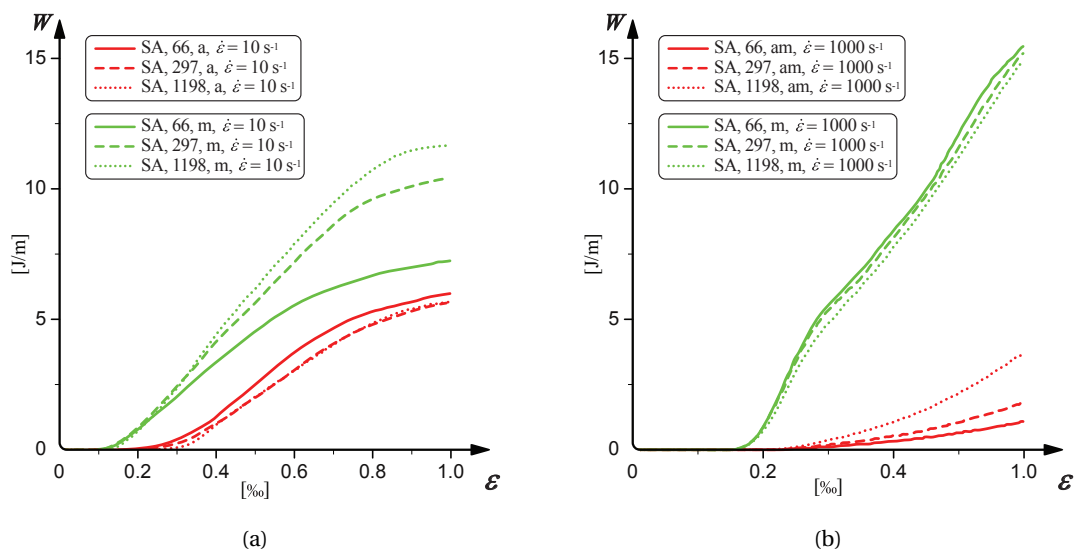


Figure 4.17: Dissipated fracture energy vs. tensile-strain. Comparison between specimens with 66, 297 and 1198 aggregates: (a) at low strain rate and (b) at high strain rate.

This phenomenon can also be observed when looking at the graph for the dissipated fracture energy (Figure 4.17a). The dissipated energy in the matrix increases with increasing number of aggregates. In contrast, the aggregate's dissipated energy reduces with decreasing size of inclusions.

The scenario changes when considering high strain rates (Figure 4.16b). In this case the peak strength is higher for large inclusions (independently of aggregate type). We recall that at high strain rate the cracks nucleate in the matrix and aggregate-matrix interfaces leading to a similar stress-strain behavior for the two types of inclusions. Therefore, even though aggregates seem not to be directly the cause of the variation of the strength, a larger number of aggregates implies also a higher probability for a growing crack to find an interface between mortar and aggregates (interfaces are weaker than matrix).

As shown in Table 4.3, for the same volume ratio of inclusions, the total length of the interfaces (between aggregates and mortar) increases roughly four times between the 66 and 1198 aggregates specimens. This is congruent with a decreasing ratio of dissipated fracture energy at the interfaces with increasing aggregates size (Figure 4.17b).

Table 4.3: Interface length between aggregates and matrix for the three different specimens.

Aggregate's number	66	297	1198
Interface length [m]	1.69	3.58	7.17

### 4.4 A rate-dependent cohesive law

In this section we discuss the limits of the proposed approach. Although, the presented meso-mechanical model is bound with a certain freedom, there are also some limitations. Indeed, (as noticed in the results section) one can remark that the strain-rate hardening obtained with the rate-independent cohesive law is not comparable with the experimental one. Moreover the dissipated fracture energy at peak in the simulations seems to be roughly independent of strain rate (however post peak dissipation of energy is clearly an increasing function of strain rate).

Experimental results have shown that energy dissipation increases with the loading rate [Rossi 94, Brara 07]. Although, there is a general agreement on this observation, it is still not clear what are the mechanisms or physics which govern it. The increase is attributed to two different aspects by different authors: structural or material. According to the structural effect hypothesis, the explanation resides in a more diffuse micro-cracking, which should be linked with higher fracture energy [Van Doormaal 94, Brara 07]. On the contrary, the material explanations sustains that the increase of toughness could be an effect of internal material "hardening" [Lambert 00]. We argue that this mechanism should be related to the chosen modeling scale.

I.e. when considering a large modeling scale (macro-scale), the toughness parameter of the cohesive approach could be a function of the loading rate, as the mesh size cannot be small enough to capture all micro-cracking mechanisms. Whereas, decreasing the scale should entail a rate independent toughness parameter.

Nevertheless, the small increase in strength with increasing loading rate in comparison to experiments seems to call for the introduction of a phenomenological rate-dependent cohesive law. Therefore, we decided to slightly modify the linear-decaying cohesive law in order to take into account the strain rate effect. Among the various possible laws, we identified two different ones differing in their shape and which are also function of different rate-dependent parameters.

The first variant [Zhou 05] assumes that the opening cohesive strength is a material constant value, while the critical opening displacement is a function of the crack opening rate.

Therefore the linear cohesive law is enriched with the following relationship for the rate-behavior of the critical opening:

$$\delta_c = \delta_{co} \left( 1 + \frac{\dot{\delta}}{\dot{\delta}_o} \right) \quad (4.4)$$

where  $\delta_{co}$  corresponds to the critical crack opening displacement for the rate-independent law (static value) and  $\dot{\delta}_o$  represents a scaling crack opening rate. The introduction of this rate-dependent crack opening increases the value at which complete separation of the cohesive zone occurs with increasing opening rate. This should also lead to a higher dissipated fracture energy, which could be related with a more diffuse micro-cracking that the actual meso-scale is not able to capture. We ran several simulations with this modified cohesive law for different

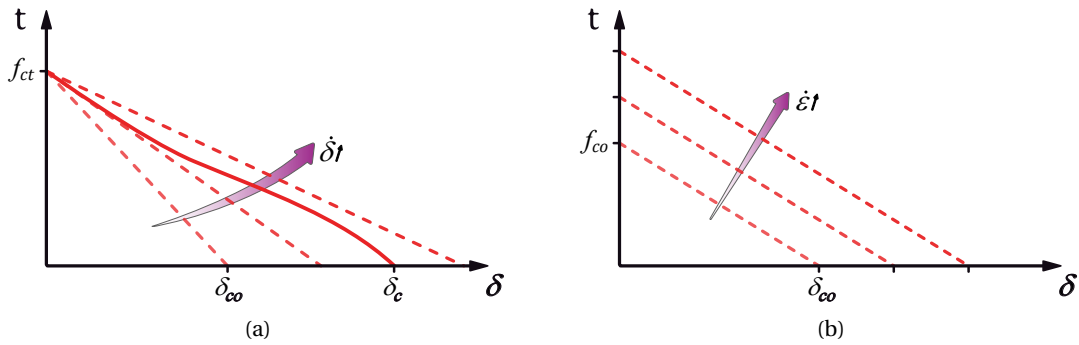


Figure 4.18: Two rate-dependent cohesive laws: (a) generalized cohesive law with crack opening displacement as a function of crack opening rate, (b) cohesive stress and crack rate, both function of strain rate.

loading rates in order to verify the strain rate-dependence. Surprisingly, we could not notice a remarkable difference in the peak strength values and dissipated fracture energy with the

## Chapter 4. Influence of the meso-structure in dynamic tensile loading

rate-independent law. This may be related with the chosen sample's size, for which one we are in presence of a mixed strength and toughness controlled regime. Therefore, we decided to use a second variant where both  $\sigma_c$  and  $\delta_c$  are sensitive to the loading rate. This results in a law, which expands outwards with increasing loading rate as shown in Figure 4.18a. The inconvenients with this kind of law is that the cohesive strength can be several times higher than the macroscopic material strength, which is physically questionable. Moreover, because we are assuming an initial rigid behavior (explicit approach), the cohesive strength needs to be known a priori. Therefore, we decided to link the law directly with the macroscopic loading ratio, introducing the following strain rate dependencies:

$$\sigma_c = \sigma_{co} \left(1 + \frac{\dot{\epsilon}}{\dot{\epsilon}_o}\right) \quad (4.5)$$

$$\delta_c = \delta_{co} \left(1 + \frac{\dot{\epsilon}}{\dot{\epsilon}_o}\right) \quad (4.6)$$

where  $\delta_{co}$  and  $\sigma_{co}$  correspond to the static values of cohesive strength and critical opening displacement respectively. Thus the two values are increased of the same amount with increasing loading rate (Figure 4.18b). Thanks to the simple loading condition and geometry of the

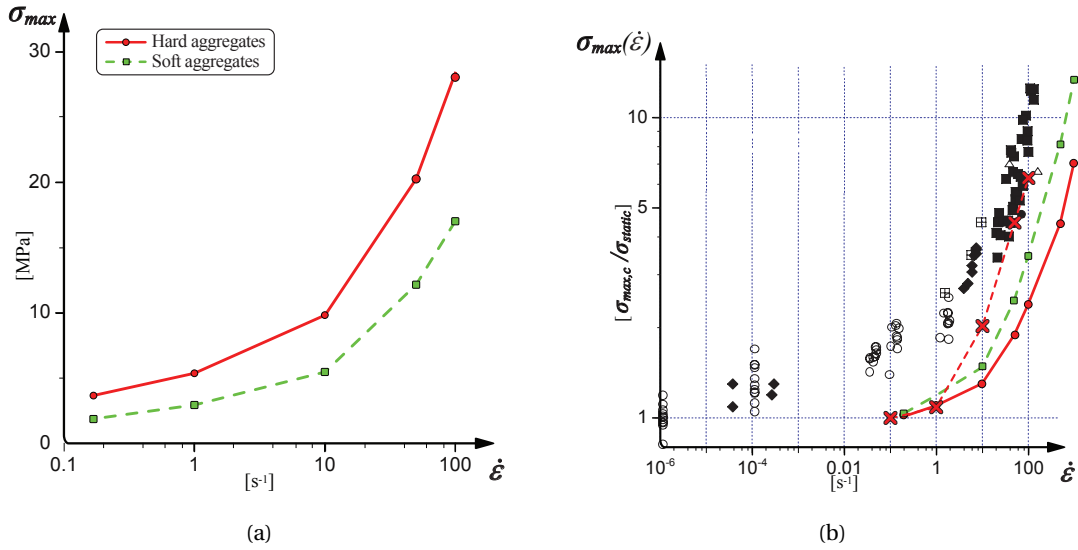


Figure 4.19: (a) Macroscopic peak strength  $\sigma$  [MPa] – strain rate  $\dot{\epsilon}$  [ $s^{-1}$ ] for soft and hard aggregates for a rate dependent cohesive law. (b) Comparison with experimental values extract from [Brara 06], which itself has used the following experimental data: [Brara 99, Ross 95, Birkimer 68, Toutlemonde 94, Mc Vay 88, John 92] (note that the vertical axis is normalized by the static strength).

presented specimens, this second variant has been implemented specifically for the proposed virtual experimental setup. For more complicated loading conditions, it would be necessary to bound the strain-rate dependence with the deformation rate of the four Gauss points adjacent

## 4.5. Additional analysis on rate dependency

to the inter-element boundary. Another possibility would be to take the static critical stress for insertion and to add, within the cohesive law, a rate-dependent viscosity parameter which depends on the opening rate (for instance [Kubair 03]). A different approach, which would not involve a cohesive-approach, would consist in having a visco-plastic bulk material (such as proposed in combination with a continuum damage formulation in [Hervé 05]).

As for the previous variant, we ran several simulations varying the loading rate. The resulting peak strengths are depicted in the graph of Figure 4.19a. One can remark that with this law the increase in peak strength and dissipated fracture energy is much more pronounced and is therefore closer to the experimental values (Figure 4.19b) and a better agreement can be simply reached by calibrating with the experimental values. The fit could be perfected by choosing a non-linear relationship for  $\sigma_c$  and  $\delta_c$  (Equations 4.5 and 4.6).

## 4.5 Additional analysis on rate dependency

This section presents an extension of the work presented in the chapter until here. We report here a summary of what was published in [Gatuingt 12]. For this new analysis the range of stiffness of the constituents, as well as the interface properties, has been enlarged to reproduce a concrete with more common material properties. The stiffness ratio between aggregates and mortar adopted until here is indeed quite low. Therefore a higher value for the Young's modulus of the inclusions has been considered (Table 4.5). This results in a stiffness ratio between heterogeneities and matrix of 3. Additionally, from the table it is possible to see that the estimated strength of the ITZ has been decreased with respect to the one of the matrix (in order to have the same value of the effective opening displacement for both matrix and ITZ). The effect of the stiffness of the aggregates on the macroscopic tensile behavior has thus been addressed. The study presents results of the influence of the meso-structure on the tensile strain-stress curve and on the dynamic increase factors for the tensile strength and dissipated fracture energy. Moreover we provide a comparison with experimental results on Split Hopkinson Bar (SHB) and modified SHB tests depicted in Figure 4.20. The derived data on strength and fracture energy of these tests are summarized in Table 4.4.

Table 4.4: Strength, fracture energy and dynamic/static ratio for these values for concrete at different loading rates (from [Weerheijm 07]).

	Load Rate $\dot{\sigma}$ [GPa/s]	Tens. Strength $f_t$ [MPa]	Fract. Energy $G_f$ [N/m]	$f_{t(dyn)}/f_{t(stat)}$	$G_{f(dyn)}/G_{f(stat)}$
Static	$10^{-4}$	3.3	120	1	1
SHB	39	5.58	120	1.7	1
Mod. SHB	1685	17.	1505	5.2	12.5

These experimental data show a rate effect on strength, and on the dissipated fracture energy, in the high loading rate regime. Table 4.4 also shows that for the higher loading velocity the

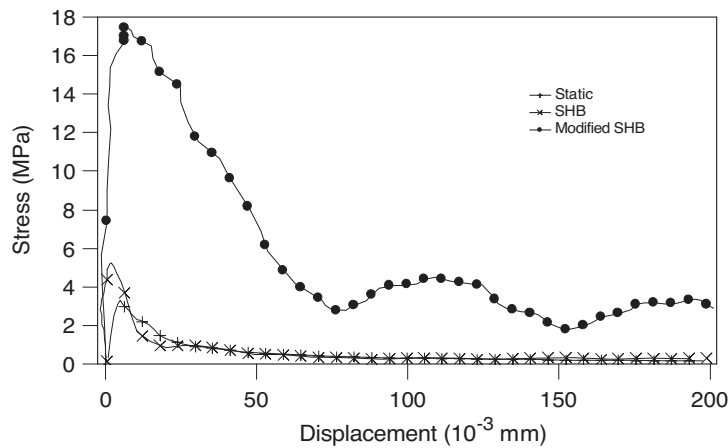


Figure 4.20: Experimental stress-displacement curves for static, SHB and Modified SHB tests (from [Weerheijm 07]).

dynamic increase factor is more important for the dissipated fracture energy than for the tensile strength. In addition, some authors have shown experimentally that the deformation capability of concrete under uniaxial tensile loading increases due to a rate effect [Kormeling 87, Oh 90, Rossi 94].

In several models it is common to introduce this dynamic increase factor directly in the macroscopic behavior (e.g. [Chambart 09]). However, this has to be done with care as it is not clear how much structural effects affect the dissipation of energy.

#### 4.5.1 Extended material parameters and meso-structure

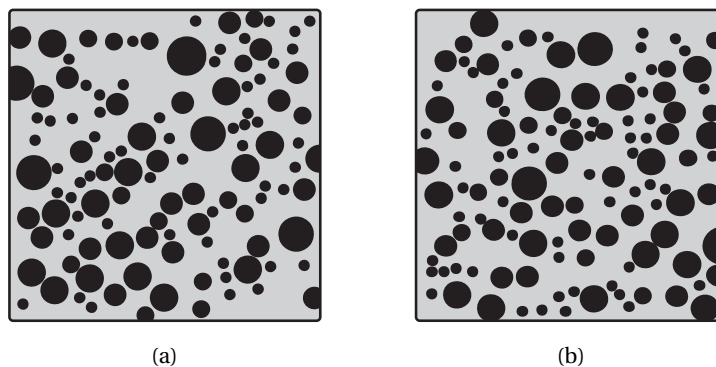


Figure 4.21: Two different meso-structures generated with the same aggregates size distribution.

For this study the geometry of the specimens has been generated according to a sieving method [EN 09]. The inclusions are represented with circles with a diameter ranging from 4



#### 4.5. Additional analysis on rate dependency

mm to 25 mm. Consequently, as in [N’Guyen 10a], knowing the aggregates size distribution, the number of perfect circular (in 2D) aggregates can be calculated.

Then, from the obtained image of the geometry the meshes can be generated using the PPM2OOF [Langer 09] public domain software created at the National Institute of Standards and Technology (NIST). This software superimposes a mesh on any image. The simplest meshing algorithm tries to divide each image pixel into two triangular elements. The chosen

Table 4.5: Material properties of concrete.

	Aggregate	Mortar	ITZ
Density – $\rho$ [Kg/m <sup>3</sup> ]	2700	2200	–
Young’s modulus – E [GPa]	75	25	–
Poisson’s ratio – $\nu$	0.2	0.2	–
Fracture Energy – $G_c$ [J/m <sup>2</sup> ]	60	50	30
Tensile Strength – $f_{ct}$ [MPa]	10	4	2.4
Cohesive zone length – $l_z$ [mm]	41	72	–

interface properties are summarized in Table 4.5. It is possible to notice that the tensile strength of the interfacial transition zone (ITZ) is lower with respect to the previous study. Its value is indeed estimated from  $G_c$  of the ITZ with  $\delta_c$  equal to the value obtained for the mortar. With this assumption one obtains a  $f_{ct}$  smaller in the ITZ than in the mortar, which is commonly accepted for a classical concrete.

In addition, also the ratio between the Young’s moduli of aggregates and cement paste reflects a common ratio for a standard concrete. A mesh sensitivity analysis (see [Gatuingt 12]) performed with different degrees of mesh refinement established that, although the peak strength convergence could be addressed, an element size of  $\approx 1$  mm is a little bit too coarse to have a good representation of the cement paste between two close aggregates. However, for smaller element sizes the response of the specimens converged for the entire range of applied loading velocities. Consequently, the average element size has been set to 0.5 mm.

#### 4.5.2 Influence of the specimen size

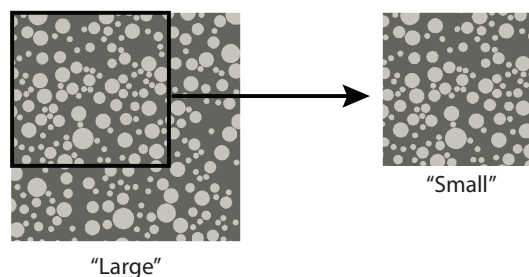


Figure 4.22: Large vs small size of the specimen.

## Chapter 4. Influence of the meso-structure in dynamic tensile loading

In order to quantify the influence of the specimen size on our results, we generate a large sample from which we cut out a smaller one. This in order to have the same aggregate/paste ratio and the same aggregate arrangement (see Figure 4.22) for both specimens. The large sample has a surface  $S_L = 0.15 \times 0.15 \text{ cm}^2$  while for the small one  $S_S = 0.1 \times 0.1 \text{ cm}^2$ . The consequence is that we increase the width of the sample of 50% and the surface of 225%. Figure 4.25 and Figure 4.23 show the results obtained for two different loading rates ( $\dot{\epsilon}=1\text{s}^{-1}$

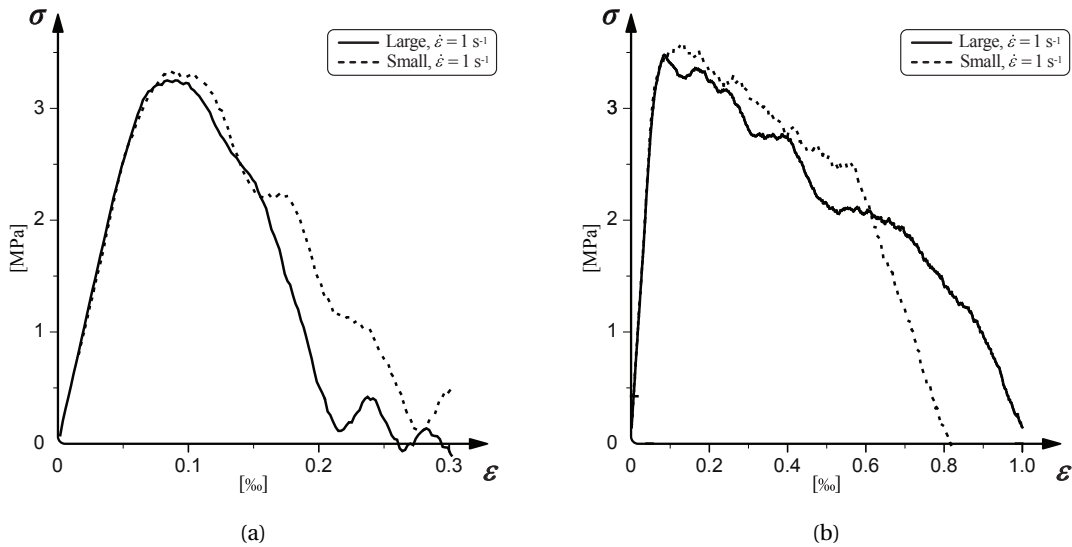


Figure 4.23: Influence of the specimen size on the stress-strain curves: (a)  $\dot{\epsilon} = 1\text{s}^{-1}$  (b)  $\dot{\epsilon} = 10\text{s}^{-1}$ .

and  $\dot{\epsilon}=100\text{s}^{-1}$ ). We can notice that the crack path obtained is very similar for the two sample sizes. This result is confirmed with the macroscopic stress-strain responses of the specimens. Nevertheless we can observe that the peak strength is a little bit smaller for the large sample compared to the small one. This size effect in quasi-brittle materials such as concrete is a well known phenomenon and there are a number of experimental and theoretical studies (see for example [Reinhardt 81, Bažant 84, Ožbolt 94]) which confirm the existence of it. Moreover in the Figure 4.23 the post-peak response is clearly different for the two sample sizes. This result is not surprising because the post-peak response is more governed by the fracture energy. This is confirmed in Figure 4.24a where the evolution of the dissipated fracture energy (per unit sample depth) is plotted for different strain rates. As expected, for a larger sample we obtain a higher dissipated energy. If we assume an horizontal single crack, we can divide this energy by the width of the specimen and plot a normalized dissipated fracture energy (Figure 4.24). In this figure we can see that the assumption of a single crack is not so bad for the lower strain rate ( $\dot{\epsilon} = 1\text{s}^{-1}$ ) where a “single” crack appears (Figure 4.25). For higher strain rates ( $\dot{\epsilon} = 100\text{s}^{-1}$ ), due to the multiple cracks this assumption is no longer true and the normalized dissipated fracture energy strongly depends on the specimen size. The larger the sample, the bigger is the Dynamic Increase Factor (DIF). In our case, we obtain a DIF equal to 8 for the smaller

#### 4.5. Additional analysis on rate dependency

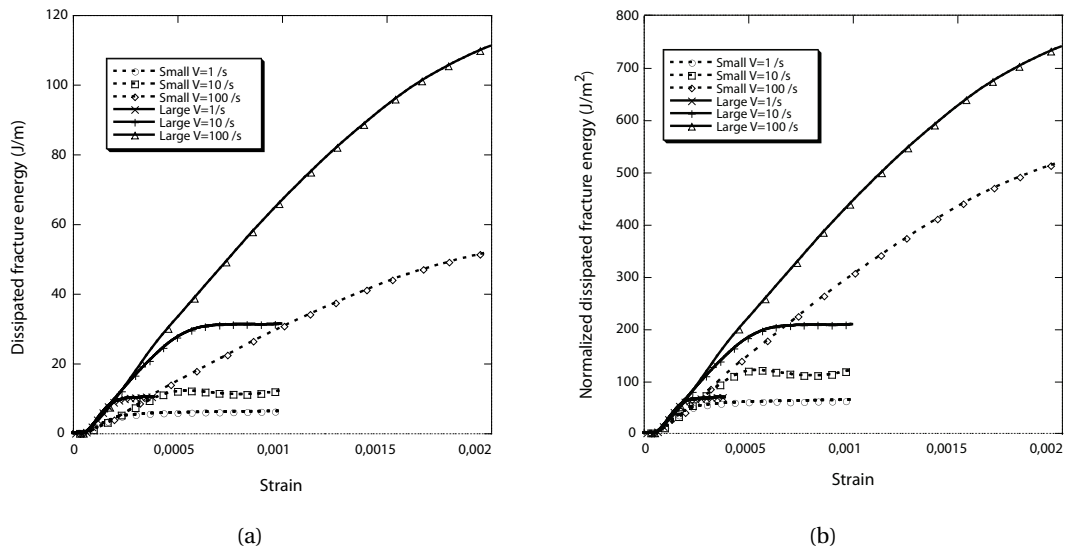


Figure 4.24: Influence of the specimen size on the dissipated fracture energy: (a) total energy and (b) normalized energy.

sample and equal to 10 for the larger one. We can conclude that in high loading rate regimes the numerical (and experimental) results are affected by this structural effect and it is not straightforward to properly quantify the true fracture energy values (the size of the sample is important).

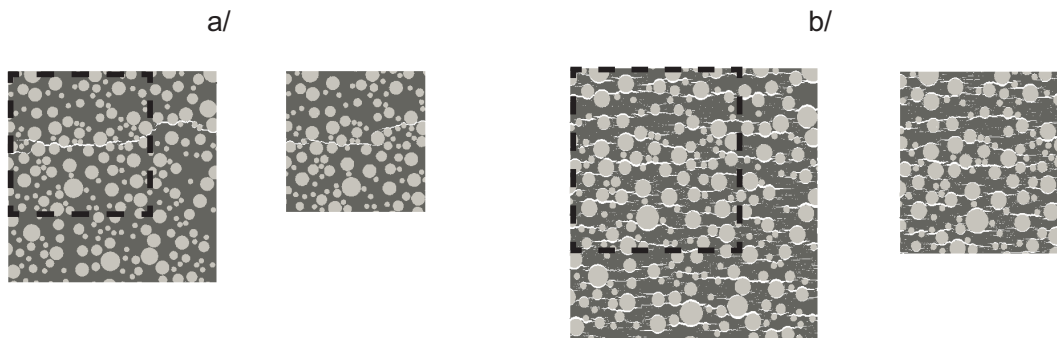


Figure 4.25: Influence of the specimen size on the fracture path: a/  $\dot{\epsilon} = 1 \text{ s}^{-1}$  b/  $\dot{\epsilon} = 100 \text{ s}^{-1}$ .

To choose the sample, we can notice that the size of the numerical "small" specimen is bigger than the experimental one (cylinder with a diameter of 74 mm [Weerheijm 07]) in which case a smaller DIF value should be obtained. We recall that the numerical DIF is 8 for the small sample whereas the experimental DIF is 12. As the aim of this work is not to study how we can reproduce the size effect with our model (even if the global trend seems to be good) we decided to keep the smaller size of the specimen.

### 4.5.3 Loading rate effect and dissipation

In this subsection we will investigate the strain rate dependence of the model. Similarly to the previous investigation only micro-inertia effects have been considered.

As already stated, experimental results on dynamic tension tests show a high rate sensitivity of tensile strength [Vegt 06, Erzar 10]. Figure 4.9b presents results obtained in literature. From this figure it is possible to distinguish between two different modes in the increase of strength. In the first mode –  $\dot{\epsilon} < 1 \text{ s}^{-1}$  – the dynamic resistance increase is probably due to the presence of water in the material. The free water in the micro-pores is assumed to exhibit the so-called Stefan-effect causing a strengthening effect in concrete with increasing rate of loading [Rossi 92]. This Stefan-effect is the phenomenon that occurs when a viscous liquid is trapped between two plates that are separated quickly, causing a reaction force on the plates that is proportional to the velocity of separation. In [Cadoni 01] a different explanation for the influence of the moisture content is given. Their interpretation is based on the principle of wave propagation in concrete. When a pore is not filled with water, it will locally reflect the incoming stress wave. The multiple reflections of all pores together can cause a considerable increase in stress. When a stress wave meets a pore that is filled with liquid the reflected stress is not big enough to cause the increase in stress that locally induces damage within the material. Therefore, the wet concrete will exhibit a more pronounced rate effect than the dry concrete. This interpretation only gives an explanation of the difference between wet and dry concrete and does not explain the increase in strength between static and dynamic loading. At a larger scale (constitutive level), Ozbolt *et al.* [Ozbolt 01] believe that the rate dependency consists of two parts: the first one related to the nucleation of micro-cracks, while the second one is due to the creep of concrete between the micro-cracks.

Figure 4.26 shows the numerical rate effect in tension obtained for the two different meso-structures considered here. One can see on this figure that the computed increase with strain rate is slight concerning the tensile strength. We obtain here a dynamic increase factor – equal to the ratio of the static versus the dynamic strengths – of 1.3 for  $\dot{\epsilon} = 100 \text{ s}^{-1}$  while it is equal to approximately 3 in the experiments. This result shows that the assumption of no rate effect in the cohesive traction law is not realistic. The micro-inertia effects in the fracture process zone are not sufficient to explain the rate dependency of concrete in tension even at the highest loading rate velocities. To get a better agreement one should introduce a rate dependency at the material level as already performed in the previous part.

Figure 4.27 depicts the evolution of the dissipated fracture energy as function of the macroscopic strain of the specimen for different loading rates and heterogeneities. One can see on this figure that, as already observed in Figure 4.26, the dissipated fracture energy strongly depends on the loading rate even with a rate independent local fracture energy (see Equation 3.37 and Figure 3.7). Here we obtain a ratio  $G_{f(dyn)}/G_{f(stat)}$  equal to approximately 8 – depending on the meso-structure – for  $\dot{\epsilon}=100 \text{ s}^{-1}$ . In the experimental data (see Table 4.4), with a Young modulus of the concrete approximately equal to 40 GPa we obtain a ratio of 12

#### 4.5. Additional analysis on rate dependency

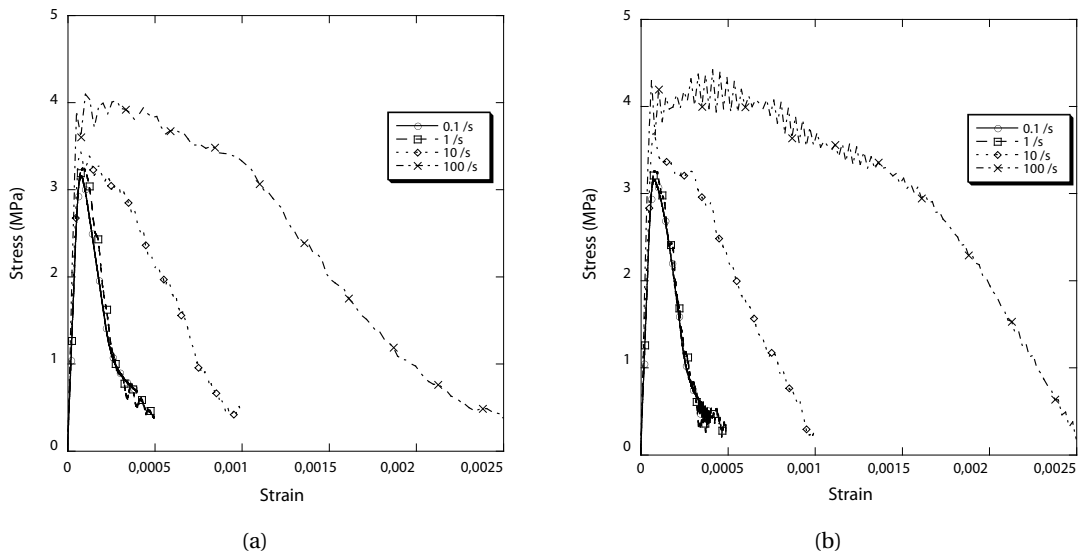


Figure 4.26: Rate effect in tension for the two meso-structures depicted in Figure 4.21: (a) Figure 4.21a and (b) Figure 4.21b.

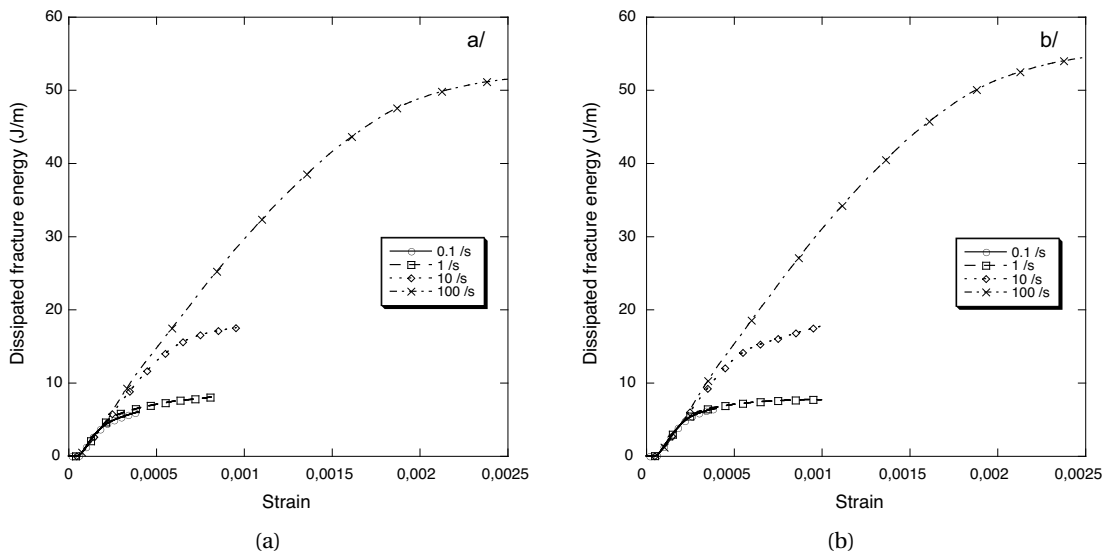


Figure 4.27: Influence of the meso-structure on the dissipated fracture energy for different strain rates for the two different meso-structures: (a) Figure 4.21a and (b) Figure 4.21b.

for  $\dot{\epsilon}=40 \text{ s}^{-1}$  (compared to quasi-statics). We note that even if the dynamic increase factor for the tensile strength is not large enough, it is less the case for the dissipated fracture energy. Moreover, and as expected, the dissipated fracture energy depends on the meso-structure (Figure 4.27a vs Figure 4.27b) due to the differences observed in Figure 4.26 on the post-peak curves.

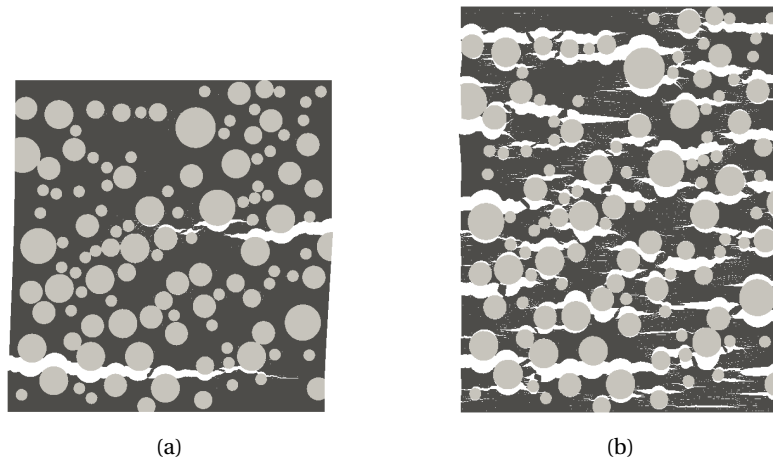


Figure 4.28: Influence of the loading rate on the final cracking for the meso-structure depicted in Figure 4.21a: (displacement has been magnified by a factor of 100): (a)  $\dot{\epsilon} = 0.1 \text{ s}^{-1}$ , (b)  $\dot{\epsilon} = 100 \text{ s}^{-1}$ .

As already observed in the first part of the chapter, simulation results seem to call for the introduction of a rate-dependent cohesive law. However, the introduced law should not increase too much the total dissipated fracture energy and the material ductility, but it should affect more the material strengthening. A possibility would be to adopt a similar law as the one proposed by Bažant and Li [Bažant 97]. Nevertheless, an additional question arises: should the rate-dependent function be applied only to a specific interface (most probably ITZ) or to all the parts of the meso-structure as done in Section 4.4? We believe that this point will be difficult to answer without some specific experiments on the different constituents of a real concrete.

## 4.6 Discussion

In this chapter we have investigated the influence of the aggregate's properties (*e.g.* referred to soft and hard aggregates, which differ in toughness and strength, but have a narrow range of elastic stiffness), the effect of the internal meso-structure (arrangement and shape of the aggregates) and the influence of their sizes. From the obtained results we can extract the following salient conclusions.

While the constitutive law used to model the interfacial behavior is insensitive to the loading rate, the model is able to capture the increase in peak strength and strain at failure with increasing rate of loading. The increase in strength with the strain rate resides in a more diffuse micro-cracking and is related to the intrinsic characteristic opening time of the cohesive law. However, the dissipated fracture energy at peak strength seems to be roughly independent of strain rate (although, post-peak dissipation of energy is clearly an increasing function of strain rate). Therefore, for our meso-mechanical approach, we cannot discard the combination of inertial with material rate hardening mechanisms. The introduction of a rate dependent cohesive law increases the difference of the computed peak strength between low and high strain rates, leading to a closer match with experiments.

In addition, simulations carried out for two different types of aggregates (soft and hard) concluded that the peak strength is considerably sensitive to the toughness of the inclusions, but only at low strain rates. There, the crack patterns for the two different aggregates are different. However, at high strain rates, micro-cracks nucleate in the matrix and have no time to propagate in the aggregates before peak strength is reached. This lead to a similar stress-strain behavior for the two aggregate types (inertial forces dominate the overall behavior in terms of strength).

The material parameters used in this study have been taken from the recent experimental literature [Rosselló 04, Rosselló 06] without modification. For instance one should notice that the stiffness of both types of inclusions is lower than the one of the matrix paste. Therefore, we have carried out a further investigation presented in the last section, where we have extended the range of stiffness (and strength) of the constituents in order to calibrate our model with other experimental data. The modifications include a higher value for the Young's modulus of the aggregates and a lower value for the strength of the interfaces between inclusions and matrix. Note that increasing the aggregates stiffness (and decreasing the interface strength) may also lead to a reduction of the (slight) mesh-dependency that the model exhibits at very high strain rates.

A comparison between three different meso-structures considered brings the following remarks. The specimen with uniform meso-structure reduces the maximum strength, because of the aligned aggregate's faces with the loading direction. Since this is avoided by rotating the aggregates, the rotated meso-structure shows always the higher peak strength. Finally, the random distribution increases the probability to have weak zones (interfaces between aggregates and matrix are closer), which reduces the peak strength.

In addition, our results show that, having two concrete materials with same aggregate volume ratio, the one with smaller inclusions will exhibit a larger strength at low strain rate in case of soft aggregates. Large aggregates facilitate the propagation of cracks within inclusions. This involves a larger area of broken aggregates, which is linked with a lower strength.

Additional investigation carried out with different material parameters and rate independent cohesive law to investigate if the experimentally observed dynamic increase factor is due to a

#### **Chapter 4. Influence of the meso-structure in dynamic tensile loading**

---

material effect or a structural (inertial) effect. With regards to tensile strength, the numerical results exhibit a small rate effect that is not coherent with the experiments. This confirms thus the need of the introduction of a rate dependent law to increase the strain-rate effect on the peak load. On the other hand, the computed dissipated energy show a closer match with experimental reported values. This means that the tensile strength increase is probably mostly due to a material effect (moisture, visco-elasticity, ...) while the dissipated fracture energy increase resides mainly in a finer networks of micro-cracks observed in the post-peak regime.



## 5 Mixed mode loading

In this chapter the model is extended to include a mixed-mode crack propagation capability. The content of this section reflects what was published in [Snozzi 12b]. In the following we describe the selected approach, which couples together cohesive zone modeling with a contact algorithm to enforce the impenetrability condition. We resort to the classical law of unilateral contact and Coulomb friction. While the debonding process is controlled by a new extrinsic traction separation law, which accounts for mode mixity, and yields two separate values for energy dissipation in mode I and mode II loading.

### 5.1 Introduction

As already mentioned, a careful treatment of both micro-cracking and frictional contact mechanisms is needed to achieve a fundamental understanding of the failure of brittle materials such as concrete. Indeed, fracture of such materials involves the opening of local micro-cracks, which may propagate, coalesce and subsequently enter into contact. The contacting rough surfaces play an important role in the amount of dissipated frictional energy, influencing the structural strength.

The transition from debonding to sliding frictional contact is an often overlooked (but key) dissipative mechanism in cohesive zone approaches. One of the first attempt combining both fracture and frictional contact phenomena has been introduced by Tvergaard [Tvergaard 90]. In this approach the response of the surface is assumed to be frictionless until complete debonding of the cohesive zone has occurred. Afterward, other authors considered the onset of friction to start in conjunction with the onset of fracture, for instance by coupling friction to decohesion, Chaboche *et al.* [Chaboche 97] and [Jean 01], or to adhesion, Raous *et al.* [Raous 97] and Del Piero and Raous [Del Piero 10]. More recent works on this topic include those on fiber pullout/push-out (*e.g.* Dollar *et al.* [Dollar 93], Chandra and Ananth [Chandra 95], Lin *et al.* [Lin 01], Talon and Curnier [Talon 03] and [Tsai 05]) and applications to structural engineering (*e.g.* plane and reinforced concrete by Cervenka *et al.* [Cervenka 98], Raous et Karray [Raous 09], masonry walls by Alfano and Sacco [Alfano 06], Sacco and Toti [Sacco 10], Fouchal *et al.* [Fouchal 09] and Koutromanos and Shing [Koutro-

manos 12]) and to brittle materials (Acary and Monerie [Acary 06]).

In this chapter the adopted approach coupling cohesive zone modeling, to represent damage, and a contact algorithm, for enforcing the impenetrability condition is presented. The key features of the model are:

- A novel initially rigid extrinsic TSL law, which enables us to define two separate values for the dissipated fracture energy in mode I and II. This formulation extends the work of Von den Bosch *et al.* [Von den Bosch 05], which developed such a model for TSL with an initial elasticity (intrinsic approach), such intrinsic cohesive laws are known to alter the elastic properties of the specimen [Klein 01].
- A continuous transition from decohesion to the pure frictional state. Friction and fracture occur simultaneously when a crack is forming under compression, avoiding numerical instabilities due to a possible stress jump when transitioning from complete debonding to pure frictional sliding.

Section 5.2 describes the developed mixed-mode cohesive approach, and applies the proposed TSL to a benchmark [Von den Bosch 05]. In Section 5.3 the adopted frictional contact enforcement algorithm is reported. The model has been successfully implemented in a finite-element program and validated by experimental data at the material level and the structural level.

Section 5.4 validates the model by comparing the numerical results to experimental data at the meso-level and structural level. The first application consists of a shear test experiment on masonry wallettes (a conventional test in order to determine the shear resistance of joints between bricks), while the second application simulates a masonry wall loaded in compression and shear.

### 5.2 Modified cohesive law for mixed mode loading

Since the Camacho-Ortiz TSL is based on a potential, it is clear that the dissipated fracture energy for a growing crack does not depend on the opening path. However, as reported in [Von den Bosch 05], it can be argued that the dissipated fracture energy should be path dependent, due to micro-structural details such as interface roughness which cannot be depicted without an extremely fine discretization.

Hence the TSL should allow for independent values of the dissipated energy depending on the loading path as depicted in Figure 5.1. We propose an alternative cohesive law based on the classical model of Camacho and Ortiz by relaxing the hypothesis of a well-defined energy potential (as previously done in [Von den Bosch 05] but for the intrinsic cohesive model of Xu and Needleman [Xu 93]). We have preferred this option to a pseudo-potential formulation (for instance proposed in [Park 09]) because of its ease of formulation. This results in a law which is not anymore bounded by a free potential energy (*i.e.* only the tractions are defined).

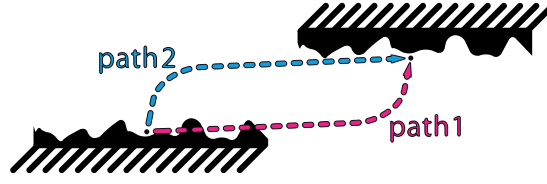


Figure 5.1: Cohesive zone loaded with two different paths leading potentially to two distinct values of dissipated energy.

A new independent parameter  $\kappa$ , which enables us to define the ratio between  $G_{c,I}$  and  $G_{c,II}$ , is introduced.

$$\kappa = \frac{G_{c,II}}{G_{c,I}} \quad (5.1)$$

We set the work of separation for a cohesive zone opened completely under Mode I ( $G_{c,I}$ ) to correspond to the one computed with the Camacho-Ortiz model ( $G_c$ ). Therefore the cohesive normal traction envelop has in this case an identical shape as in the Camacho-Ortiz TSL. Conversely, because the introduced parameter,  $\kappa$ , is linked with the tangential direction, the adjustment influences the shapes of the tractions, when the opening does not occur in pure normal direction. Our model yields the following equation for the cohesive tractions in case of crack opening:

$$\mathbf{T} = \left( \frac{\beta^2}{\kappa} \Delta_t \mathbf{t} + \Delta_n \mathbf{n} \right) \frac{\sigma_c}{\delta} \left( 1 - \frac{\delta}{\delta_c} \right) \quad (5.2)$$

The effective opening displacement, previously defined in equation 3.32, needs to be redefined as follows:

$$\delta = \sqrt{\frac{\beta^2}{\kappa^2} \Delta_t^2 + \Delta_n^2} \quad (5.3)$$

Normal and tangential tractions are shown in Figure 5.2 as function of the normalized normal and tangential opening displacements. As postulated in [Camacho 96] damage is considered to be an irreversible process. Unloading or reloading takes place when  $\delta < \delta_{max}$ . In this case the tractions are calculated with:

$$T_n = \Delta_n \frac{\sigma_c}{\delta_{max}} \left( 1 - \frac{\delta_{max}}{\delta_c} \right) \quad (5.4)$$

$$T_t = \frac{\beta^2}{\kappa} \Delta_t \frac{\sigma_c}{\delta_{max}} \left( 1 - \frac{\delta_{max}}{\delta_c} \right) \quad (5.5)$$

With these equations the tractions are linearly interpolated between the origin and the tractions at which the opening will be equal to the maximal attained effective opening displace-

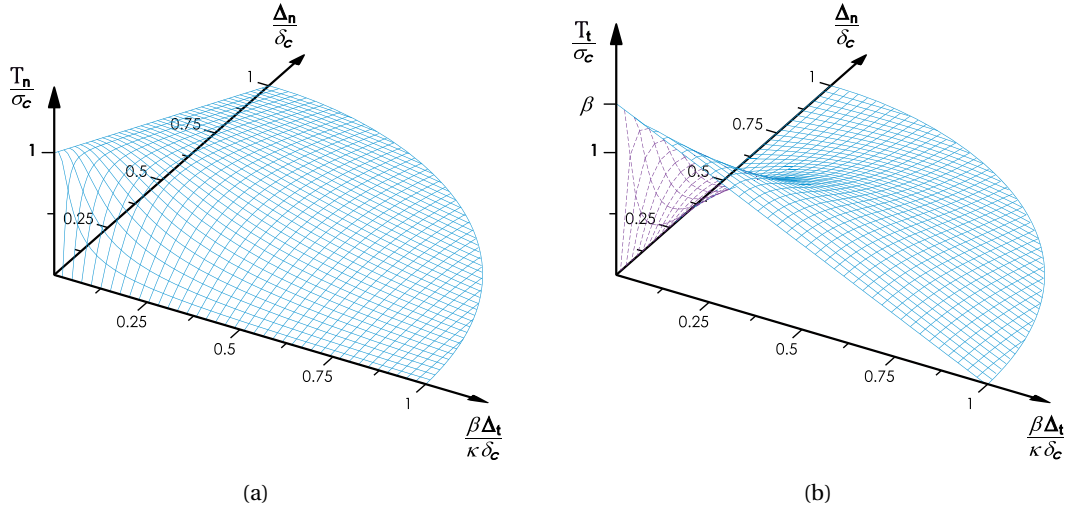


Figure 5.2: Cohesive traction in (a) normal direction and (b) tangential direction (with  $\beta > 1$ ).

ment in the new loading direction.

### 5.2.1 Work of separation under combined normal shear loading

If  $\kappa$  is set equal to one, the tractions and the dissipated energy match with those of the Camacho-Ortiz TSL. Whereas, if  $\kappa$  is set different to one, the dissipated fracture energy becomes path dependent and therefore does not correspond for every loading path to the mode-independent fracture toughness  $G_c$ . This energy can be computed by integrating the tractions over the path. In order to depict the mode dependent behavior of the proposed TSL and to verify our model we repeat the two different patch tests reported in [Von den Bosch 05]. In this work it was demonstrated that the classical Xu Needleman law failed these patch tests, showing some unphysical/unexpected behavior in the computed amount of separation work. The first one consists in loading a surface monotonically with an imposed constant loading angle until complete separations occurs, Figure 5.3a (*i.e.* proportionality between tangential and normal displacements). Whereas, in the second case, the cohesive zone is loaded first in one direction up to a maximal value, and then broken completely in the other direction (non proportional loading).

For a separation associated with a loading angle  $\alpha$ , the work of separation can be expressed as

$$W_{tot} = \int_0^{\Delta_{n,c}} T_n(\Delta) d\Delta_n + \int_0^{\Delta_{t,c}} T_t(\Delta) d\Delta_t \quad (5.6)$$

The evolution of  $W_{tot}$  in respect to the loading angle is depicted in Figure 5.3b. The graph has been normalized by  $G_{c,I}$ . Since we have chosen a higher value of the fracture energy in mode II, the dissipated fracture energy increases monotonically by a factor of  $\kappa$  between the

## 5.2. Modified cohesive law for mixed mode loading

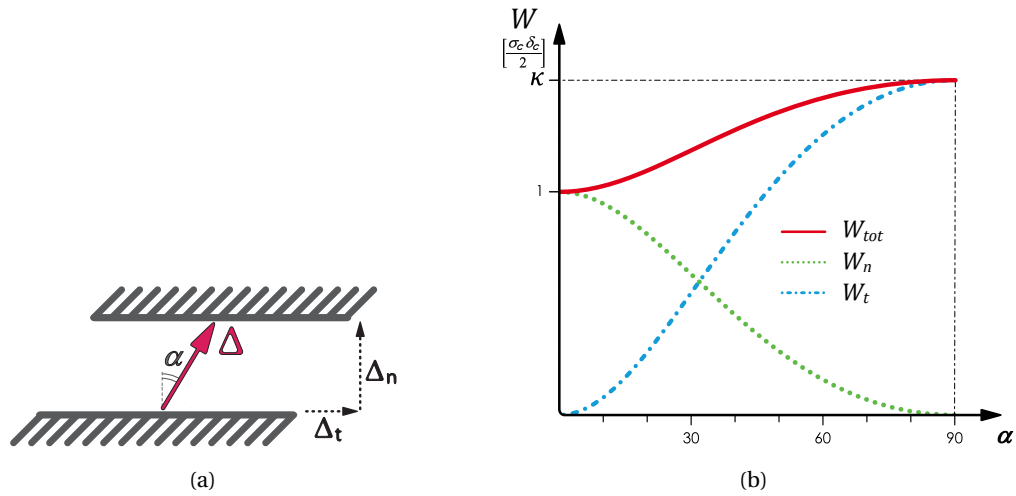


Figure 5.3: (a) Cohesive zone loaded under a constant angle  $\alpha$  as in [Von den Bosch 05] and (b) resulting dissipated work as function of the loading angle expressed in units of  $G_{c,I}$  (with  $\kappa > 1$ ).

two extremes 0 and 90, which corresponds to the fracture energy for mode I and mode II respectively. Indeed, increasing the angle is equivalent to increasing the work done by the tangential traction ( $W_t$ ) and decreasing the portion corresponding to the normal traction ( $W_n$ ).

For the non proportional loading, the surface is opened in the first case up to a maximal



Figure 5.4: Interface non proportionally loaded: (a) first in normal direction until  $\Delta_{n,max}$  and then broken in shear and (b) first in tangential direction until  $\Delta_{t,max}$  and then broken in normal direction as in [Von den Bosch 05].

normal displacement  $\Delta_{n,max}$  and then broken completely in shear (Figure 5.4a). Conversely, in the second case the zone is loaded first in tangential direction (up to the value  $\Delta_{t,max}$ ) and then separated in normal direction until complete separation occurs (Figure 5.4b).

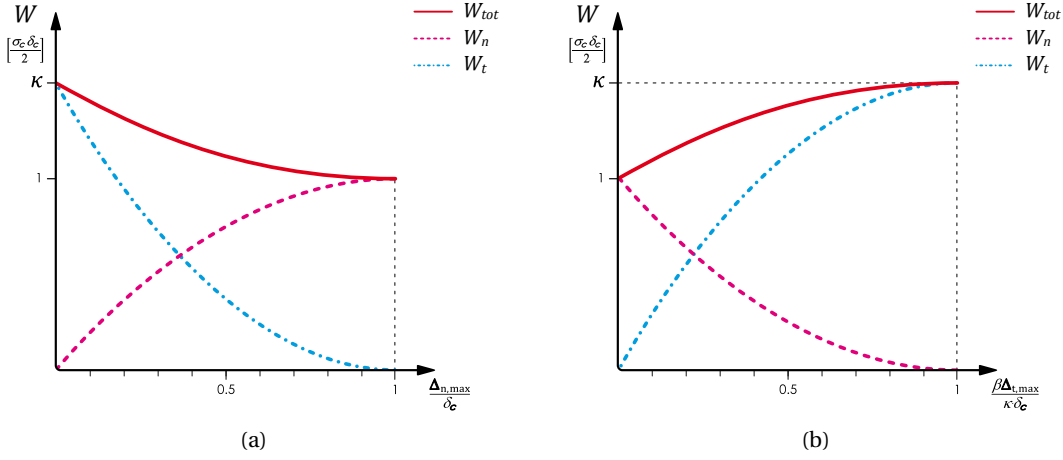


Figure 5.5: (a) Work of separation when loading first in (a) normal direction and (b) in tangential direction respectively expressed in units of  $G_{c,I}$  (with  $\kappa > 1$ ).

The dissipated fracture energy for case one and two can be expressed with

$$W_{tot} = \int_0^{\Delta_{n,max}} T_n(\Delta_n, \Delta_t = 0) d\Delta_n + \int_0^{\Delta_{c,t}} T_t(\Delta_n = \Delta_{n,max}, \Delta_t) d\Delta_t \quad (5.7)$$

$$W_{tot} = \int_0^{\Delta_{t,max}} T_t(\Delta_n = 0, \Delta_t) d\Delta_t + \int_0^{\Delta_{c,n}} T_n(\Delta_n, \Delta_t = \Delta_{t,max}) d\Delta_t \quad (5.8)$$

The results of the first case are reported in Figure 5.5a.  $W_{tot}$  is equal to  $G_{c,I}$  if  $\Delta_{n,max}$  is set equal to  $\delta_c$  and corresponds to  $G_{c,II}$  if  $\Delta_{n,max}$  is equal to zero. An analogous behavior can be observed in the second case, Figure 5.5b. In both loading cases it is possible to recognize that the transition of the dissipated fracture energy as function of the maximal first opening is smooth and does not show any kink or unphysical oscillation.

### 5.3 Contact enforcement

When a crack is growing under compressive shear loading, we enforce the impenetrability condition by a master-slave explicit contact algorithm. Since our goal is to be able to deal with multiple cracking, which causes numerous asperities to enter into contact, we have preferred an explicit contact enforcement rather than a more traditional static or implicit dynamic formulation. Among this second class of methods, augmented Lagrangian multipliers (for instance [Alart 91]) and penalty methods (for instance [Kikuchi 88]) have been widely used. The first class is able to provide an accurate constrain enforcement circumventing ill-conditioning. Nevertheless, the size of the problems might be limited due to the implicit system of equations that one needs to solve, which can rapidly increase the computational cost

with increasing system size. On the other hand, penalty methods allow a little interpenetration of the contacting surfaces, which is inversely proportional to the value of the penalty parameters. Nevertheless, a high value of these parameters can produce an ill-conditioned system of equations, requiring a high number of iterations and leading to convergence problems. Moreover, another drawback, in the explicit dynamic version of this method, is that the critical time step decreases with increasing stiffness penalty parameter.

Thereby, in this work we have decided to address the above-mentioned difficulties enforcing the impenetrability constrain using a ballistic method called Decomposition Contact Response (DCR) developed by Cirak and West [Cirak 05]. This method is based on the conservation of linear and angular momentum while the impenetrability condition is guaranteed by acting on the displacements directly, *e.g.* by projecting the impacting nodes on the penetrated surface. Therefore, the purpose of the method is not to resolve the impact time exactly for every node

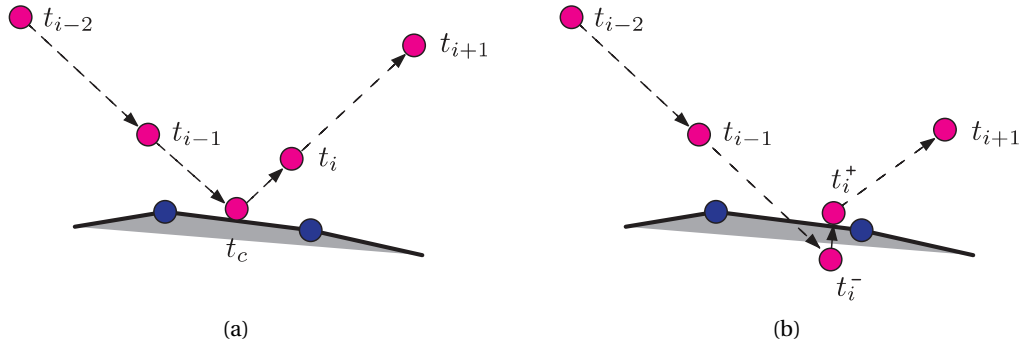


Figure 5.6: (a) Impact-time resolved exactly and (b) approximation of the DCR.

as depicted in figure 5.6a, but with an approximation as illustrated in figure 5.6b. Thus, nodes which are allowed to penetrate the master surface within the predictor ( $t_i^-$ ), must subsequently be projected back within the same time step ( $t_i^+$ ). The equations governing the impact (beside the projection of the slave nodes on the master surfaces) are

$$\mathbf{p}^{t_i^+} - \mathbf{p}^{t_i^-} = \lambda \nabla_{\mathbf{x}} g(\mathbf{x}^{t_i^+}) \quad (5.9)$$

$$[\mathbf{p}^T \mathbf{M}^{-1} \mathbf{p}]_{t_i^-}^{t_i^+} = 0 \quad (5.10)$$

where  $\mathbf{p} = \mathbf{M}\dot{\mathbf{x}}$  represents the momentum vector of slave and master nodes (with  $\mathbf{M}$  mass matrix, which has the size 6x6 for edge to node contact),  $g$  is the gap function and  $\lambda$  a scalar parameter. The approach modifies only the post impact velocities of the contacting nodes involved in contact but only for their components in direction of the gap gradient. A closed form for the post impact velocities can be derived using momentum decomposition. We will report here the main equations for computing the momentum after collision (for a detailed derivation see reference [Cirak 05]). First, velocities of all impacting nodes need to be decomposed into their

normal (subscript  $n$ ) and tangential (subscript  $t$ ) components giving

$$\dot{\mathbf{x}} = \dot{\mathbf{x}}_n + \dot{\mathbf{x}}_t \quad (5.11)$$

where the normal  $\dot{\mathbf{x}}_n$  components are defined as

$$\dot{\mathbf{x}}_n = \left( \frac{(\nabla g)^T \dot{\mathbf{x}}}{(\nabla g)^T \mathbf{M}^{-1} \nabla g} \right) \mathbf{M}^{-1} \nabla g \quad (5.12)$$

With the above equation, one can compute the normal components of the velocity before impact of the contacting triplets (node to segment approach). The normal components of the velocity after impact can be thus corrected as follow

$$\dot{\mathbf{x}}_n^+ = \dot{\mathbf{x}}_n^- - \dot{\mathbf{x}}_n^- (1 + c_{res}) \quad (5.13)$$

where  $c_{res}$  represents the coefficient of restitution, which can range between 0 (completely inelastic contact) and 1 (perfectly elastic contact) and the superscripts  $^+$  and  $^-$  denote quantities before and after projection respectively (in the application presented in this chapter, we choose  $c_{res} = 0$ ).

### 5.3.1 Frictional impact

A simple Coulomb friction law can be included by computing the relative motion between the contacting entities. To this end the velocity needs to be decomposed into fixed and non-fixed components

$$\dot{\mathbf{x}} = \dot{\mathbf{x}}_{nonfix} + \dot{\mathbf{x}}_{fix} \quad (5.14)$$

where only the non-fixed components  $\dot{\mathbf{x}}_{nonfix}$  lead to a relative motion between the bodies. In order to derive the non-fixed components of the velocity a separation vector between two impacting points needs to be defined

$$\mathbf{h} = \mathbf{x}^L - \mathbf{x}^R \quad (5.15)$$

where  $\mathbf{x}^L$  and  $\mathbf{x}^R$  stand for the positions of the two impacting points. Consequently the non-fixed components can be obtained as follow

$$\dot{\mathbf{x}}_{nonfix} = \mathbf{M}^{-1} (\nabla \mathbf{h})^T \left( \frac{(\nabla \mathbf{h}) \dot{\mathbf{x}}}{(\nabla \mathbf{h}) \mathbf{M}^{-1} (\nabla \mathbf{h})^T} \right) \quad (5.16)$$

Since the non-fixed velocity is the resultant between motion leading to interpenetration ( $\dot{\mathbf{x}}_n$ ) and relative tangential displacement (sliding), the slide components are given by

$$\dot{\mathbf{x}}_{slide} = \dot{\mathbf{x}}_{nonfix} - \dot{\mathbf{x}}_n \quad (5.17)$$



According to the Coulomb model one can compute the slip velocity as follow

$$\mu \frac{\|\dot{\mathbf{x}}_n^T \mathbf{M}^{-1} \dot{\mathbf{x}}_n\|}{\|\dot{\mathbf{x}}_{slide}^T \mathbf{M}^{-1} \dot{\mathbf{x}}_{slide}\|} \dot{\mathbf{x}}_{slide} \quad (5.18)$$

In order to account for stick-slip, the authors [Cirak 05] suggest to bound the maximal frictional impulse which can be delivered during sliding with the minimum value between equations 5.17 and 5.18 (the stick and slip velocity respectively)

$$\dot{\mathbf{x}}_t^+ = \dot{\mathbf{x}}_t^- - \min \left( 1, \mu \frac{\|\dot{\mathbf{x}}_n^T \mathbf{M}^{-1} \dot{\mathbf{x}}_n\|}{\|\dot{\mathbf{x}}_{slide}^T \mathbf{M}^{-1} \dot{\mathbf{x}}_{slide}\|} \right) \dot{\mathbf{x}}_{slide} \quad (5.19)$$

If the relative motion between two contacting bodies becomes too small, equation 5.19 will cause most of the nodes to get into stick, leading consequently to an insufficient frictional force between the sliding bodies. Therefore, the limitation criterion of equation 5.19 has been removed, allowing bigger correction in the tangential quantity of motion within the predictor. Nevertheless, this can produce too large values in the delivered frictional impulse. Thus, the relative motion between the sliding nodes needs to be verified after Newmark's corrector and if necessary corrected.

### 5.3.2 Coupling with cohesive zone model

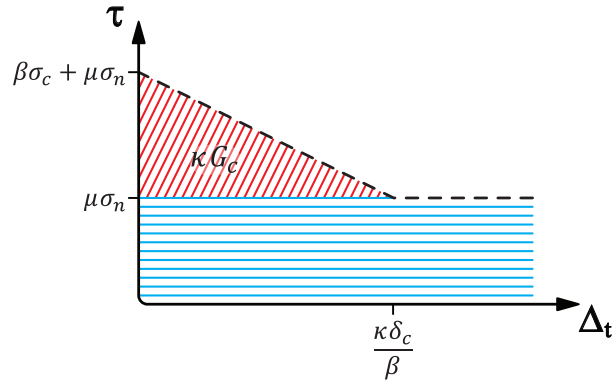


Figure 5.7: Shear stress-tangential opening displacement relationship for a growing crack in mode II with full onset of friction.

As already mentioned before, the contact algorithm is coupled in parallel with the TSL. This implies that friction and fracture occur simultaneously in the cohesive zone when a crack is growing under compression. A first possibility, as illustrated in Figure 5.7, is to assume a full onset of friction at the beginning of decohesion. This superimposition combined with the extrinsic approach gives a very steep (rigid) initial behavior followed by the softening branch. Therefore, in order to reproduce the experimental interfacial behavior, a different transition

from the onset of fracture to pure frictional sliding has been chosen (note that the accuracy of the transition might depend on the level of observation and material). Our second approach

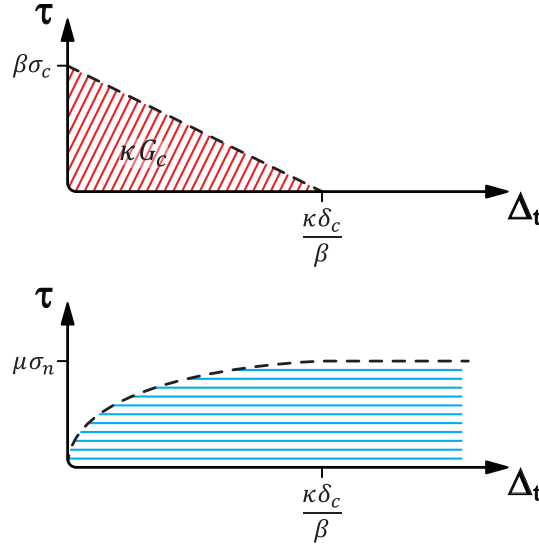


Figure 5.8: Adopted shear stress-tangential opening displacement relationship for a growing crack in mode II with increasing frictional capability.

(depicted in Figure 5.8) considers a progressive shift to friction during debonding. When the cohesive zone starts to damage, friction does not act on the interface, but it rises gradually with increasing decohesion, giving a soft transition from debonding to the pure frictional stage. The function that regulates the increase in the friction force depends on the amount of damage experienced by the cohesive zone and is given by:

$$1 - \left(1 - \frac{\delta}{\delta_c}\right)^q \quad (5.20)$$

where the exponent  $q$  has been set in this work to three. Note that the chosen cubic transition function implies a relatively high dissipation of frictional energy already during the decohesion process (and that the peak shear strength/traction remains essentially influenced by both the cohesive strength and the amount of applied compressive force). To summarize, as depicted in Figure 5.8 for a growing crack in Mode II the cohesive elements are inserted if the tangential stresses exceed  $\beta\sigma_c$ . A fracture energy corresponding to  $\kappa G_c$  multiplied by the length of the cohesive zone will have been dissipated when the tangential opening ( $\Delta_t$ ) attains the critical opening value ( $\kappa\delta_c/\beta$ ). During this process, the cohesive zone experiences a continuous transition from debonding to pure frictional sliding.

## 5.4 Numerical validation

As mentioned in the introduction, in order to validate our numerical model, we have selected two problems related to the masonry engineering field. The first application is a simple and representative experiment of a masonry wallette, which has been used to identify the interface's parameters. These parameters have then been used to predict the behavior of a masonry wall loaded in compression and shear.

### 5.4.1 Application to a masonry wallette

Masonry is one of the most widely used construction material in civil engineering around the world. Therefore, different tests have been designed in order to extract the properties of its components. Among these, a common experiment in order to determine the ultimate shear strength of the mortar joints, is a shear test of a masonry wallette, which consists of three bricks linked with two mortar joints (shear triplet) as depicted in Figure 5.9a. For our work we refer to the experimental data obtained by Beyer *et al.* ([Beyer 10] and [Beyer 11]).

Experimentally, the masonry wallettes have been tested on a loading machine. During the experiment the inner brick is supported at the upper edge with two rigid blocks, while the shear load is introduced on the lower edge of the two outer bricks. Horizontal rods are responsible for the horizontal axial force, which guarantees constant normal stress acting on the mortar joints during the shearing.

The virtual experimental setup chosen for the numerical test consists in half of the symmetric

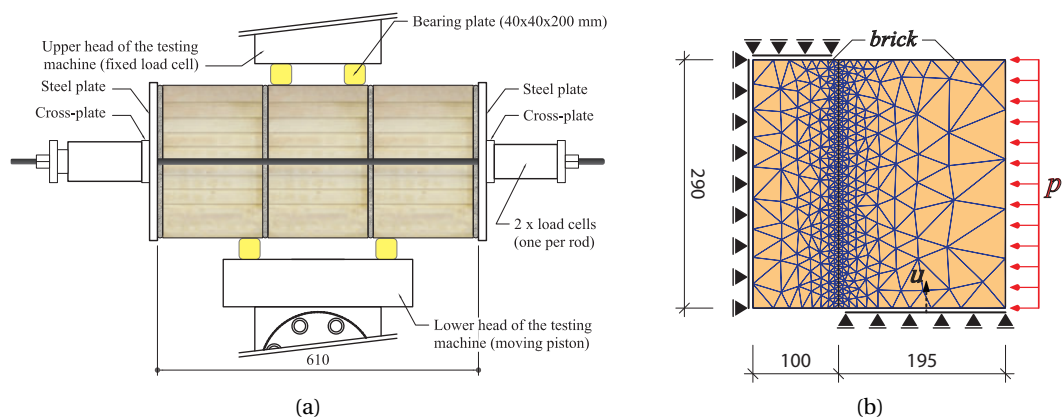


Figure 5.9: (a) Experimental test setup of the wallette [courtesy of Beyer [Beyer 10], [Beyer 11]] and (b) corresponding finite-element mesh, corresponding to one half of the experimental setup (all dimensions in mm).

part of the experimental setup and is drawn in Figure 5.9b with the adopted finite-element mesh. The mesh has been chosen fine enough in order to achieve numerical convergence leading to an element size of about 5 mm (element edge) at the inter-brick boundary. The boundary conditions for the upper and lower edge have been simplified by extending the

length for load introduction and support to the edge length. It should be pointed out, that this change in the boundary condition has not a significant influence on the global behavior of the wallette (in terms of shear stress-displacement relationship). The two bricks have been modeled explicitly, whereas the mortar layer and the two interfaces between mortar and bricks are represented by means of a line of dynamically inserted elements with the proposed cohesive frictional capability.

Elastic constitutive behavior is assumed for the brick's elements. The elastic material parame-

Table 5.1: Material properties of the masonry bricks.

<i>Material</i>	E [Gpa]	$\nu$ [-]	$\rho$ [Kg/m <sup>3</sup> ]
Brick	14.0	0.15	940

ters are reported in Table 5.1 (and have been taken from [Beyer 10] for the density and Young's modulus and from [Alfano 06] for the Poisson ratio). Whereas, the cohesive parameters (see Table 5.2) for the interfacial transition zone between bricks have been fitted, in order to achieve a good agreement between the numerical and experimental shear-displacement relationship. The value for the critical stress is of the same order as the values for the strength of the joints reported in [Van der Pluijm 92] and [Lourenço 97]. Whereas, the values for the fracture energies are somewhat higher than the values suggested in these two references but on the same order of magnitude as the ones given in [Pina-Henriques 06]. Moreover,  $\kappa$  has been set in order to represent the usual ratio between the fracture energies in mode II and I in masonry engineering. The fitting has been achieved by varying the value of the cohesive strength and dissipated fracture energy. As depicted in Figure 5.10a larger values of  $\sigma_c$  increase the peak shear resistance, whereas larger value of  $G_{c,I}$ , Figure 5.10b, shift the transition to the pure frictional state toward higher values of the brick displacement. One can notice from Table 5.2

Table 5.2: Cohesive properties for interface elements, in bold assumed values for the shear test.

<i>Interface</i>	$\sigma_{c,I}$ [MPa]	$G_{c,I}$ [J/m <sup>2</sup> ]	$\sigma_{c,II}$ [MPa]	$G_{c,II}$ [J/m <sup>2</sup> ]	$\mu$
Brick-mortar	0.2 <b>0.3</b> 0.4	75 <b>125</b> 200	$\sigma_{c,I}$	$6 \cdot G_{c,I}$	0.77

that only cohesive values for the interface between mortar and brick are given. Indeed, as reported above, the propagation of cracks can occur only at the inter-element boundaries between brick and mortar, while bricks are assumed to remain uncracked. Indeed, we have not adopted a fully meso-scale representation of masonry (as for instance in [Pina-Henriques 06]) and all the cracking is concentrated at the straight interfaces.

In order to have a smoother transition from uncracked to cracked regime, variations in the value of the critical stresses following a normal distribution (with standard deviation in the order of 0.05 MPa) have been adopted. Moreover, in order to reduce oscillation during sliding and to reduce the amount of energy injected in the system (which is due to the projection

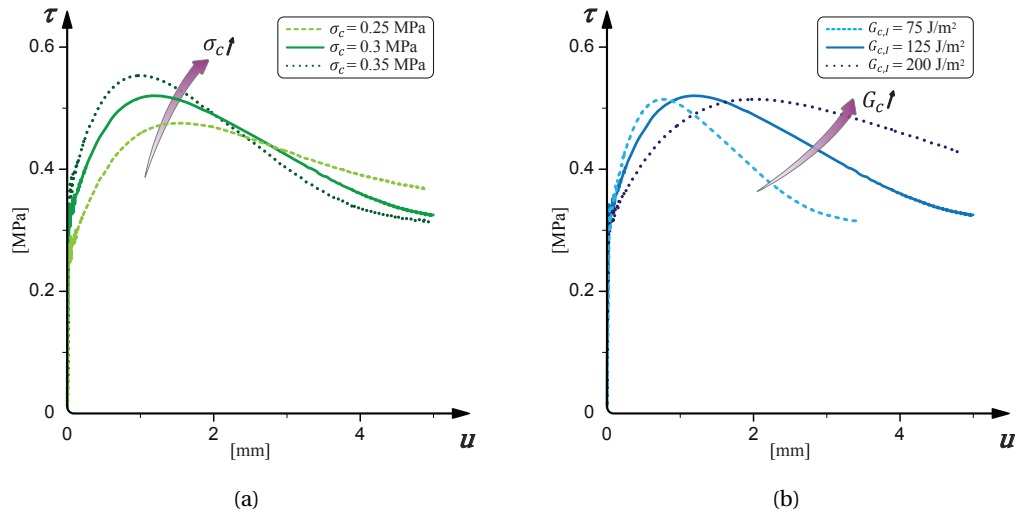


Figure 5.10: Shear stress plotted against shear displacement: (a) for different values of  $\sigma_c$  ( $G_{c,I}$  kept constant) and (b) for different values of  $G_{c,I}$  ( $\sigma_c$  kept constant).

of the slave nodes) material damping has been adopted. Figure 5.11 shows the influence of damping on the computed stress-displacement relationship and on the amount of kinetic energy in the specimen for two different Rayleigh damping ratio  $\zeta$  [Bathe 96]. As illustrated in Figure 5.11b, the regularization through damping allows to maintain the right level of kinetic energy (insufficient damping leads to an increase of energy in the system and to oscillations in the stress displacement curve). For this application a damping ratio of 7 % has been used. As in the testing machine, the specimen has been loaded with an imposed displacement with a constant normal pressure level of 0.4 MPa. The outer brick has been displaced at a constant initial velocity ( $v$ ) of 0.025 m/s in order to avoid rate-effects (similar to [Bi 02]). Nevertheless, loading velocities beyond 0.05 m/s increase the peak shear stress. Similarly to the experiments, the shearing has been interrupted after a path of approximately 10 mm.

The comparison of the shear stress-displacement relationship between experiment and simulation is illustrated in Figure 5.12. The stress (y-axis) in the figure is obtained by dividing the shear force acting on the brick by the area of the interface between mortar and brick. In general, the experimental and numerical curves are in good agreement. The transition to the pure frictional regime is smooth and the model is able to depict friction correctly. This demonstrates the robustness of our frictional cohesive model. The curved shape of the numerical shear-displacement relationship at initial stage of loading can be traced back to the assumed transient coupling between decohesion and friction.

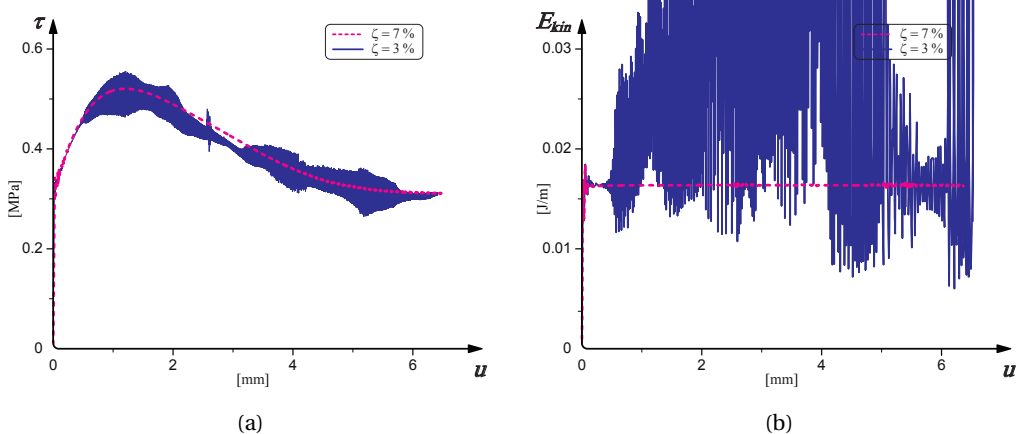


Figure 5.11: Regularization of damping on (a) the stress-displacement curve and (b) the amount of kinetic energy in the system.

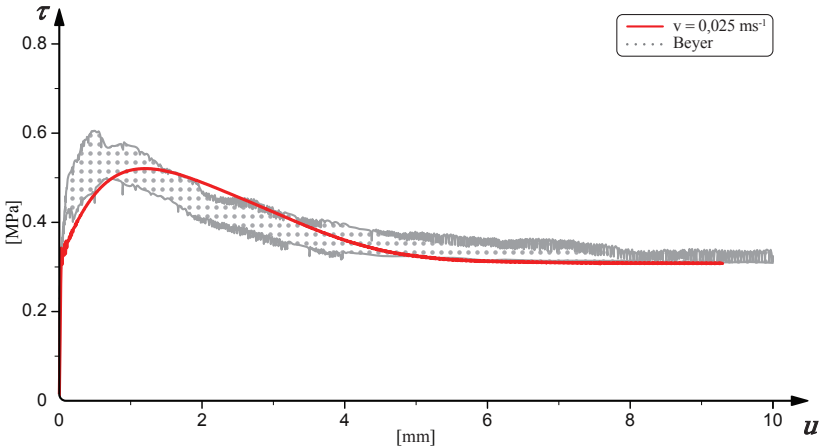


Figure 5.12: Shear stress plotted against shear displacement: comparison between experimental envelope (dotted gray area) and simulation (continuous red line).

### 5.4.2 Application to a masonry wall

The second selected application for the interface model is the simulation of a masonry wall loaded in shear and compression under low and moderate strain rate. For this virtual experiment we have chosen to reproduce one test unit of the experimental test program conducted by Ganz and Thürlimann [Ganz 84]. The geometry of the wall is represented in Figure 5.13. The

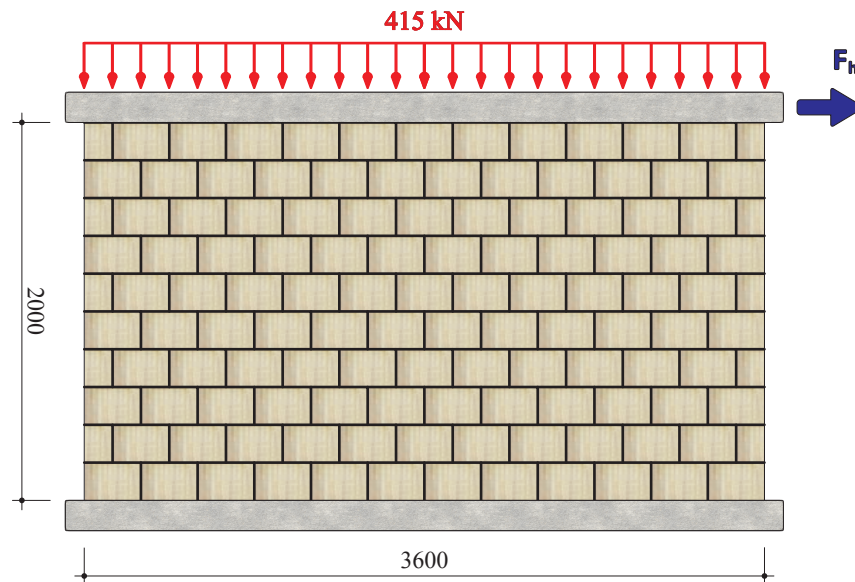


Figure 5.13: Experimental setup of the masonry wall tested in [Ganz 84] (all dimensions in mm).

specimen is 3.6 m wide and 2 m high (which represents approximately 80 % of a full-scale wall in a building). Experimentally, each test unit has been loaded first with a normal compressive force (kept constant during the shearing) and then displaced horizontally under a quasi-static regime. The bricks that compose the wall are hollow clay bricks 29 cm long, 19 cm high and 15 cm thick, and thus similar to the bricks of the previous application. Since no experimental data of the interface properties was available, we have used the parameters calibrated for the first application.

The mesh adopted for the virtual experimental setup is illustrated in Figure 5.14. The bricks have been modeled explicitly, whereas the interfacial transition zone is represented (as before) by dynamically inserted elements with the proposed cohesive frictional capability. Since cohesive insertion is allowed only at the interfaces between bricks, bricks are assumed to remain uncracked (this assumption can be considered adequate for low to moderate values of the horizontal wall's displacement, because little crushing of the bricks is observed experimentally). The bricks are modeled with elastic elements and their material properties are the same as those reported in Table 5.1 except for the density which has been set to  $855 \text{ Kg/m}^3$ . The cohesive parameters of the interfaces are reported in Table 5.2.

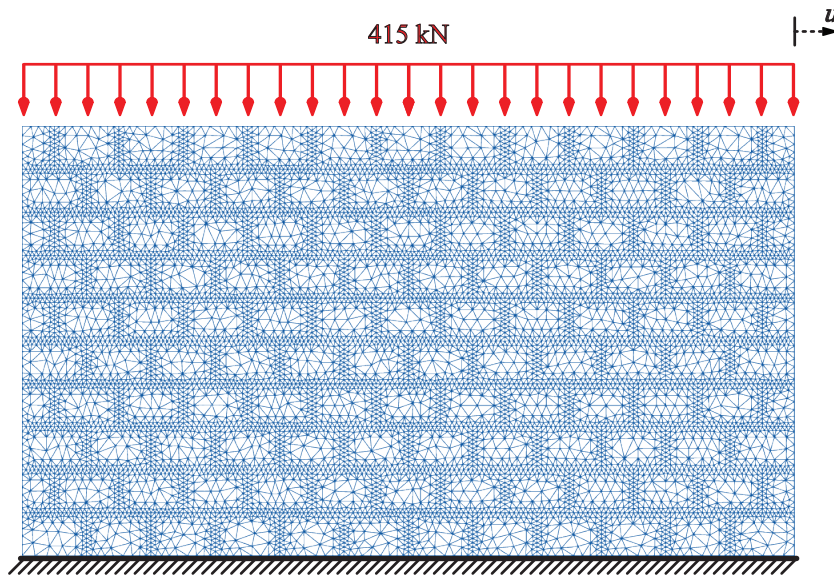


Figure 5.14: Adopted finite-element mesh.

The specimen has been loaded first with a vertical force of 415 kN. Little fluctuations in the amount of vertical displacement of the nodes located on the top edge have been allowed in order to maintain a constant level of compression during the shearing test. The shearing has been applied to the top edge of the wall prescribing a displacement  $u$ . The test has been performed at two loading velocities ( $v$ ): a low one ( $0.05 \frac{\text{m}}{\text{s}}$ ), which can be considered representative of a quasi-static regime, and a moderate one ( $0.5 \frac{\text{m}}{\text{s}}$ ) in order to show the rate dependent response of the tested unit. The damping ratio has been set to 0.75 %. The numerically computed and the experimentally recorded force displacement curves are compared in Figure 5.15. One can remark that the model can successfully reproduce the experimental behavior. Although the initial response of the wall is stiffer than the experimental one (probably because of the virtual setup and the assumed interface parameters), the peak strength and the corresponding displacement at peak strength almost match the values reported by Ganz. As depicted in the figure the response of the wall depends on the amount of horizontal velocity. An increasing velocity causes a delay in the dissipation of cohesive energy and a more diffuse cracking network that produces an overall increase in strength. The crack pattern for the two different loading velocities is depicted in Figure 5.16. One can notice that the higher applied velocity causes a higher number of cracks perpendicular to the loading direction. The bigger amount of cracks is related to the intrinsic opening time of the cohesive zone and is responsible for the increase in strength, which is obtained despite the rate insensitive constitutive law used to model the interfacial behavior.



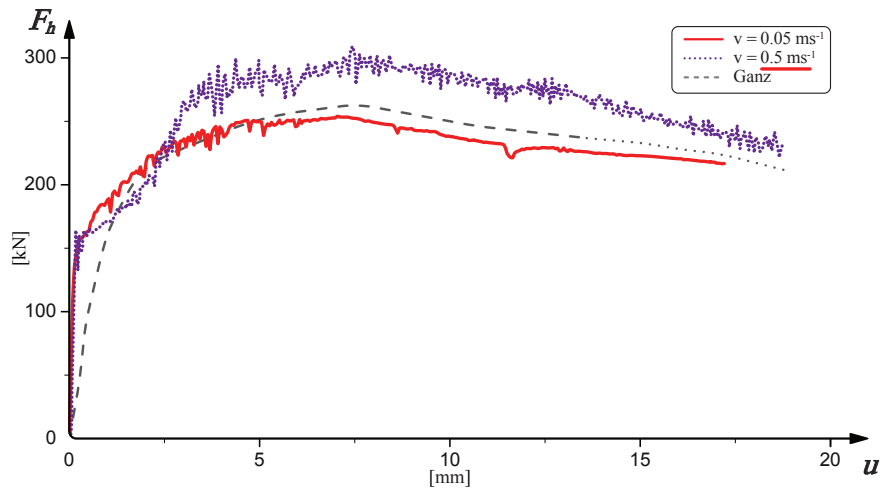


Figure 5.15: Comparison of the horizontal force-displacement curves for the masonry wall between the finite-element analysis (continuous red line and dotted blue line) and the experimental results (dashed gray line) of Ganz [Ganz 84].

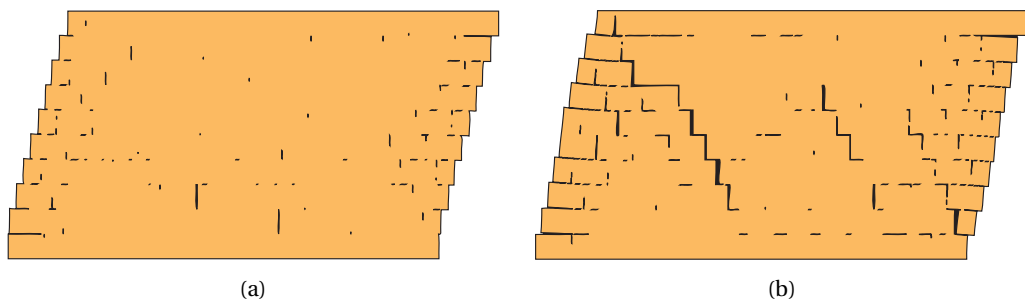


Figure 5.16: Deformed mesh configuration (at  $u = 14.5 \text{ mm}$ ) for shear velocity of (a)  $0.05 \frac{\text{m}}{\text{s}}$  and (b)  $0.5 \frac{\text{m}}{\text{s}}$  (magnification factor 25).

### 5.5 Conclusions

In this chapter the numerical model is enriched with the introduction of a frictional contact and a new cohesive law to account for crack propagation under mode mixity. The debonding process is controlled by a traction separation law based on the popular linear extrinsic irreversible law proposed by Camacho and Ortiz [Camacho 96]. The law has been modified in order to account for path dependent behavior and therefore to introduce a mode-dependent fracture energy. The impenetrability condition is enforced by the DCR contact algorithm developed by Cirak and West [Cirak 05]. We resort to the classical law of unilateral contact and Coulomb friction. The contact algorithm is coupled together with the cohesive approach in order to have a continuous transition from crack nucleation to the pure frictional state.

The model has been validated by simulating a representative shear test on a masonry wallette. Furthermore, the calibrated values for the interfacial transition zone in the wallette application have been used to reproduce a test on a masonry wall loaded in compression and shear. The numerical results have shown the capability of the model to represent the physical process involved during cracking in compression and to give a good prediction of the structural response of the tested units. This is achieved with a relatively simple model, which does not involve many parameters.

This formulation will be applied for the simulations under compressive loading of meso-scale concrete specimens in the next chapter to capture the interlock between the generated cracked surfaces.

# 6 Compressive behavior of concrete under dynamic loading

In this chapter the two-dimensional meso-mechanical finite-element model is applied to analyze failure of concrete specimens subjected to compression. The content of the chapter summarizes the work published in [Snozzi 12a]. Our intention is to extend the mesoscopic approach that has been already applied to tensile loading in Chapter 4 by including the formulation presented in Chapter 5 for mode II debonding of cohesive surfaces under the presence of (local) compression.

In this chapter we will verify if the approach is able to reproduce the asymmetric tensile/compressive behavior, strain-rate strengthening and confinement effects. We also quantify the increase in the ratio between dissipated frictional energy and dissipated fracture energy as the confining pressure is augmented.

The chapter is composed as follows. In Section 6.1 the meso-geometry with its material parameters is presented. Results are reported in Section 6.2 for uniaxial compression. While results on biaxial compressive loading are listed in Section 6.3. Finally, concluding remarks are stated in Section 6.4.

## 6.1 Meso-scale geometry

### 6.1.1 Mesh generation and aggregate distribution

The specimen geometry has been obtained using a pseudo-random generator of irregular polygons. The polygons, which represent aggregates, are created according to a chosen specific distribution. According to this, the approximate total number of inclusions can be first determined before the geometry is generated. The boundaries of each aggregate are then created by generating its faces; a random length is assigned to every edge (as well as an arbitrary angle with the previous edge). However, these values have to lie between given threshold values. Consequently, small inclusions are more likely to get fewer edges, while bigger ones show more faces. Finally, the polygons can be placed randomly into the sample starting from the biggest ones and avoiding possible intersections with the already present inclusions by changing location and rotating them. Although, in order to have a regular

## Chapter 6. Compressive behavior of concrete under dynamic loading

distribution of the phases near the boundaries, the aggregates have been placed in a larger area, from which the specimen has been cut out. Inclusions with the smallest diameter ranging from 1.5 mm to 20 mm have been considered in this work. The distribution has been chosen according to the Fuller and Thompson density curve [Fuller 06] with a value for the exponent  $q$  equal to 0.7.

$$A(d) = \left( \frac{d}{d_{max}} \right)^q \quad (6.1)$$

Where  $A(d)$  represents the percent by weight (cumulated mass under a given diameter  $d$ ) and  $d_{max}$  the largest aggregate in the mixture. This idealized curve is plotted in Figure 6.1a together with the recorded distribution within the sample having the generated meso-structure of Figure 6.1b. The obtained distribution differs from the reference one of Eq. 6.1 in its starting value (since inclusions smaller than 1.5 mm have been not represented explicitly) and in the discontinuous shape (small specimen size and discrete inclusions).

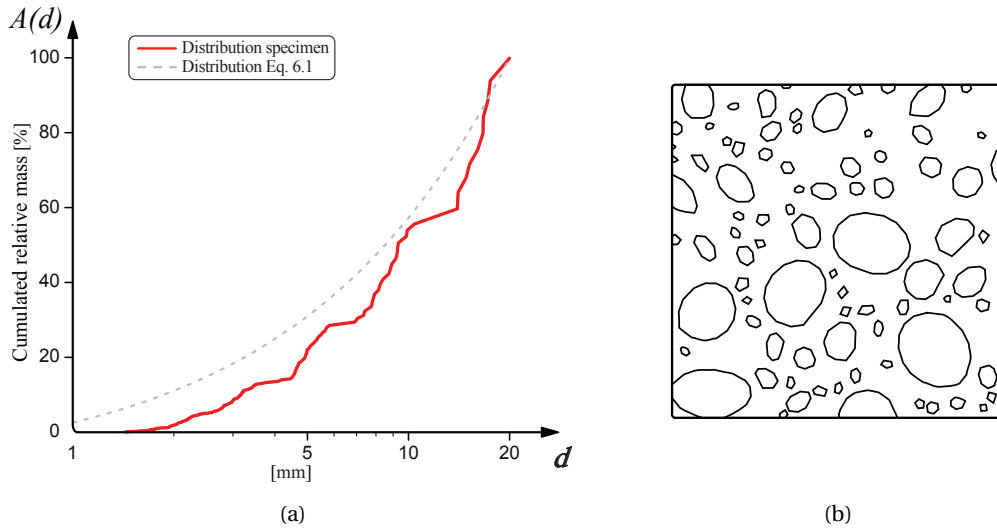


Figure 6.1: (a) Computed cumulated aggregates size distribution of the concrete meso-structure (b).

The resulting ratio of aggregate area is around 31 % of the specimen area, which is a square with an edge size equal to 100 mm. For the remainder of the chapter we have kept the same geometry for every simulation. Indeed, a different meso-structure with a similar distribution would not affect significantly the results as reported in [Gatuingt 12] for tensile loading (since the specimen dimension can be considered large enough). Note that if we compare the generated geometry with a section obtained by cutting a real concrete specimen (showing the same aggregates distribution), they will look rather different. However, the assumption of using the Fuller curve in two dimensions can be considered adequate for the strain plane assumption (since inclusions are considered to be right prisms).

## 6.2. Uniaxial compressive loading

From this geometry one can obtain meshes with different element sizes. Since a convergence study on mesh sensitivity has already been performed in Chapter 4, we have set directly the value of the average element size to 0.5 mm (which gives a mesh with roughly 120000 nodes).

### 6.1.2 Material parameters

The meso-mechanical approach requires defining the material properties for every components. In Table 6.1 the material properties for the inclusions and matrix paste are summarized. Those values are generic and suitable for a usual concrete and are similar to the values used in Chapter 4. The values for the three different interfaces are reported in Table 6.2. These

Table 6.1: Material properties of the concrete's components.

Material	Density – $\rho$ [ $kg/m^3$ ]	Young's modulus – E [GPa]	Poisson's ratio – $\nu$ [-]
Aggregate	2700	75	0.2
Cement paste	2200	30	0.2

material properties can be determined experimentally (for instance [Rosselló 06]). For this work we have chosen values of the cohesive properties ( $G_c$  and  $\sigma_c$ ) similar to the ones reported in Chapter 4 ([Gatuingt 12]) while the remaining pair ( $\beta$ ,  $\kappa$ ) had to be identified through a parametric study as reported in Section 6.2.

Table 6.2: Cohesive properties and selected parameters for the interfaces.

Interface	Fracture Energy $G_c$ – [ $J/m^2$ ]	Tensile Strength $\sigma_c$ – [ $MPa$ ]	$\beta$	$\kappa$	Friction Coefficient $\mu$ – [-]
Aggregate	60	16	3.5	10	0.7
Mortar	50	4.7	3.5	10	0.7
ITZ	30	2.7	3.5	10	0.7

## 6.2 Uniaxial compressive loading

In this section we analyze the dynamic compressive response of the concrete model.

### 6.2.1 Initial and boundary conditions

The samples are loaded under displacement control with an imposed strain rate  $\dot{\epsilon}$ .

$$V_y(y) = \frac{2V_0}{h} y \quad (6.2)$$

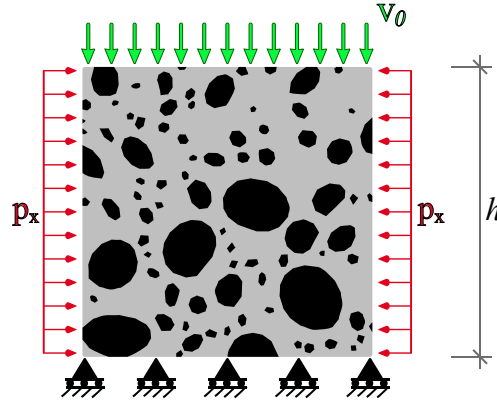


Figure 6.2: Boundary and initial conditions for specimen loaded in compression.

Note that even if the linear gradient is not exact in case of a heterogeneous material, the selected initial condition does not lead to oscillations at early stage of loading. As depicted in Figure 6.2 all the nodes located at the upper edge of the finite element mesh are forced to move at a certain constant velocity  $V_0$ :

$$V_0 = -\dot{\epsilon}h \quad (6.3)$$

Whereas, the lower boundary is supported in  $y$ -direction and therefore the motion of the nodes belonging to this edge is blocked in the vertical direction (while the horizontal displacement of the nodes is unconstrained). If lateral confinement ( $p_x$ ) is applied (Section 6.3), the sample is first loaded statically with a hydrostatic pressure corresponding to  $p_x$ . After this step, the dynamic loading is applied until the end of the simulation.

To obtain the stress-strain curves presented thereafter, we define the macroscopic stress ( $\sigma$ ) as the boundary reaction force  $F_y$  divided by the initial width, and the macroscopic strain ( $\epsilon$ ) as the change in height divided by the initial height  $h$ . The compressive stress and compressive strain are identified with  $\sigma_c$  and  $\epsilon_c$  respectively. Moreover, during simulation, a slight material damping has been adopted in order to compensate for the slight increase of internal energy (due to the enforcement of the impenetrability through projection [Cirak 05]) and reduce numerical oscillations.

### 6.2.2 Identification of model's interface parameters through simulations

In order to identify the two remaining parameters of the cohesive law,  $\beta$  and  $\kappa$ , we have ran some simulations in order to extract them indirectly by comparing the macroscopic stress-strain relationship with a semi-analytical model for concrete proposed in [Fernández Ruiz 07] for the compressive behavior.

Since these two parameters influence mode II cracking, and have therefore little influence

on the peak tensile strength and more generally on the global macroscopic behavior of the specimens subjected to uniaxial tension, the fitting has been conducted by examining the response in unconfined compression for a loading rate  $\dot{\epsilon} = 1 \text{ s}^{-1}$ . The influence of  $\beta$  has been investigated first. Its value affects the shear strength of the interfaces, which changes considerably the compressive peak strength of concrete as depicted in Figure 6.3a. With an increasing value of  $\beta$ , one obtains a higher compressive strength. Since with the interface

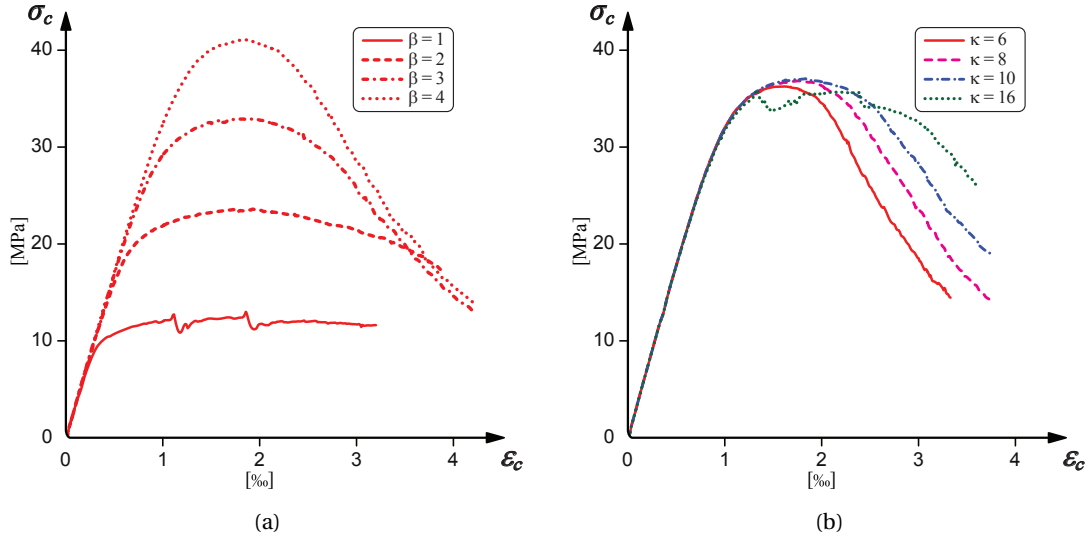


Figure 6.3: (a) Influence of the  $\beta$  parameter on the compressive stress-strain behavior of concrete (for  $\kappa = 10$ ) and (b) influence of  $\kappa$  (with  $\beta = 3.5$ ) for  $\dot{\epsilon} = 1 \text{ s}^{-1}$ .

properties of Table 6.2 a tensile strength slightly lower than 4 MPa (precisely 3.67 MPa) is obtained, the authors have decided to set the value of  $\beta$  equal to 3.5 (a lower value compared to the one chosen in [Ruiz 00]). This leads to a compressive strength roughly one order of magnitude higher than the tensile one (see Figure 6.2), which seems a usual ratio for a conventional concrete. The stress-strain behavior is also affected by  $\kappa$ , which increases the dissipated fracture energy and therefore modifies mostly the post-peak behavior and shifts the transition to softening towards higher strain values. This trend is graphically illustrated in Figure 6.3b. Therefore, in order to obtain a concrete with softening starting around  $\epsilon_c = 0.002$  (which is a usual value for the peak strain of conventional unconfined concrete) we decided to fix the value of  $\kappa$  at 10 (same ratio between fracture energies estimated by Carol *et al.* [Carol 01]). Note that this relatively high value should take into account frictional effects that might occur for low normal openings of the surfaces that are not taken into account by the frictional contact algorithm. This results in a concrete with a compressive strength of roughly 36.8 MPa at a compressive peak strain around 0.0019. The obtained constitutive response is compared in Figure 6.4a with the constitutive model proposed in [Fernández Ruiz 07]. The computed peak strain and stress are in the same range of the experimental values ( $\epsilon_{peak} = 0.0018-0.0021$  and  $\sigma_{peak} = 32.8-38.8$ ) recorded by [Sfer 02]. Note that we could not compare directly the

curves since the experimental unconfined response is not drawn in [Sfer 02]. Nevertheless, we will have recourse again to the data reported in this reference for the comparison with the confined response in compression (Section 6.3). The stress-strain behavior is depicted for

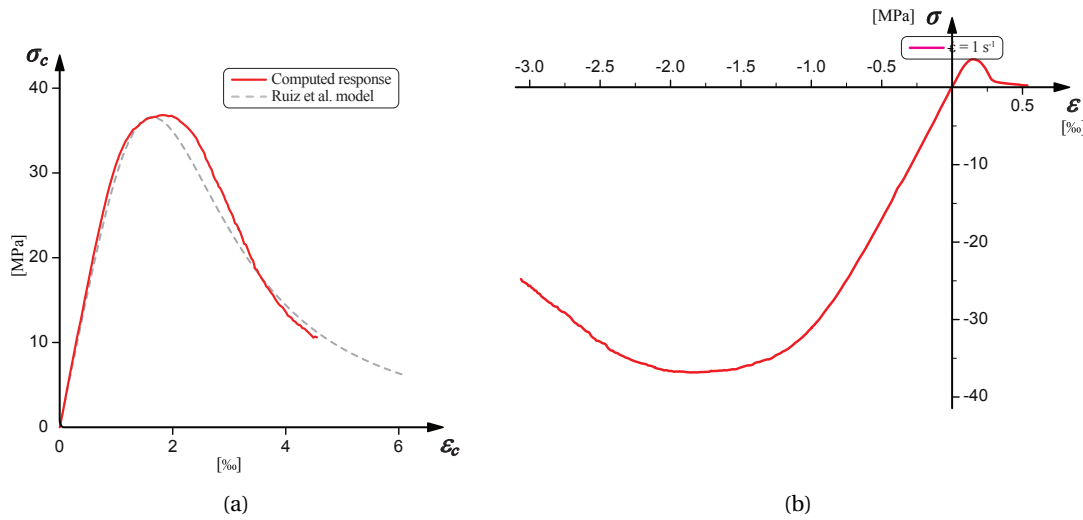


Figure 6.4: (a) comparison with empirical model of [Fernández Ruiz 07] and (b) asymmetric tensile/compressive behavior of concrete ( $\dot{\epsilon} = 1 \text{ s}^{-1}$ ).

tension and compression in Figure 6.4b. It is clear that the tension/compression asymmetry is well captured.

### 6.2.3 Rate effect

In this subsection we analyze the behavior of concrete subjected to unconfined compression under different loading rates.

As for tension, experimental results [Bischoff 91] show a clear rate sensitivity under compressive loading. Commonly, the stress increase can be explained with lateral inertial confinement (Poisson's effect) and a more diffuse micro-cracking beside eventual material rate hardening mechanisms.

Figure 6.5 shows the computed stress-strain curve for different loading rates. The results display a strain-rate hardening with a DIF of about 1.9 for a strain rate of  $\dot{\epsilon} = 100 \text{ s}^{-1}$ . In contrast to our computed tensile DIF ( $\approx 2$ ), this increase factor is consistent with experimental results [Bischoff 91]. This results highlights the strong effect of lateral inertial confinement alone that can explain the increase in strength as noticed in [Donzé 99] too. Indeed, in our simulations, we do not consider any rate effect at the material level.

Figure 6.6 shows the crack pattern for  $\dot{\epsilon} = 1 \text{ s}^{-1}$  and  $100 \text{ s}^{-1}$ . Cracks tend to propagate within



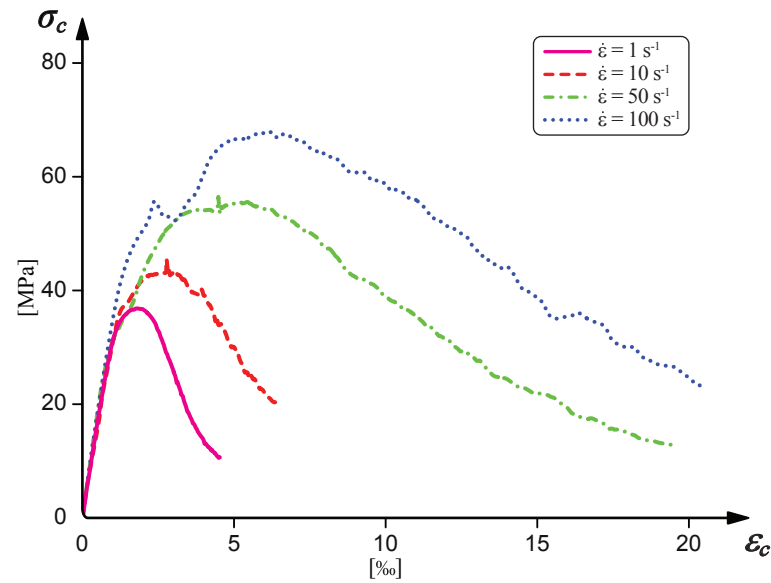


Figure 6.5: Stress-strain response for different strain rates under compressive loading.

the matrix phase bypassing the inclusions except for few big aggregates that have been crossed. One can notice that due to the absence of a horizontal constraint at the upper and lower

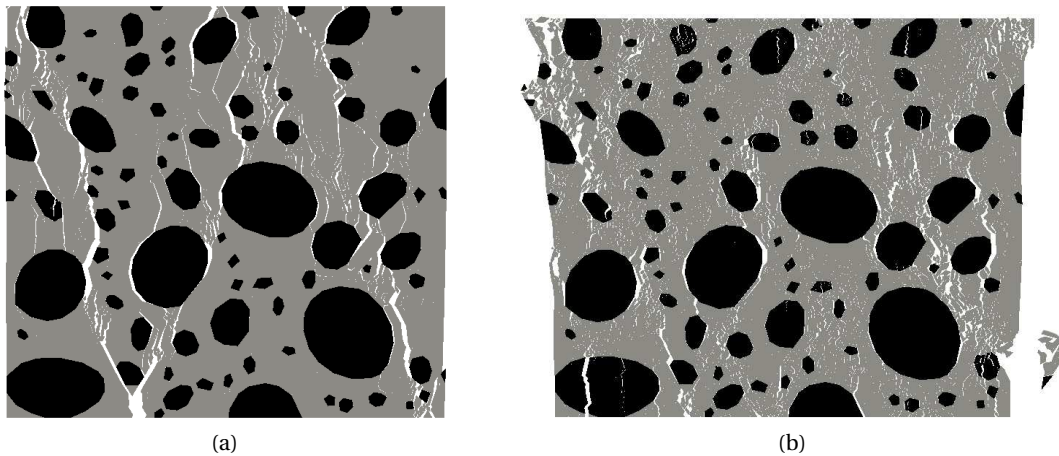


Figure 6.6: Influence of strain rate on the crack path in compression: (a)  $\dot{\epsilon} = 1 \text{ s}^{-1}$ , (b)  $\dot{\epsilon} = 100 \text{ s}^{-1}$ . Note that the displacement field has been magnified by two different factors: 4 in (a) and 2 (b).

boundaries of the specimen, the crack pattern does not show the formation of a characteristic cone, as mostly observed during simple compression experiments. Moreover, the cracks are aligned parallel to the loading direction, conversely to a perpendicular orientation in case of tension.

The evolution of the dissipated fracture energy ( $W_G$ ) and frictional work ( $W_\mu$ ) in the specimen

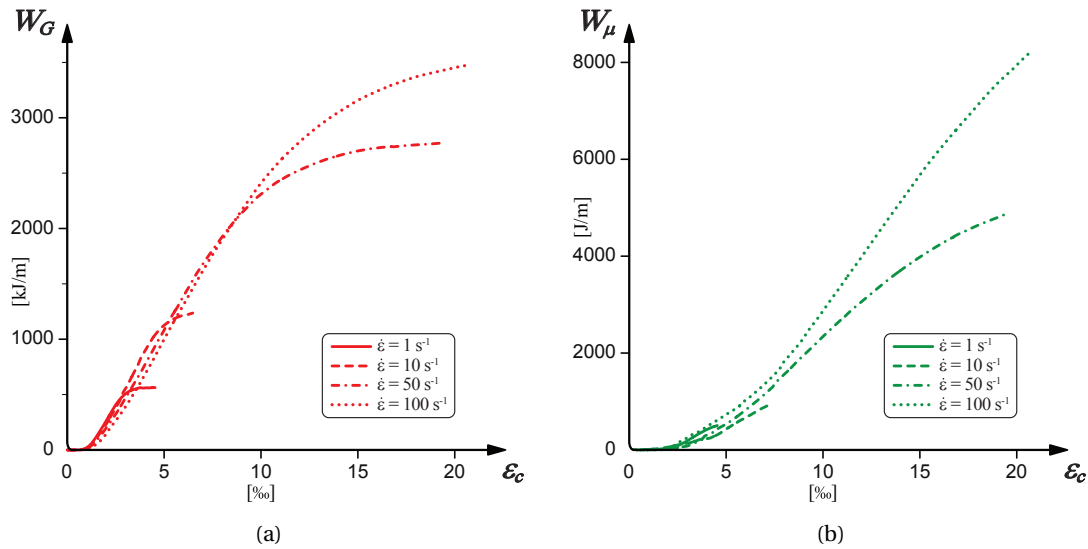


Figure 6.7: (a) Dissipated fracture energy and (b) dissipated frictional work for different loading rates.

is depicted in Figures 6.7a and 6.7b respectively. Both figures show that the raising number of cracks with increasing strain rate causes a higher dissipation of energy within the damaged specimen. This mechanism leads to a higher compressive strength and larger area (thus toughness) under the stress-strain curve. In particular, the post-peak dissipation of energy seems to be affected more by friction than by dissipation of fracture energy. Therefore, the gain in strength can be traced back to an inertial effect alone (as suggested for instance in [Cotsovos 08]).

### 6.3 Influence of lateral confinement

We now investigate the behavior of concrete subjected to moderate lateral confinement under a strain rate  $\dot{\epsilon} = 1 \text{ s}^{-1}$ . The concrete specimens have been subjected to four level of transversal confinement pressures ( $p_x$ ): 4.5, 9, 12 and 30 MPa (for comparison with experiments).

Figure 6.8a shows that the confining stress increases substantially the compressive strength as well as the longitudinal compressive peak strain. Moreover, one can notice that confining concrete results in a decrease of the slope of the post-peak branch indicating therewith a moderate rise in the ductility of concrete. Among the several data that one can find in the experimental literature of the stress-strain behavior, we have selected the data on triaxial loading reported in [Sfer 02] for a direct comparison. As previously commented the concrete tested in this reference almost matches in terms of peak strength and peak strain the computed response in the unconfined case. The comparison between simulations and the results is

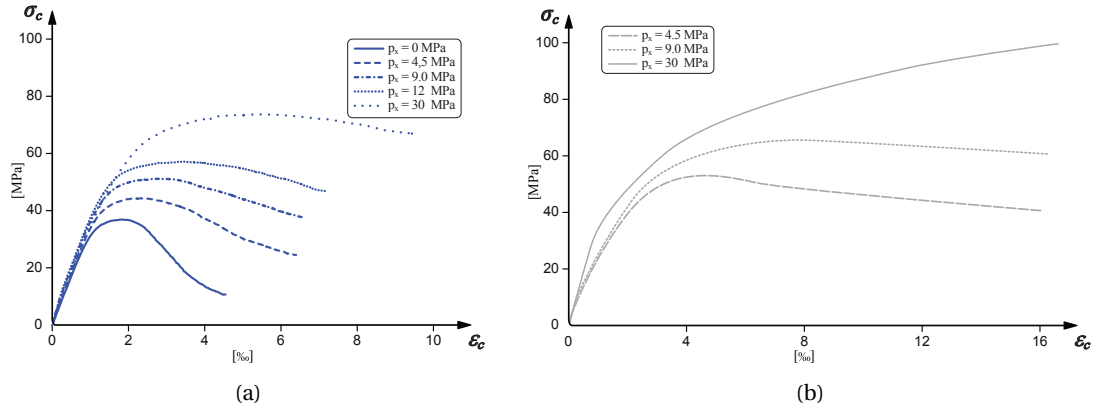


Figure 6.8: (a) Influence of confining pressure on the stress-strain behavior ( $\dot{\epsilon} = 1 \text{ s}^{-1}$ ) and (b) experimental results of [Sfer 02].

illustrated in Figure 6.8. As already noticed, one can remark that the increase in peak strength with lateral confinement in the simulations is lower than the one obtained experimentally. Additionally, one can compute the gain in concrete strength of the confined specimens. Usually, in concrete research, the Mohr-Coulomb failure criterion can be assumed to describe the sliding failure in a confined concrete. This can be expressed as follows:

$$\sigma_c = f_c + k * p_x \quad (6.4)$$

where  $f_c$  represents the unconfined compressive strength of concrete and  $k$  is a constant, which is usually set to four [Richart 29, Lahlou 92, Candappa 01] for triaxial tests. In our case, we obtain a  $k$  with a value somewhat lower than two for low confining pressures (and that becomes even smaller if moderate pressures are considered), while the increase measured by [Sfer 02] (Figure 6.8b) gives a  $k$  of roughly 3.5. Moreover, the values recorded by [Sfer 02] show a considerable rise in ductility of the specimen with larger confinement. While simulations show only a moderate increase. This becomes more evident for the highest confining pressure (30 MPa) considered here. At such confining pressures the specimen response is probably dominated by physical interactions at the micro-crack level that our model seems to reproduce less accurately. The failure mechanism shifts from damage due to strain extension to compaction due to porosity reduction. Some authors (*e.g.* [Camborde 00]) are able to reproduce compaction with a lattice based discrete element method introducing a phenomenological model in their beam behavior. Another reason for the too little hardening could partially reside in an insufficient dissipation of frictional energy in our simulations, which leads to a larger negative slope after the peak strength has been reached. A better modeling could perhaps be obtained by increasing the value of the friction coefficient and acting on the coupling (apart from changing the value of the pair  $\beta$  and  $\kappa$ ). Indeed, the chosen onset of friction implies an initiation of cracks that is not influenced by the level of applied lateral pressure. In addition, it should also be pointed out that the chosen 2D framework is

## Chapter 6. Compressive behavior of concrete under dynamic loading

limited and cannot capture realistic 3D micro-cracking networks. Indeed in three dimensions to reach percolation is more difficult than in 2D, where cracks can coalesce easily. This implies that in 2D the obtained micro-cracks density might be underestimated and consequently the dissipation of energy as well. Moreover, the three-dimensional representation of cracks, should also lead to a much bigger dilatancy of cracks and thus to an increase in the ductility of the specimens. This work can be considered as a first attempt to extract concrete behavior from a new approach and the foreseen improvement clearly requires an extension to 3D.

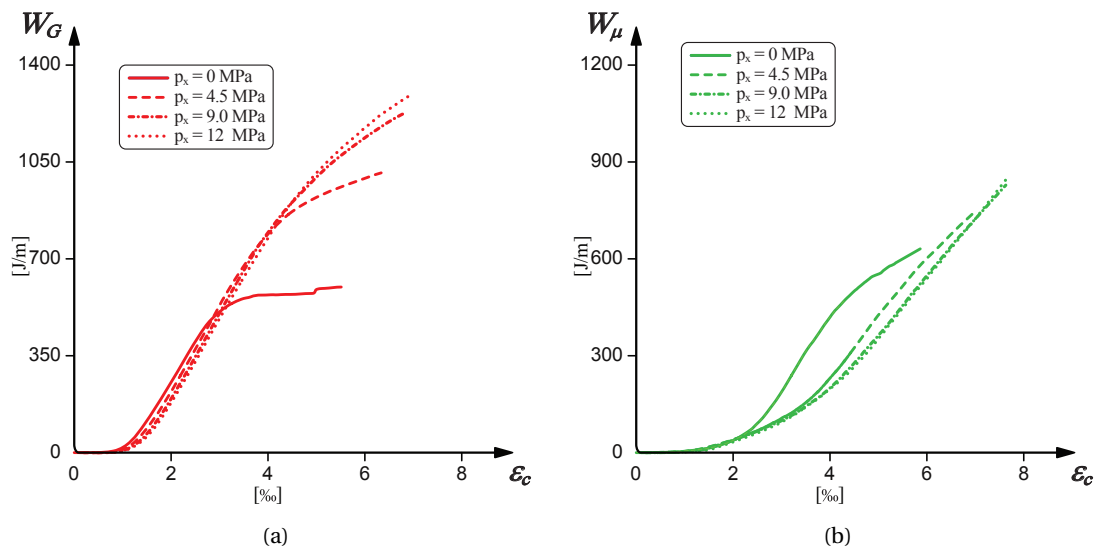


Figure 6.9: (a) Dissipated fracture energy and (b) frictional work for  $p_x = 0, 4.5, 9$  and  $12$  MPa ( $\dot{\epsilon} = 1 \text{ s}^{-1}$ ).

The comparison between the dissipated energies is illustrated in Figure 6.9. From Figure 6.9a one can remark that an increase in the lateral confinement will delay the opening of cracks and thereafter the start of the dissipation of fracture energy. This phenomenon has already been observed with a meso-scale modeling of ceramics [Warner 06, Kraft 08].

However, the rise in the horizontal pressure ultimately increases the amount of dissipated fracture energy. This is because cracks are more prone to open following a mode II fashion, which is bounded with a larger value of stored fracture energy than mode I, and also because there is a more diffuse fine crack network. Figure 6.10 shows this crack network. It also illustrates that applying a confinement pressure forces the cracks to propagate at a faulting angle of roughly  $30^\circ$ , whereas their paths were more vertical for unconstrained compression (Figure 6.6a). The increase in the faulting angle orientation, from axial splitting for unconfined concrete to shear faulting for specimens subjected to lateral confinement, appears to be in agreement with analytical models (see for instance [Horii 85] for rock mechanics).

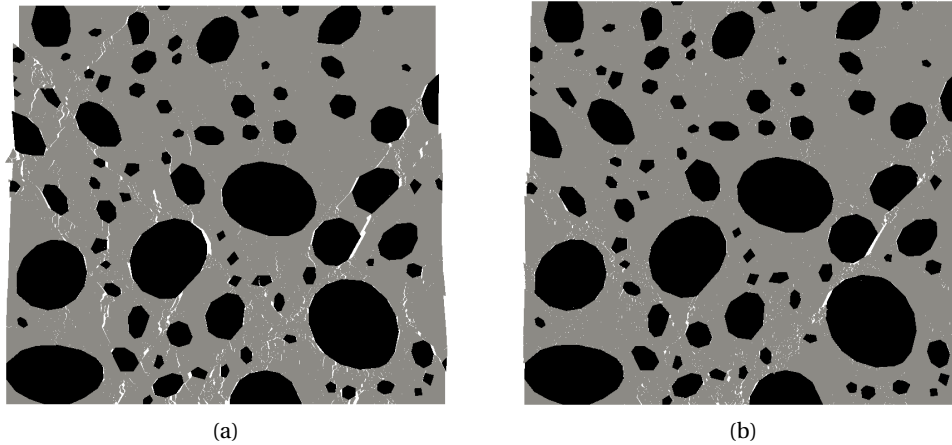


Figure 6.10: Deformed specimens for confinement pressures of (a) 4,5 Mpa and (b) 12 MPa. Displacement has been magnified by a factor of 5.

Since we are using an explicit representation of cracks, it is possible to monitor their time evolution and to extract relevant information. We have chosen to follow the formation of the longest crack cluster (which is a group of fully broken interfaces which are interconnected to each other),  $L_{c,max}$ , as well as the total number of crack clusters  $NB_c$  (as was done for ceramics in [Warner 06, Kraft 08]). The first variable has been normalized with the edge size of the specimen. As already observed, an increase in the level of confinement produces a

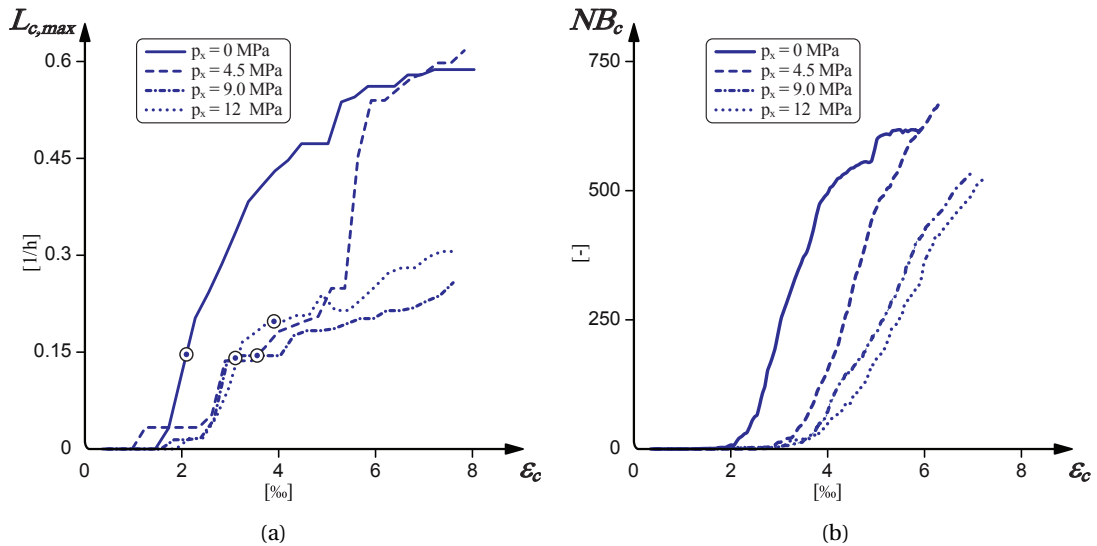


Figure 6.11: (a) Maximal cluster length normalized over specimen size  $h$  and (b) number of cracks for  $p_x = 0, 4.5, 9$  and  $12$  MPa. The length at which softening starts, represented by circles on graph (a), does not depend on the amount of confinement.

delay in the formation of the first cluster. This is noticeable from both graphs of Figure 6.11. Moreover, from the first graph (Figure 6.11a) one can see that the application of a horizontal pressure causes the longest crack to be relatively shorter with a length of the range of  $0.2h$  (unfolded length) until the negative slope of the softening becomes more pronounced. On the other hand, the number of clusters is not much affected by the application of lateral confinement as depicted in Figure 6.11b. The unconfined sample shows initially a larger number of cracks than the confined ones, which implies that the lateral pressure delays the onset of micro-cracks coalescence. This can be confirmed by looking at the deformed mesh configuration. One can see from Figure 6.10 that the application of the confinement pressure triggers a finer net of smaller cracks, which exhibit a smaller opening (and are thus not completely debonded). Finally, by looking at Figure 6.11a, it appears that the softening phase can start, for the three confined cases considered here, when the longest cluster reaches a length of approximately  $0.15 - 0.2h$  (circles on the strain- $L_{c,max}$  curve indicate the strain immediately after peak strength has been reached) and thus does not depend on the level of applied confinement (for the unconfined sample the transition is less clear to identify, since the transition to a macroscopic crack is more rapid).

Note that the total length of a cluster has been considered here, whereas if one looks at the cluster length projected on a line (similarly to what reported in [Prado 03] for tensile loading), its maximal value will not increase much after the softening has started. That is, the maximal projected length tends to stabilize around  $0.2 - 0.15h$ .

### 6.4 Discussion and Conclusions

In this chapter we have simulated failure of concrete specimens under compressive regime. To this end the meso-mechanical approach previously applied to tensile loading (Chapter 4) has been enriched with the cohesive/frictional capability presented in Chapter 5. From the obtained results we can draw the following conclusions.

The model naturally reproduces the characteristic asymmetric tensile/compressive behavior of concrete. Similarly to tensile loading, simulations in compression show that the model gives an increase in peak strength and strain at failure with increasing rate of loading although the interfacial constitutive law is rate independent. This rise in strength resides in a more diffuse micro-cracking and is thereby bounded with a higher dissipation of fracture energy as well as energy dissipated through friction.

A comparison between our simulation results and experimental literature indicates that inertial forces alone are sufficient to explain the increase in strength with increasing loading rate excluding thus further strain-rate dependence at the material level (material hardening). Specimens subjected to lateral confinement in compression exhibit an increase in peak strength and strain at maximum stress with increasing confining pressure. However, the rise in strength is lower than experimental reported values. It has been observed that an increase in the lateral pressure produces delays in the formation of the first crack cluster and in micro-cracks

coalescence. Dissipation of energy through fracture and friction is also an increasing function of the applied confinement. The model also shows the importance of capturing frictional mechanisms, which appear to dissipate a raising amount of frictional energy with increasing strain and applied pressure (the work done by friction is on the same range of magnitude as the energy dissipated trough crack opening under compressive loading).

It is however important to emphasize that our model needs further improvement to capture experiments better. In particular, the ductility of the specimen is less affected by the confining pressure than the one measured experimentally and the post-peak behavior remains more brittle. This could perhaps be related to a yet insufficient increase in the amount of dissipated frictional energy or to the lack of others physical phenomenon in the model (such as compaction). Moreover, the chosen 2D setting is limiting to capture the complexity of 3D micro-cracking. Indeed, in 2D the density of the cracks is underestimated since it is easier to reach percolation than in 3D.

Besides this, the influence of the internal ordering of the meso-structure has not been investigated in this chapter. This model has been included in the multi-scale framework, proposed in the next Chapter, to simulate the behavior of concrete (including asperities interlocking) at the fine scale.





## 7 Multi-Scale modeling

As stated in the introduction chapter, concrete is a good example of a construction material that at the structural level is often considered homogeneous but reveals a heterogeneous nature at a lower level of observation. The advantage of a low level of observation is that it allows an explicit representation of some concrete ingredients, and thus enables to reduce the number of model parameters and describing the interactions between matrix and inclusions. It follows that the Direct Numerical Simulations (DNS) of specimens provide a rich set of results. However, if real size structures need to be analyzed this technique requires too high computational costs.

To overcome this problem it is possible to have recourse to multi-scale models. These methods provide accurate solutions at a computational cost that is substantially lower compared to DNS. Homogenization is based on the principle of separation of scales, which requests the characteristic length of the fine scale heterogeneities to be much smaller than the characteristic length of the macro-scale. Moreover, another assumption that is often pursued postulates periodicity of the micro-structure within the macro-domain. This entails that the coarse scale problem can be assumed to be composed by repeated unit cells or, alternatively, by regions showing the same micro-structural morphology.

Therefore, the idea beyond homogenization is that the entire macro-domain can be solved by a sequence of representative volume elements (RVEs). Once the necessary macroscopic quantities have been determined (typically deformations, *i.e.*  $\mathbf{F}_M$ ), they can be transferred and applied to the cells, over which an analysis is performed to obtain the quantities of interest (typically stresses, *i.e.*  $\mathbf{P}_M$ ) that are collected back and transferred to the coarse scale. This procedure is schematically illustrated in Figure 7.1b. The implementation of the entire framework in a parallel environment is consequently particularly attractive, since it allows to run sequential simulations on every available processor of a computer cluster as depicted in Figure 7.1a. For the remainder of the chapter the subscript “M” indicates a macroscopic quantity, while the subscript “m” refers to a microscopic quantity.

Computational multi-scale techniques, which allow for both the macro and the micro-scale to be modeled, have been developed by several authors during the past years. Within the field of

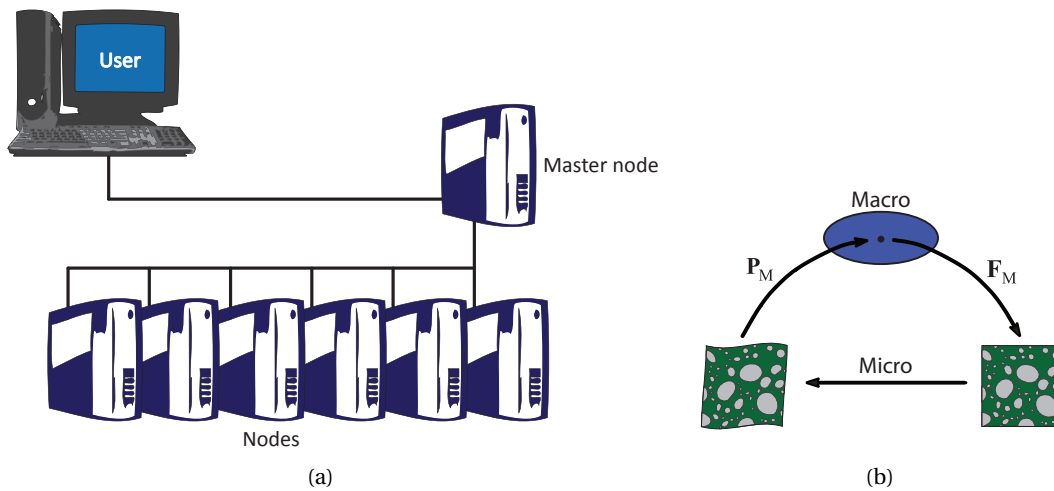


Figure 7.1: (a) parallel computational framework exploited for multi-scale simulations (the master nodes queues the jobs distributing them between the cluster nodes). (b) Homogenization scheme.

computational homogenization, a significant contribution is represented by methods having recourse to an explicit modeling of the fine scale structure through a RVE, as firstly proposed in [Suquet 85, Renard 87]. However, the RVE existence requires a clear separation of scales such that the hypothesis of uniformity of macroscopic strains holds over the micro-structure. To this end the RVE dimensions are chosen much smaller than the coarse scale size in first order scheme. Higher order gradients [Kouznetsova 02, Feyel 03] are adopted, when first order classical computational homogenization fails to satisfy the principle of separation of scales allowing thus moderate strain localization. An extensive study over the available computational schemes for first-order and second-order scale transition can be found in [Geers 10].

Nevertheless, problems that entail damage mechanisms occurring at the micro-structural level (with consequent up scaling) represent a raising subject of interest in simulation-based engineering field. For materials that undergo softening at the finer-scale, other methods need to be considered in order to avoid possible scale separation problems that arise during localization. In [Gitman 08] a method called coupled volume approach has been presented. This approach, based on a classical first-order homogenization technique, includes the micro model directly into the macro-model. Consequently, the homogenized behavior is not extracted from a RVE (since it is not thought to exist) but from a material sample, which shows the same dimensions as the associated macroscopic element. Similar approaches have been presented in [Markovic 06, Kaczmarczyk 10].

An additional approach is represented by embedded concurrent multi-scale approaches (for instance [Hirai 84] or more recently [Unger 11]). In this class of methods, the problem is discretized at the beginning of the simulation only at the coarse-scale, while the fine scale is activated on the fly, only at necessary locations through an adaptive technique.

A further approach, for micro-macro up scaling, is represented by the multi-scale cohesive /adhesive failure, which incorporates the behavior extracted from the fine-scale into a macro-scale fracture model.

The application of this method in a  $FE^2$  setting, can be traced back to the work presented in [Kulkarni 10] and [Verhoosel 10]. The latter work proposed a homogenization methodology that was applied besides adhesive fracture to cohesive failure of a heterogeneous microstructure. Similar results have been reported by Nguyen [Nguyen 10b, Nguyen 11, Nguyen 12], who provided comparison with DNS and simulations of a Double Cantilever Beam (DCB).

In this work we aim to extend this line of thought by extending the method developed by Verhoosel *et al.* [Verhoosel 10] to explicit dynamics, which implies that strain-rate effect can be represented too. In addition, in the proposed framework besides cracking the onset of friction is also considered at the RVE level. Special periodic boundary conditions (similarly to the one reported in [Coenen 12]) have been applied to the RVEs in order to allow the propagation of arbitrary crack path within the RVE and thus to reduce macroscopic mesh dependency.

The chapter is organized as follows: Section 7.1 summarizes the adopted formulation at the macro and meso-scale level, followed in Section 7.2 by a description of the chosen multi-scale cohesive up scaling. Results are reported in Section 7.3, where the solution provided by the multi-scale method is compared first to a DNS (substantially mode I) and second to experimental recorded values of a push-off test (which involves shearing of the cracks). Finally, closing remarks are stated in Section 7.4. This chapter will later be submitted to a numerical methods journal.

## 7.1 Multi-Scale framework

The following section summarizes the adopted finite-element framework to model the macro and the meso-scale simultaneously. At both scales the scheme, in order to find equilibrium, needs to solve the discretized equation of motion (Equation 3.13) with the procedure described in Chapter 3.

### 7.1.1 Macroscopic modeling

As usual in computational homogenization at the macro-scale the material is assumed to be homogeneous. However its constitutive response is determined from the homogenized quantities obtained from the lower-scale. The continuum is assumed to behave linear-elastically with effective properties according to the chosen meso-scale cell. However, if the bulk elements experience too large deformations, cracking occurs and the crack propagation is modeled by dynamically-inserted zero-thickness interface elements. The macroscopic fracture process is thus described by the cohesive approach (Chapter 3). The computed displacement jump ( $\Delta$ ) at each quadrature point is imposed on a meso-scale RVE, from which the corresponding cohesive tractions are extracted. The mechanical response of the macroscopic discontinuity is thus determined from the meso-structure, establishing the macroscopic traction separation

law (TSL):

$$T = T(\Delta) \quad (7.1)$$

Details about the adopted up scaling procedure are given in Section 7.2. Outside this zone the bulk material remains undamaged and it continues to behave linear elastically.

### 7.1.2 Meso-scale formulation

In this subsection, a simple test demonstrating the existence of an RVE made of concrete is given. Furthermore the description of the adopted boundary value problem is outlined. The constitutive model adopted for this fine-scale is the same as the one presented in the previous chapter.

#### Meso-geometry

For the present investigation we generate our geometries using the same pseudo-random mesh generator of irregular polygons already introduced in Section 6.1. Nevertheless, to respect periodicity, the geometry has been modified to be periodic with respect to the principal axis (*i.e.* inclusions intersecting an edge of the specimen must appear on both opposite faces). The aggregate's distribution has been obtained following a Fuller-Thompson grading curve. More precisely, we have chosen to explicitly represent aggregates with a diameter ranging from 1.5 mm to 16 mm. The material properties and interfacial parameters selected are generic and suitable for a usual concrete and reflect those adopted in Chapter 6 (Table 6.1 and Table 6.2 respectively). An example of a generated structure is depicted in Figure 7.2.

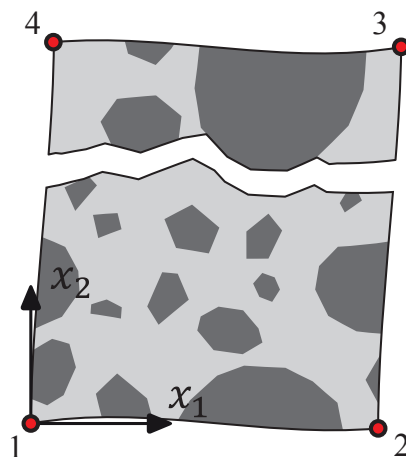


Figure 7.2: Deformed RVE showing a characteristic meso-structure. The numbers from 1 to 4 represent the index of the corner nodes.

### Choice of the Representative Volume Element (RVE)

A question that often arises from computer-modeling, is related to the specimen size that should be adopted for virtual experiments, in order to gather a representative response from the sample. This concept is very important for multi-scale simulations, where the choice of an appropriate representative volume element (RVE) is crucial and determines the accuracy of the model. Even in case of linear elasticity, the homogenized properties can be under/overestimated if the selected cell is too small and thus does not contain enough information about the micro-structure itself (see for instance [Terada 00]). More recently RVE existence has been demonstrated in [Gitman 07] for linear and hardening regimes. While in case of softening problems the reader can refer to the proof provided in [Verhoosel 10, Nguyen 10b]. Nevertheless, we report here a brief verification of the RVE existence for our selected mesoscopic model.

### Elastic behavior

There are two fundamental requirements that are necessary for a RVE to be considered appropriate for simulations. First, the selected area should be large enough, in order to contain enough information about the morphological composition of the material. *i.e.* it should be a statistically representative sample of the chosen meso-structure arrangement. This applies also if any multi-scale computation is performed. The second condition states that the employed size should allow a sufficient accuracy in the computation of the homogenized properties. This means that the RVE's size depends on the type of information that are of interest at the macroscopic scale, on the meso-structure heterogeneity and the constitutive behavior assumed for the phases. Thus, a simple validation test, to select a representative RVE, is to perform an analysis varying the size of the specimen to see if the homogenized properties converge with increasing RVE size.

We report here a verification of the elastic properties for different meso-scale samples sizes presenting an irregular arrangement of the meso-structure. If the selected specimen is too small the recorded properties will differ from the "real" one. Whereas, if the sample is large enough the homogenized properties will coincide independently of the applied boundary conditions (BCs). In multi-scale homogenization, different type of BCs can be employed. However, they can all be traced back to three types of BCs.

**Traction boundary conditions** In this case tractions ( $\boldsymbol{p}$ ) are imposed to all the nodes located at the boundary edges of the RVE according to the imposed macroscopic stress  $\mathbf{P}_M$ .

$$\boldsymbol{p} = \mathbf{P}_M \boldsymbol{N} \quad \text{on } \Gamma \quad (7.2)$$

Note that this kind of boundary conditions constitute the weakest kinematic constraint for the displacement of the boundary and that it does not prevent the sample from rotation around a point.

**Displacement boundary conditions** With this type of BCs, the constraint is applied to the displacements of the nodes located on the boundary depending on the applied macroscopic deformation

$$\mathbf{x}_i = \mathbf{F}_M \mathbf{X}_i \quad \text{with } \mathbf{X}_i \text{ on } \Gamma \quad (7.3)$$

Equation 7.3 determines the position of all the points on the boundaries and does not allow, consequently, any fluctuation within the sample edges (*i.e.* edges remains straight).

**Periodic boundary conditions** Periodic boundary conditions are the most widely adopted in the multiscale-community. This kind of condition prescribes the displacements of the corner nodes according to the macroscopic deformation gradient.

$$\mathbf{u}_i = (\mathbf{F}_M - \mathbf{I}) \mathbf{X}_i \quad \text{for } i = 1, 2, 4 \quad (7.4)$$

Where the index  $i$  indicates the corner node considered and  $\mathbf{I}$  stands for identity matrix. The displacement field at the RVE's edges can show fluctuations but these have to be periodic on opposite faces. To depict this let us consider the periodic RVE drawn in Figure 7.3. Periodicity imposes that the displacement of every node located on the top edge (face T in

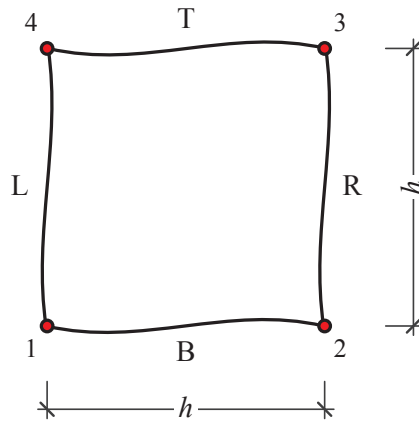


Figure 7.3: Schematic of a two-dimensional RVE.

Figure 7.3) matches the displacement of the corresponding node located on the bottom (face B in Figure 7.3). Assuming that the mesh is periodic, this can be written for every pair of nodes located on opposite surfaces as follows:

$$\mathbf{u}_T = \mathbf{u}_B + \mathbf{u}_4 - \mathbf{u}_1 \quad (7.5)$$

$$\mathbf{u}_R = \mathbf{u}_L + \mathbf{u}_2 - \mathbf{u}_1 \quad (7.6)$$

Note that the constraint of Equation 7.6 is easier to impose if periodic meshes are used. But it can be also applied to non periodic RVEs.

The same kind of constraint has been adopted for the velocities of corresponding (facing) nodes, since the residual forces and accelerations are computed on every nodes, which are composed by assembling the contributions of both opposite nodes. A similar principle is also applied if the number of nodes, at one position, is not the same on both sides (e.g. cracked edge only on one side). In this case the constraint is satisfied in an average sense. In addition, this causes the constraint to be applied on the increment of the displacement at each time step, instead of acting directly on the total displacement.

The geometry generated for assessing convergence of the elastic response is depicted in Figure 7.4a. The meso-structure of the various specimens used in this investigation has been obtained by selecting a specific (decreasing) area on the global surface. The volume fraction of the aggregates is about 30%. While their distribution follow a Fuller curve with diameters ranging from 4 mm up to 20 mm. It is possible to notice that the geometry of the obtained samples is not periodic, which leads to convergence with larger RVE's size.

All the different samples sizes have been loaded under simple shear and tension with the

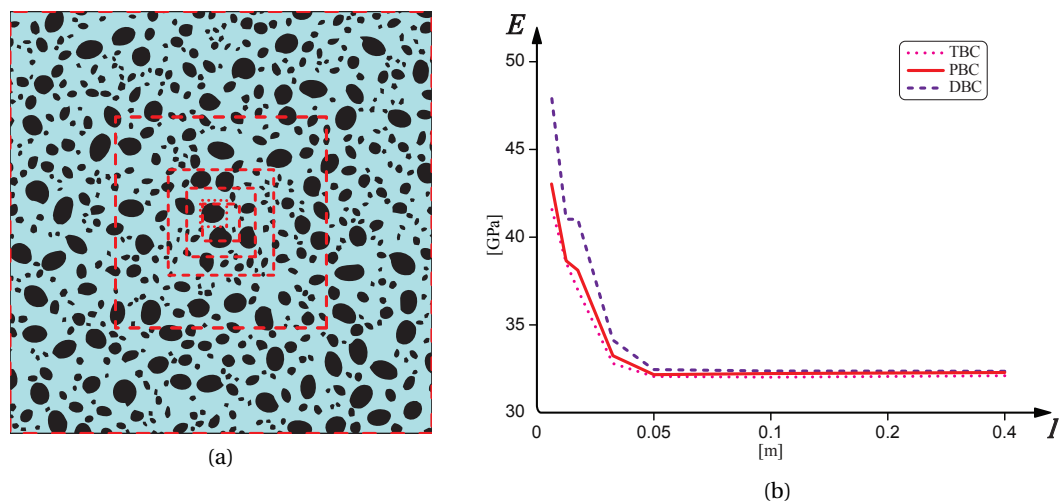


Figure 7.4: (a) Geometry of the meso-structure with the selected RVE regions and (b) resulting macroscopic Young's modulus for homogenized elastic behavior as a function of edge size. TCB, PBC and DBC stand for traction, periodic and displacement BCs respectively.

three different boundary conditions, in order to compute the homogenized response. The result of those computations is shown in Figure 7.4b, where the macroscopic homogenized Young's modulus is plotted as a function of the sample edge size. It is possible to notice from this graph that with increasing size (from  $l \approx 50$  mm) the three curves tend to collapse in one, leading thus the same value of the homogenized quantity. Whereas for small specimens the apparent stiffness is overestimated by displacement boundary conditions while traction

boundary conditions represent the lower bound. This means that in this case the selected size is too small, while specimens showing an edge size of 50 mm or more are representative and thus suitable for an elastic multi-scale analysis.

**Non-linear behavior**

We report here a brief verification of the RVE existence for our selected mesoscopic model for the non-linear behavior (which we are more interest in). For this investigation three different sample sizes have been considered: squares with an edge size of 25, 50 and 75 mm. The meso-structure of the smaller sample has been generated with a ratio of aggregates corresponding to roughly 40%. While, in order to have a comparable arrangement and grading of the aggregates in the two bigger samples, they geometry has been obtained simply by assembling various times the small unit. This means that the specimen meso-structures of the 50 and 75 mm specimens are constituted by 4 and 9 times respectively the starting cell. The specimens have been subjected to tensile loading in the vertical direction (*i.e.* corner nodes 3 and 4 of Figure 7.2 have been displaced in the vertical direction). To obtain the stress-strain curves, we define the macroscopic stress as the volume average of the microscopic stress tensor  $\mathbf{P}_m$  over the initial RVE volume  $V_0$ .

$$\mathbf{P}_M = \bar{\mathbf{P}}_m = \frac{1}{V_0} \int_{V_0} \mathbf{P}_m dV_0 \tag{7.7}$$

While the macroscopic strain corresponds to the imposed macroscopic gradient  $\mathbf{F}_M$  on the RVE shifted by the identity matrix (and is thus equal to the displacement of the corner nodes divided by the edge length).

$$\boldsymbol{\epsilon}_M = \mathbf{F}_M - \mathbf{I} \tag{7.8}$$

The problem is that the damaging zone of a specimen does not scale with its size, leading to a more brittle behavior with increasing sample size, as one can notice from Figure 7.5a. This can be resolved by plotting the stress in function of the inelastic displacement experienced in the RVE

$$\mathbf{u}_{\text{inelastic}} = \mathbf{u}_4 - \bar{\boldsymbol{\epsilon}}_m \mathbf{X}_4 \tag{7.9}$$

with  $\boldsymbol{\epsilon}_m$  being the volume average of the strains in the bulk elements and the subscript 4 refers to the upper left corner node (and thus represents the imposed displacement over the sample). Indeed, it is possible to notice, from Figure 7.6, that the peak strength is almost independent from the size of the specimen (small size effect since no statistical distribution for  $\sigma_c$  of the interfaces has been introduced to model material's defects). But this is not the case for the strain at peak and at the end of softening. The softening behavior is indeed mainly governed by the main crack that localizes in each sample. Nevertheless, convergence of the response can be achieved by plotting the homogenized stress response as function of the homogenized



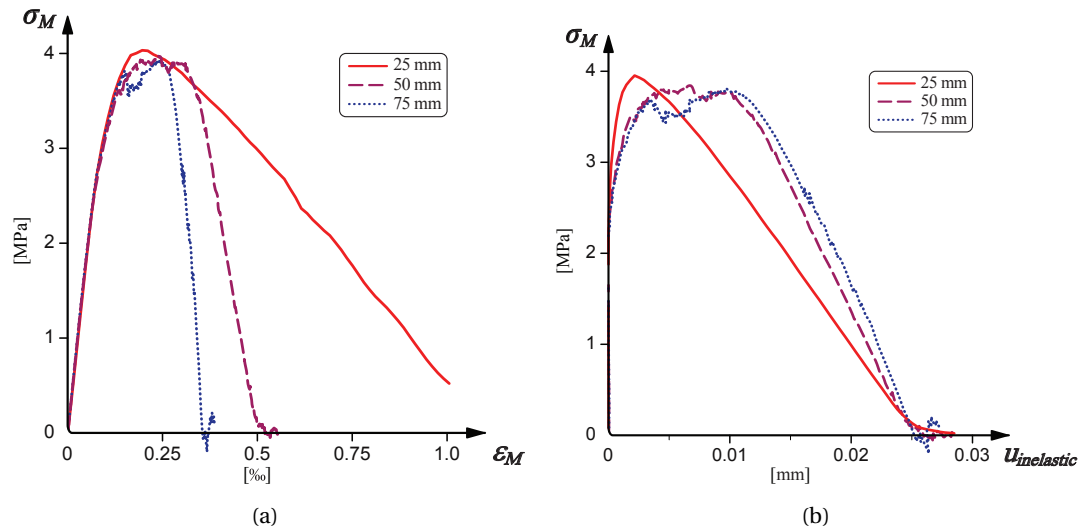


Figure 7.5: (a) stress-strain behavior for different RVE-sizes and (b) homogenized stress-displacement relationship.

inelastic displacement for the two bigger samples, as illustrated in Figure 7.5b. This plot

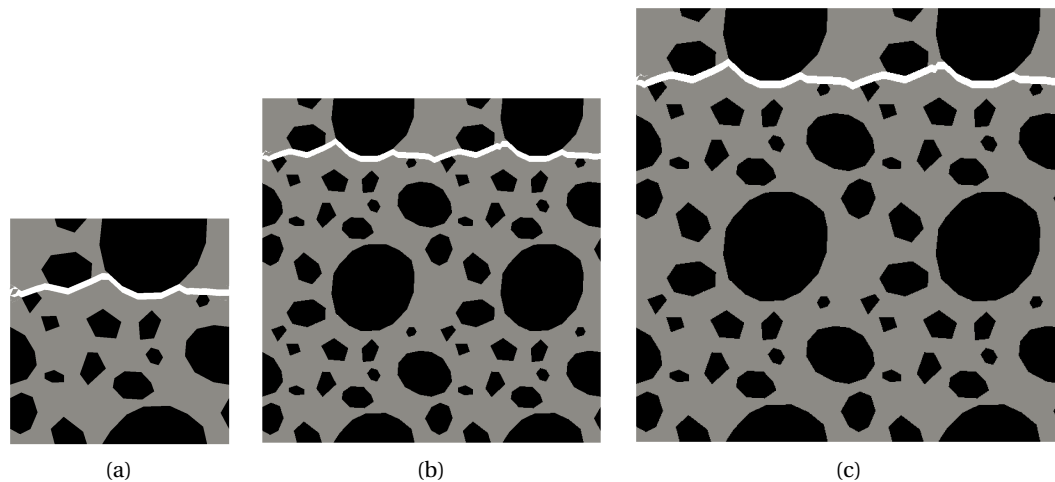


Figure 7.6: Crack path for three RVEs: edge size of (a) 25, (b) 50 and (c) 75 mm (displacement has been magnified by a factor of 20).

shows that the size of 25 mm is clearly too small for the chosen meso-structure, but, the inelastic response that the two bigger samples show is quite similar. Thus, although the two curves do not perfectly match, the curve obtained for the 50 mm specimen can be considered representative (probably with a regular meso-structure a better convergence can be achieved). Thus, it can be concluded that for the presented random meso-structure the existence of a RVE

could be confirmed. The edge size of the RVE has been set for the remainder of the chapter at 50 mm, which corresponds to roughly three times the size of the larger inclusions. Note that in comparison with the elastic behavior a bigger RVE is thus required. Indeed in the un-cracked case larger inclusions have been considered, suggesting the size of the RVE to be equal to 2.5 the size of the largest inclusion. Moreover, in the elastic regime the material is assumed to be non periodic, which should entail a larger RVE size ( [Gitman 07]).

The computed ratio between RVE's edge and coarsest aggregate size reflects what was observed by other authors; for instance experiments carried out on concrete samples by van Mier [van Mier 97] assess this ratio to range between three and five. While simulations performed by Zubelewicz [Zubelewicz 87] show that the fracture front in a notched specimen has a width of about three maximum particle sizes.

### **Aligned periodic boundary conditions**

Classical periodic boundary conditions are suitable for brittle RVEs that are crossed by cracks, whose alignments respect the direction of the periodic enforcements (*i.e.* aligned horizontally or vertically). If this condition is not satisfied, the onset of cracking and development of cracks will be significantly affected. Usually multiple (parallel) cracks will develop in the RVE to face the “unphysical” displacement (unless high strain rates, which cause a diffuse network of cracks, are applied to the RVE) that is imposed on periodic faces because of the misalignment (Fig. 7.9c). One solution to bypass this problem would be to enforce boundary conditions in a weak sense, as proposed in [Mesarovic 05]. In this reference the authors impose minimal kinematic boundary conditions, such that only the desired overall strain is imposed on the RVE. Nevertheless, a new technique of enforcing periodicity to overcome the problems that arise with PBC, has been recently proposed in [Coenen 12]. The authors have developed PBCs, which orient with the evolving localization band in an elasto-plastic voided RVE. Inspired by this new percolation-path aligned boundary conditions, we have adopted in this work boundary conditions that evolve with the development of a crack. During the simulation, before a cluster of cracks propagates, classical PBC are adopted. Indeed at an early stage of loading the sample is uncracked and the position of the discontinuities (that will develop) is not known a priori. Subsequently, when the longest cluster reaches a length of about half of the cell edge, the alignment of the crack direction is estimated having recourse to linear regression analysis (fitted using the least squares approach). At this point, if the determined orientation is not parallel with the sides of the RVE, periodicity of the displacements is enforced on boundaries by rotating the constraint alignment of nodes on opposite faces. The procedure is illustrated with the help of Figure 7.7. Similarly to the aligned case, periodicity is enforced on opposite sides acting on the increment of the displacement at each time step. The reference face, which is intersected by the discontinuity, is considered first (left side of the RVE in Figure 7.7). The increment of the fluctuation field is computed subtracting from the increment of the displacement field ( $\delta \mathbf{u}$ ) the homogeneous part. This can be expressed as follows:

$$\delta \mathbf{w}_L = \frac{\delta \mathbf{u}_4 - \delta \mathbf{u}_1}{h} \mathbf{X} - \mathbf{u}_L \quad (7.10)$$

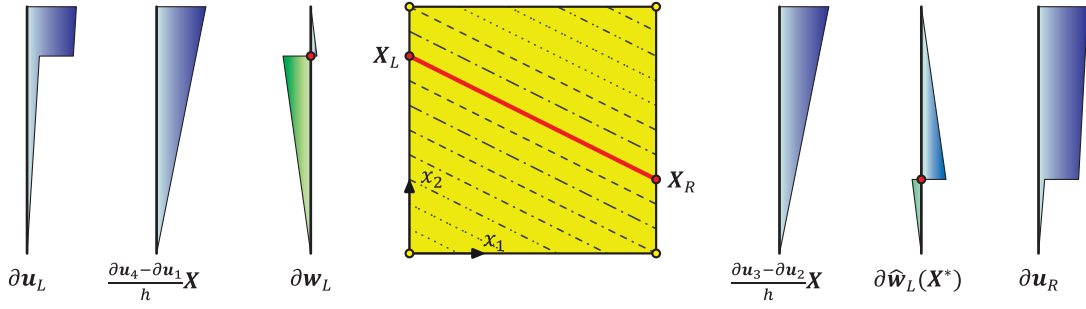


Figure 7.7: Schematic of a RVE crossed by a crack with applied aligned PBC on lateral faces.

The coordinates of the intersection points between the crack with the two faces is indicated with  $\mathbf{X}_L$  and  $\mathbf{X}_R$ . This allows computing the relative coordinates on the periodic face.

$$\mathbf{X}_i^* = \mathbf{X}_i - (\mathbf{X}_R - \mathbf{X}_L) \quad (7.11)$$

With the help of the relative position, the periodic counterparts of each node on the reference face can be determined. Next the increment of the fluctuation field that has to be applied on the periodic face is computed as follows:

$$\delta \mathbf{w}_R = \delta \hat{\mathbf{w}}_L(\mathbf{X}_i^*) = \delta \mathbf{w}_L(\mathbf{X}_i - (\mathbf{X}_R - \mathbf{X}_L)) - \delta \mathbf{w}_L(\mathbf{X}_R - \mathbf{X}_L) \quad (7.12)$$

Note that the reference increment  $\delta \mathbf{w}_L$  needs to be shifted (with the amount  $\delta \mathbf{w}_L(\mathbf{X}_R - \mathbf{X}_L)$ ) in order to vanish at the corner nodes. Consequently, the increment of the displacement on the periodic face is obtained through superposition of the fluctuations field and the “homogeneous” displacement field.

$$\mathbf{u}_R = \frac{\delta \mathbf{u}_3 - \delta \mathbf{u}_2}{h} \mathbf{X} + \delta \mathbf{w}_R \quad (7.13)$$

Finally, it is possible to notice that, if the crack is aligned with the mesh (*i.e.*  $X_{L,2} = X_{R,2}$ ), the aligned PBC reduce to the conventional ones. In addition, since we are using a dynamic framework, a similar procedure has been adopted for the enforcement of the velocities on opposite faces.

### Comparison between classical and aligned PBC

The advantage of the aforementioned procedure, compared to classical PBC, is illustrated ahead of an example. Let us consider the one-dimensional bar illustrated in Figure 7.8. The bar can be discretized using triangular elements with inter-element boundaries oriented with the loading direction (Figure 7.8a) or with diagonal interfaces at an angle of  $30^\circ$  with the vertical axis (Figure 7.8b). In the first case, the TSL of the cohesive elements inserted at the red interface of Figure 7.8a is extracted from a RVE, which is loaded with a traction

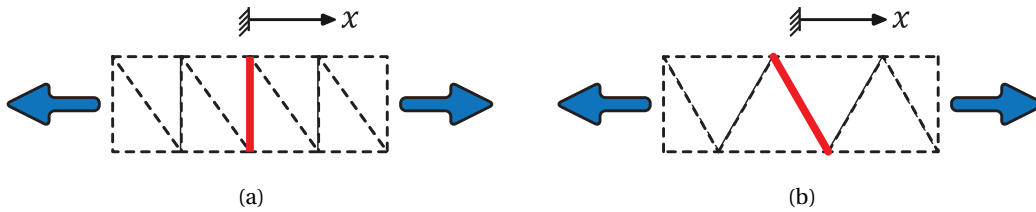


Figure 7.8: One dimensional bar discretized with two different meshes: (a) with inter-element boundaries aligned with the loading direction and (b) with interfaces oriented at an angle of  $30^\circ$ . The thick red line indicates the location of the discontinuity.

parallel to the axis of the cell (thus respecting periodicity). Whereas, if the second mesh is considered (Figure 7.8b), the sample is subjected to a loading which is not aligned with the RVE boundaries.

Consequently, for this example three RVEs will be considered: one that corresponds to the interface of Figure 7.8a and two representative of the diagonal interface depicted in Figure 7.8b. The two RVEs of the second case are subjected to a tensile loading with an angle of  $30^\circ$  between the principal direction and the horizontal axis of the RVE. The difference lies in the direction along which periodicity is imposed. In one case classical PBC have been adopted, whereas in the second case PBC that align with the evolving crack cluster have been selected.

The resulting homogenized TSLs for the three RVE is plotted in Figure 7.10a (homogenized

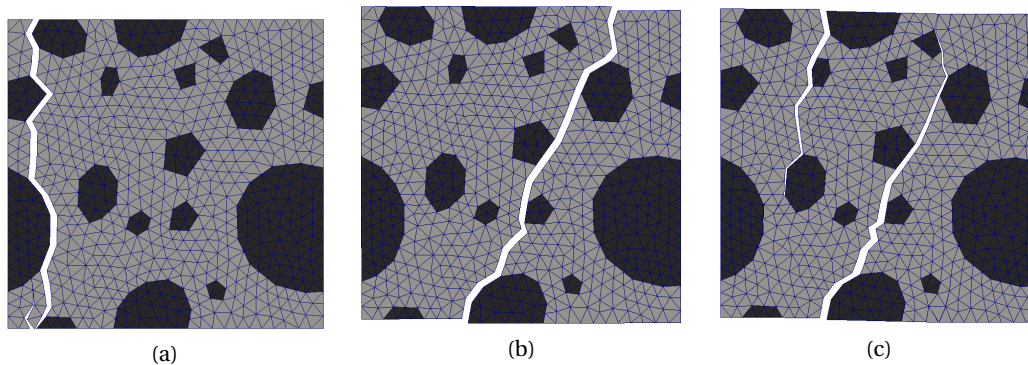


Figure 7.9: Crack path (displacement magnified by a factor of 15) for the RVE: (a) interface aligned with loading direction, (b) interface at  $30^\circ$  with aligned PBC (c) interface at  $30^\circ$  and classical PBC.

traction in  $x$  direction versus inelastic applied opening displacement). It is remarkable that the stress at which softening starts is similar for the three cases considered here. The homogenized response of the RVE loaded in  $x$  is very similar to the one with aligned PBC. Indeed, in both cases, a unique principal crack localizes in the RVE (Figure 7.9a and Figure 7.9b). On the contrary, the response of the RVE without orientation of the PBC, is similar at the beginning, but it

starts to differ during the softening phase due to the misalignment of the imposed periodicity. This also causes the propagation of two big crack clusters that grow perpendicularly to the loading direction as depicted in Figure 7.9c. The alignment of the imposed constraint between faces, causes the crack to have the same propagation point on opposite sides. Therefore, as in the case illustrated here, if the loading direction is not aligned with periodicity, the two propagating cracks cannot then coalesce in the middle. This leads to a TSL law that cannot be considered adequate. Whereas, the agreement between the constitutive response of the samples of Figure 7.9a and Figure 7.9b is pretty good, even if the peak traction is slightly higher for the case with loading aligned with the RVE sides. Therefore, it can be concluded that aligned PBCs not only allow developing correctly cracks within a RVE but also reduce the mesh dependency, that is caused by the macro-scale interface orientation.

As previously mentioned, during the simulation, the growing direction of the main crack is

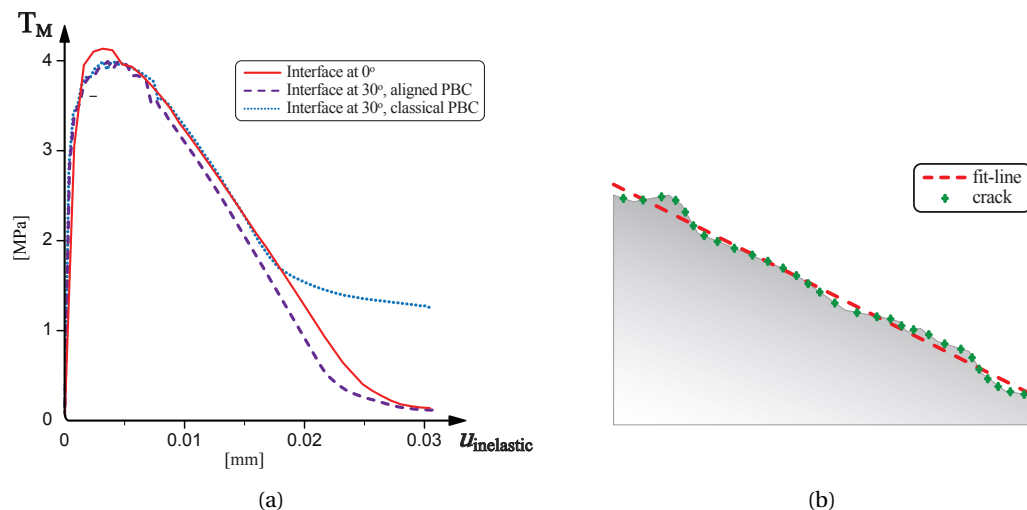


Figure 7.10: (a) Extracted TSL from the three RVEs of Figure 7.9 and (b) computed regression line for the RVE depicted in Figure 7.9b

detected by means of a linear regression analysis. This simple technique minimizes the sum of squared differences between observed values and predicted ones and it is illustrated for the RVE case of Figure 7.9b. The middle node of the inserted cohesive elements is used to track the cluster (green cross in Figure 7.10b). Consequently, the fit can be computed on the basis of those points, giving a straight line (red dashed line in the figure). The obtained equation allows thus computing the intersection between RVE boundaries and the fitted line. The nodes, that are located on the RVE edge in the proximity of the computed point of intersection, are checked for the presence of cohesive elements. The alignment of the periodicity can this way be adjusted, to respect the onset of cracking already present on the faces.

## 7.2 Upscaling

This section illustrates how the coupling from the meso to the macro-scale has been performed. We recall that the problem is how to relate the macroscopic crack with the cells. We adopt the same scheme already adopted in [Verhoosel 10, Nguyen 11]. At the macro-scale, the material behaves linear elastically until crack initiation. I.e. when the inter-element stress exceeds a critical stress value, interface elements are inserted. After nodal disconnection has occurred, the macroscopic traction separation law is extracted from the response of the meso-scale RVE. Therefore meso-scale RVEs are activated each time that a macroscopic discontinuity propagates (on the fly), conversely to conventional homogenization techniques, where integration points are linked from the beginning of the simulation with corresponding micro-scale RVEs. This is congruent with the dynamically inserted cohesive elements.

From the macroscopic boundary value problem, the deformation gradient together with the crack opening displacements and the opening velocity is transferred to the cells. Whenever a crack is initiated the RVE is loaded until the microscopic deformation gradient matches the macroscopic gradient. It should be pointed out that, at this stage of loading, the RVE usually already presents some micro-cracking, but the response is almost elastic and the imposed strain is slightly lower than the strain at which softening (descending branch in the stress-strain curve) starts. This coupling is illustrated in Figure 7.11. The selected coupling causes the homogenized TSL to be initially rigid with some hardening before degradation of the tractions starts Figure 7.11b. Thus, the extracted TSL defines a fracture process zone (FPZ)

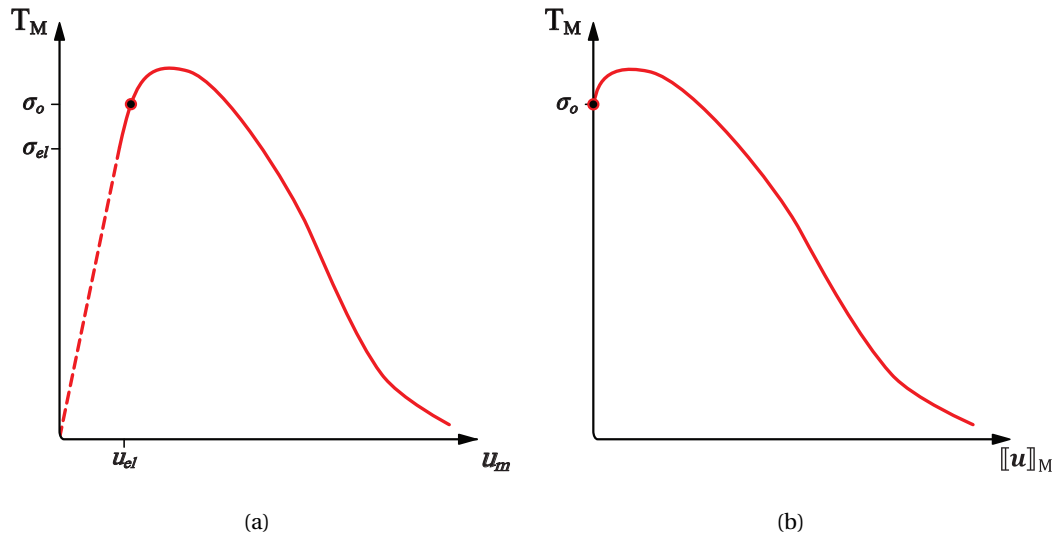


Figure 7.11: Homogenized macroscopic stress (traction) versus (a) meso-scale displacement and (b) homogenized opening displacement of Equation 7.14. The dot ( $\sigma_o$ ) represents the status in the RVE at cohesive insertion.

that includes effects of micro-cracks ahead of the macroscopic crack tip. Indeed, the stress distribution within the FPZ will reach its maximum value before the end of the FPZ, at which the tensile traction will drop to  $\sigma_o$ .

Since after this initial step the RVE is mainly subjected to the macroscopic opening displacement  $\Delta$ , the inelastic displacement on the RVE, representing the sum of all cracks opening within the RVE, needs to be computed in the cell.

$$[[\mathbf{u}]]_{\text{M}} = \mathbf{u}_{4, \text{inelastic}} - \mathbf{u}_{4, \text{inelastic, in}} = \mathbf{u}_4 - \bar{\boldsymbol{\epsilon}}_{\text{m}} \mathbf{X}_4 - (\mathbf{u}_{4, \text{in}} - \bar{\boldsymbol{\epsilon}}_{\text{m, in}} \mathbf{X}_4) \quad (7.14)$$

where  $4$  stands for the index of the  $4^{\text{th}}$  corner node (Figure 7.2). The equation above provides the homogenized opening displacement over the sample. This is defined as the current inelastic displacement in the RVE shifted by the initial amount of applied inelastic displacement. If the RVE is aligned with the normal of the macro-scale cohesive elements (*i.e.*  $\mathbf{e}_2 = \mathbf{N}$ ) the RVE is loaded until

$$[[\mathbf{u}]]_{\text{M}} = \Delta \quad (7.15)$$

Then the homogenized macroscopic traction ( $\mathbf{T}_{\text{M}}$ ) can be computed from the homogenized stress as follows

$$\mathbf{T}_{\text{M}} = \bar{\mathbf{P}}_{\text{m}} \mathbf{x}_2 \quad (7.16)$$

This averaging scheme has been called in [Nguyen 11] as failure averaging technique (moreover, in their publication the authors also provide a proof through an energetic equivalence theorem of the well-posedness of this up scaling procedure). As reported in the previous section, provided that the RVE is selected large enough, this homogenization approach also allows obtaining a TSL which is almost independent of the cell dimensions.

One should note that this procedure applies in both cases of increasing or decreasing values

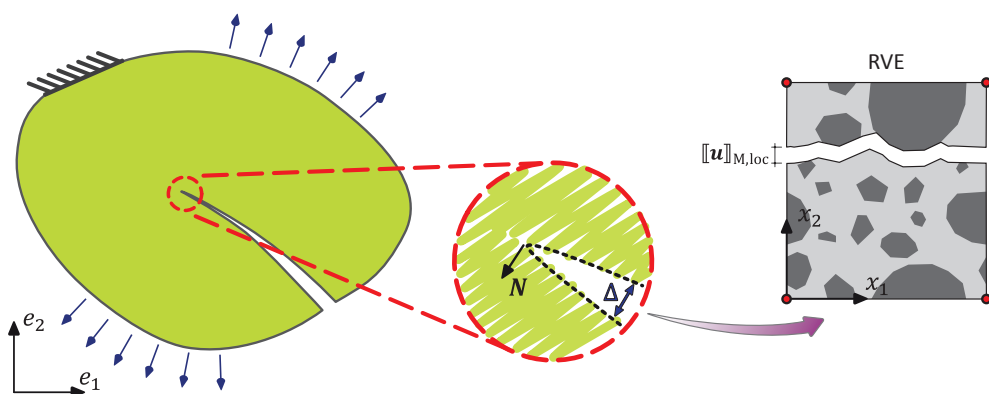


Figure 7.12: Cracked macro-body with crack tip normal  $\mathbf{N}$  and corresponding rotated RVE

of  $\Delta$ , *i.e.* no further treatment is needed to handle unloading and reloading cases. What was

reported so far works if  $N$  corresponds to  $e_2$ . If this is not the case, the geometry of the cell is rotated and it is aligned with the crack direction as illustrated in Figure 7.12. This procedure is applicable since concrete does not have a microstructure with preferential direction of loading (random meso-structure). In order to account for the macro-scale orientation, the quantities of interest need to be transformed from the global (macro-scale) reference system to the local one (RVE) using a rotation matrix. The local displacement jump is computed as follows

$$[[\mathbf{u}]]_{M,loc} = \mathbf{R}\Delta \quad (7.17)$$

where  $\mathbf{R}$  stands for the (2x2) rotation matrix ( $\mathbf{R} = [N_y \ -N_x; N_x \ N_y]$ ). The same procedure applies to the deformation gradient:

$$\mathbf{F}_{M,loc} = \mathbf{R}^T \mathbf{F}_M \mathbf{R} \quad (7.18)$$

and the resulting macroscopic traction

$$\mathbf{T}_M = \mathbf{R}^T \mathbf{T}_{M,loc} \quad (7.19)$$

After the first time step, beyond  $[[\mathbf{u}]]_M$ , the first component of the local deformation gradient is applied to the unit cell. This allows accounting for lateral expansion/shrinkage that occurs at the macro scale and thus recovering a more realistic biaxial stress/strain state within the RVE. This deformation gradient is obtained by averaging the deformation gradients of the closest integration points of the triangular element adjacent to the macro-scale interface element. Moreover, since we are running a dynamic analysis, the opening velocity ( $\dot{\Delta}$ ) of the macro-crack is transferred to the lower scale too. This velocity determines the number of time steps needed to impose the macroscopic quantities and allows accounting for a rate depended response of the material. The initial conditions at the beginning of each meso-scale simulation are formulated according to the imposed displacement and velocity.

$$\mathbf{v}_i = \dot{F} \frac{\mathbf{X}_i}{h} \quad (7.20)$$

respectively

$$\mathbf{v}_i = \dot{\Delta} \frac{\Delta}{\|\Delta\|} \frac{\mathbf{X}_i}{h} \quad (7.21)$$

This conditions should avoid important stress wave propagation and an early fracture near the boundaries [Miller 99] at early stage of loading. Both Equations 7.20 and 7.21 result in a linear gradient of velocities according to the reference position of each node. It is possible to notice that when the specimen has undergone large deformation they could be modified to account for the influence of a discontinuity of the velocity field.



### 7.2.1 Computational aspects

The presented multi-scale procedure is solved performing an explicit dynamics analysis both at the macro and RVE scale. Therefore no computation of the tangent matrix is needed. The meso-scale RVE are initiated whenever a new crack segment is inserted at the macro-scale. At each macroscopic time step, an analysis with several time steps needs to be performed in every active RVE. We manage the farming procedure with the remote procedure call (RPC) based client-agent-server system Gridsolve [Dongarra 06], which is a library that supports C, FORTRAN, Matlab, and Mathematica. One master process (client) solves the macro-scale boundary problem and performs GridRPC asynchronous calls to the servers through the help of an agent, which manages the requests and assigns them to an appropriate server. The client also collects back the results that are returned from the servers (each server runs sequentially meso-scale simulations). To have a computationally efficient algorithm, which minimizes waiting time, communication is kept as low as possible. The amount of transferred data is minimized (every RVE-mesh is reconstructed starting from the original mesh on the basis of few transferred information) and a call for a specific meso-scale RVE is performed only if the macroscopic opening displacement has changed perceptibly, compared to the value computed at the previous time step. The entire procedure is illustrated in the Algorithm 1.

---

**Algorithm 1** Multi-scale algorithm for computational homogenization in explicit dynamics

---

```

1: while  $t \leq \text{simulation time}$  do
2:   Apply displacement boundary conditions
3:   Predictor:  $\mathbf{u}(t_i)$ 
4:   Compute  $\Delta(t_i)$ 
5:   for all number of active RVEs do
6:     Call SOLVERVE
6:   end for
7:   Assemble residual:  $\mathbf{r}(t_i)$ 
8:   Check cohesive insertion
9:   Corrector:  $\mathbf{a}(t_i)$  and  $\mathbf{v}(t_i)$ 
10: end while
1: function SOLVERVE ▷
2:   Compute local quantities and restore status of RVE
3:   repeat
4:     Apply displacement on corner nodes
5:     Solve RVE problem
6:   until  $\mathbf{u}_{m, \text{in}} \approx \llbracket \mathbf{u} \rrbracket_{M, \text{loc}}$ 
7:   Compute macro-traction:  $\mathbf{R}^T \mathbf{T}_{M, \text{loc}}$ 
8:   return  $\mathbf{T}_M$ 
9: end function

```

---

### 7.3 Numerical results

As already stated in the introduction section, we have selected two problems to demonstrate the performance of the presented multi-scale model. The first application consists in a Double Cantilever Beam (DCB), which entails the propagation of a macroscopic crack under mode I. The purpose of the first virtual experiment is to validate the applicability of the proposed method by comparing the recorded multi-scale response with the result of a DNS. While, the second application involves shear displacement between the crack faces. To this end we have reproduced a push-off test.

#### 7.3.1 DCB specimen

We perform here a validation test on a concrete DCB specimen. The validation is provided through comparison between the FE<sup>2</sup> solution and the recorded response of a DNS. The chosen specimen geometry and the boundary conditions for this test are illustrated in Figure 7.13. As depicted in the figure, the specimen is 1 m wide and 0.8 m high with a notch of 0.4 m. In

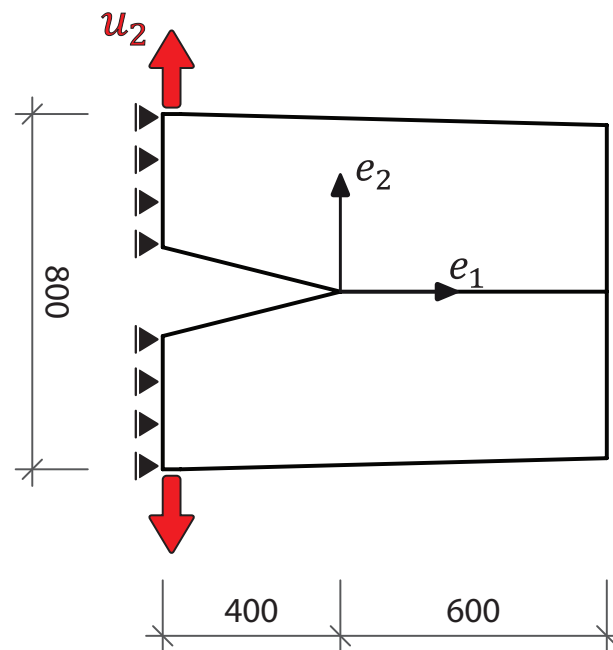


Figure 7.13: Geometry (all units in mm) and boundary conditions of the DCB test

both virtual experiments the samples have been loaded under displacement control. To avoid a too large computational effort during the DNS test, the DCB specimen (depicted in Figure 7.14b) has not been completely resolved at the fine-scale. Indeed a meso-scale band, composed by repeated adjacent RVE geometries, accounts for the heterogeneous composition of the material. This fine level of representation is located where the macroscopic crack is

expected to propagate. Since only few micro-cracks should nucleate outside from this zone, the surrounding material is considered to be homogeneous and to behave linear elastically. The material properties of this region correspond to the uncracked properties of an RVE: Young's modulus 35 GPa and Poisson's ratio 0.2. Whereas, the material in the meso-scale zone accounts for the fracturing process and behaves thus exactly following the constitutive model described in Section 7.1.2.

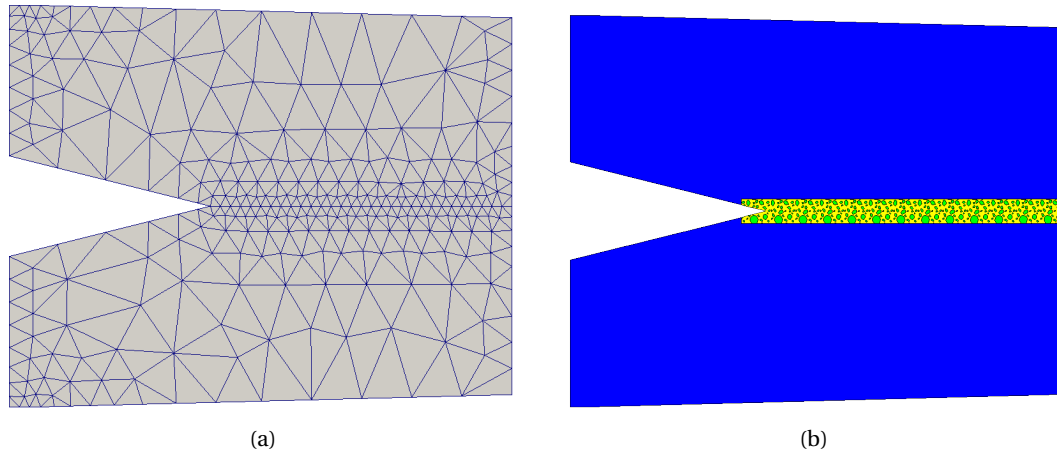


Figure 7.14: DCB specimen for the virtual experiments: (a) Macroscopic mesh for the multi-scale simulation and (b) adopted geometry for the direct numerical simulation.

The corresponding macro-scale mesh for the multi-scale simulations (Figure 7.14) has to be chosen according to the cohesive zone length ( $l_z$ ) resulting from the RVEs response (10 cm). We recall that this length (see Equation 3.39) has to be considered for the choice of the mesh. In order to resolve the decohesion process, the cohesive zone length must be discretized with a few cohesive elements (typically around 3-5). Therefore, according to  $l_z$  in the zone where crack propagation occurs the mesh size of the coarse scale has been fixed to 2 cm. The macroscopic mesh is composed by quadratic triangular elements, which entails that each cohesive element has three quadrature points. As a result three RVEs are assigned to every dynamically inserted interface element. This together with the necessary refinement's degree of the macroscopic mesh, implies that the horizontal central line along which a crack is expected to propagate is represented by more than 12 adjacent unit meso-structures of the DNS.

During the virtual experiments the upper and lower ends of the DCB have been displaced vertically (Figure 7.13) in  $+e_2$  and  $-e_2$  direction respectively. The imposed vertical velocity has been increased gradually up to a value of 0.025 m/s. Thereafter its value has been kept constant during the rest of the simulation, in order to avoid rate-effects and thus make more realistic the assumption of a single propagating horizontal macroscopic crack (with little amount of nucleating micro-cracks ahead of the crack tip).

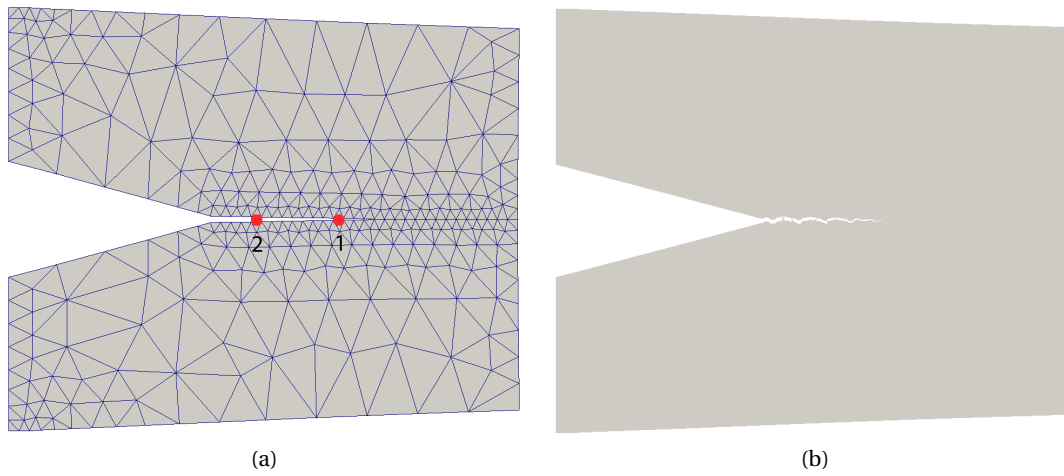


Figure 7.15: Developed crack path in the DCB specimen (displacement has been magnified by a factor of 80). Comparison between (a) the multi-scale cohesive solution and (b) the DNS.

The evolution of the crack with the approaches is illustrated in Figure 7.15. The image depicts the deformed configuration after the peak strength has been reached. Note that the two images do not exactly depict the same time-frame, indeed the specimen of Figure 7.15a shows a slightly longer crack.

In addition, Figure 7.16 illustrates the crack path in two different RVEs. The first one (depicted

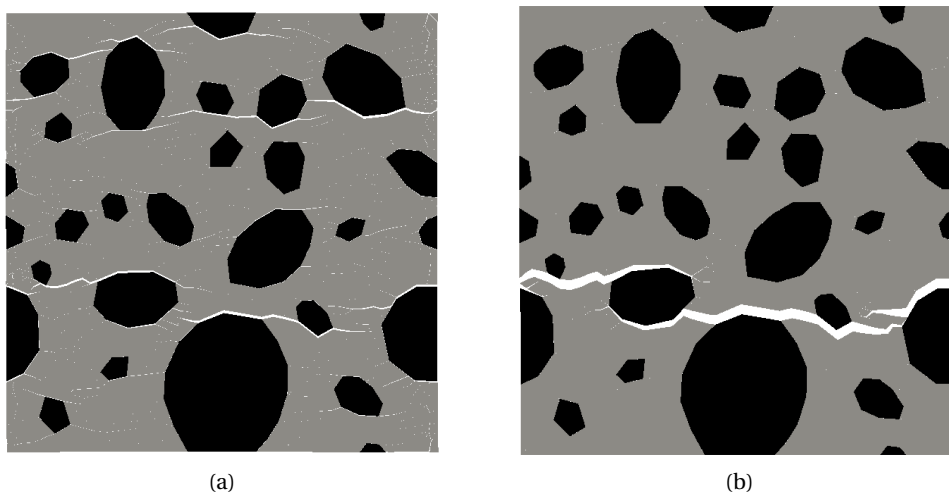


Figure 7.16: Deformed configuration (displacements have been magnified by a factor of 15) of two RVEs corresponding to two different integration points located: (a) near the crack tip (circle 1 in Figure 7.15a) and (b) more distant (circle 2 in Figure 7.15a) respectively.

in Figure 7.16a) corresponds to a coarse scale integration point near the crack tip (circle 1 in Figure 7.15a) and shows a few micro-cracks in the matrix and at the ITZs. While the second one, which represents a Gauss point more far off the crack tip (circle 2 in Figure 7.15a), has already undergone a bigger deformation (*i.e.* imposition of a larger opening displacement), which entails the localization of a single crack within the RVE (Figure 7.16b).

The comparison of the recorded load-displacement curves is illustrated in Figure 7.17. From this graph one can notice that the multi-scale model can successfully reproduce the behavior of the DNS. Although the two curves do not match exactly (and an exact match cannot be expected from a coarse multi-scale simulation), there is a good agreement between the two responses, since the peak strength and the corresponding displacement at peak are similar for the two solution techniques.

Finally, the  $FE^2$  analysis, ran on a cluster node with 10 CPUs, allowed to reduce the computa-

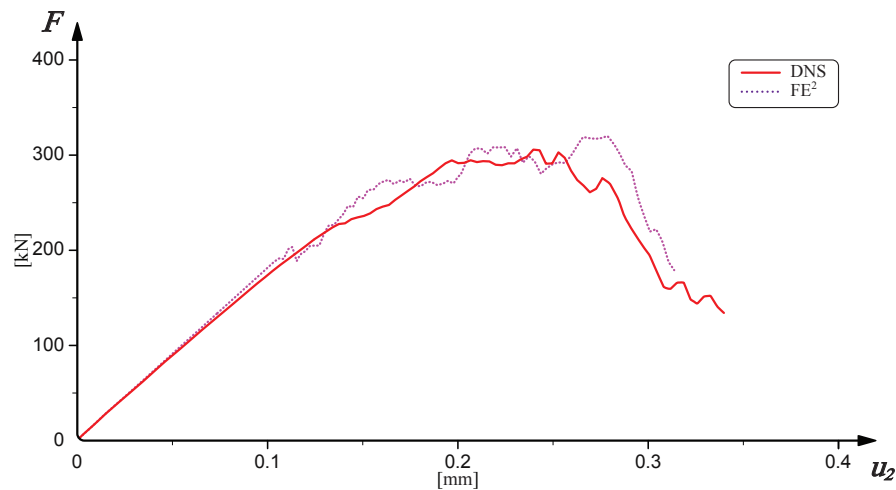


Figure 7.17: Comparison of the vertical force-displacement relationships for the multi-scale scheme and the DNS

tional time of about 4.5 times.

### 7.3.2 Push-off application

The aim of the second application is to demonstrate the applicability of the proposed method to a common test in civil engineering, which is performed to investigate the mechanisms related to shear transfer through cracks. For this purpose we have chosen to carry out a multi-scale simulation of a push-off test. This problem involves frictional contact at the scale of the inclusions through aggregate interlock. Because of to the large displacement experienced by the crack surfaces, no comparison with a DNS has been performed. While, preliminary results have been compared with experimental recorded values.

The geometry of the specimen is illustrated in Figure 7.18a. For this virtual experiment we have

chosen to reproduce one test unit of the experimental test program conducted by Sagaseta *et al.* [Sagaseta 11].

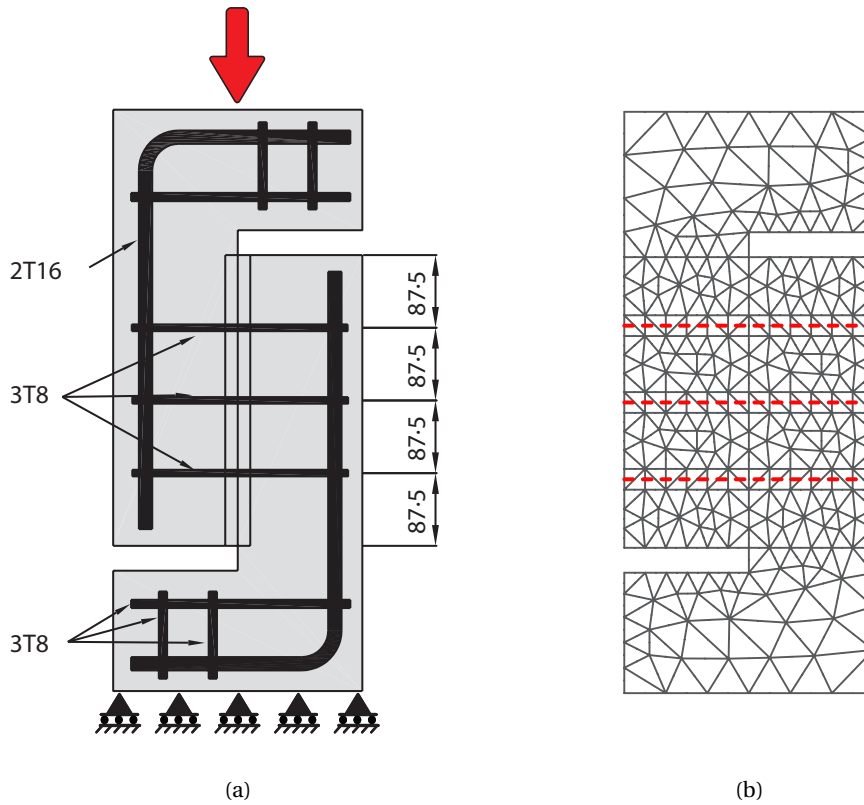


Figure 7.18: (a) Geometry of the tested unit by Sagaseta *et al.* [Sagaseta 11] with diameter of reinforcement bars (all dimensions in mm). (b) Corresponding coarse-scale mesh for the multi-scale analysis (the red dashed lines represent stirrups that have been modeled with bar elements).

The sample is composed by two reinforced concrete blocks with an “L” shape. Experimentally the specimen is pre-cracked in tension before the shear is introduced (the upper block is moved in vertical direction toward the lower one, which is supported on a sliding support). Horizontal stirrups constrain the widening of the specimen during the test. The relative displacement experienced by the two blocks causes indeed the dilatation of the vertical macro-crack between them, since the inclusions at the crack surfaces slide over each other. As a consequence compressive normal forces are generated because of the presence of the stirrups, while the resulting shear stiffness is due primarily to the mechanism of aggregate interlock. The mesh used for the FE<sup>2</sup> simulation is depicted in Figure 7.18b. Since the sample is made of reinforced concrete, the macro-scale problem is considered to be homogeneous with exception of bar elements simulating the steel-reinforcement. However, we do not model the entire network of reinforcement bars, because crack propagation is allowed only at the

interface between the two blocks. Therefore, only the stirrups, which cause the confinement of the macroscopic crack, have been modeled explicitly (note that a perfect bond between concrete and steel has been assumed). In addition, since experimentally the sample is pre-cracked, for the simulation we have adopted RVEs with an initial vertical crack, which crosses the RVEs.

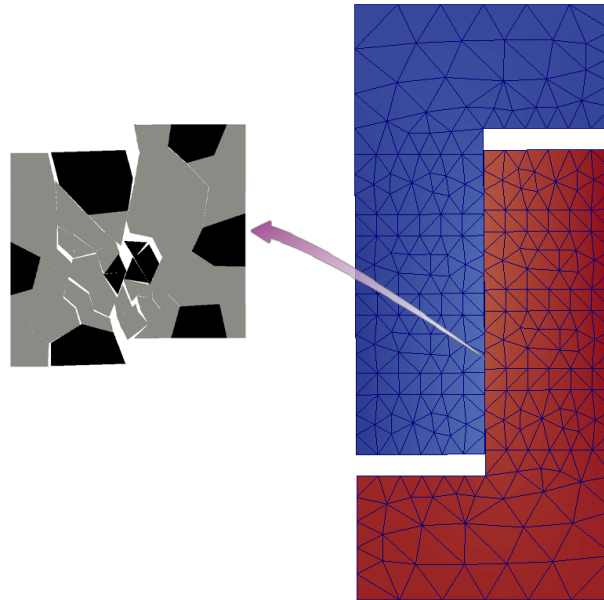


Figure 7.19: Macroscopic deformed mesh configuration and shearing in a RVE located on the vertical macroscopic crack.

The deformed mesh configuration of the sample is depicted in Figure 7.19. Moreover, the same figure shows the deformation experienced by a RVE located on the macroscopic crack. One notices that the inelastic displacement localizes in a main vertical crack. (Note that for this application a smaller RVE has been selected, in order to reduce the computational cost. However, since the RVE is pre-cracked the computed TSL originates primarily from shearing of the cracks.)

The numerically computed and the experimentally recorded shear stress-displacement curves are compared in Figure 7.20. For the comparison, experimental results obtained with concrete inclusions made of marine dredged gravel (cracks propagate around aggregates) have been selected.

From the graph one can remark that the model can reproduce some features of the experimental behavior. After an initial peak, the computed response stabilizes indeed around a fixed value during the pure frictional regime. However, the resultant shear stiffness (as well as the initial stiffness) is lower than the experimental one. This might be traced back to the chosen simplified modeling of the stirrups (we do not consider dowel action) and to the fact that we are in a two-dimensional settings. In addition, the use of pre-cracked RVEs in conjunction

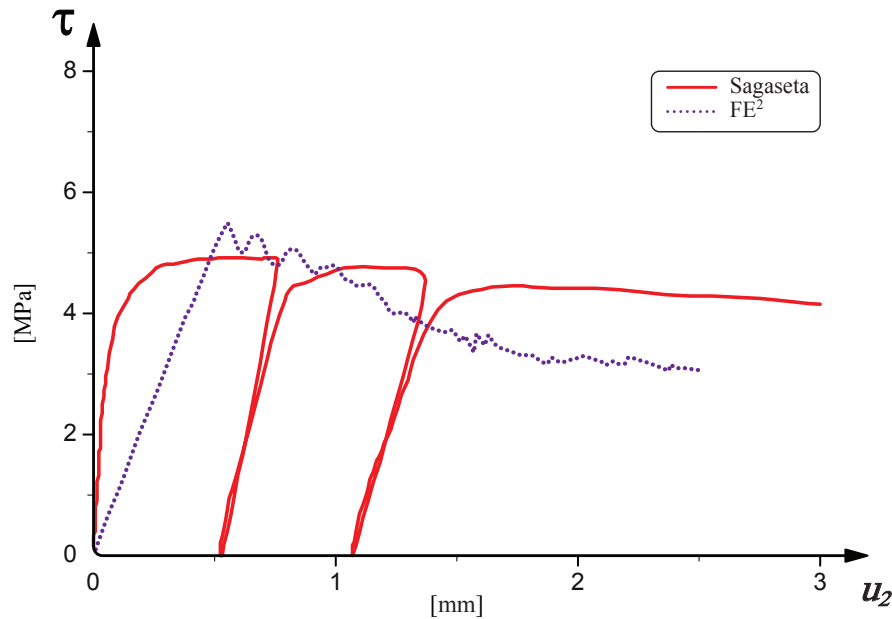


Figure 7.20: Comparison of the shear stress-displacement curves for the push-off test between the  $FE^2$  analysis (dotted line) and the experimental results (continuous red line) of Segaseta [Segaseta 11].

with the bar elements causes some initial slip within the RVEs at early stage of loading, leading to a lower initial stiffness in the force-displacement relationship.

### 7.3.3 Perspectives: application to a reinforced concrete beam

The aim of the work presented until here has been to develop the fundamental computational aspects to simulate macroscopic material's behavior explicitly by modeling the interactions occurring at the fine scale. This goal has been achieved for the applications presented in the previous subsection. However, further investigations should allow the virtual testing of more complicated engineering's problem, such as structural reinforced components. With respect to the two selected applications, such a problem would indeed entail a more complicated propagation of cracks under mode mixity (multiple cracks) as well as a higher number of degrees of freedom to be modeled.

A possible application of interest, depicted in Figure 7.21, is represented by shear failure of a reinforced beam. This failure mode is characterized by the growth and formation of a macroscopic well-defined crack that determines the ultimate load of the member. This problem is particularly interesting because it involves, besides crack opening, shearing of the cracked surfaces (similarly to the push-off test).

In the last decades, there has been a substantial research in understanding such failure events. Semi-analytical models have been developed to describe brittle shear rupture of structural



components (e.g. [Muttoni 08, Muttoni 12]). Therefore, it would be extremely interesting to perform a multi-scale analysis of a specimen involving this geometry and to perform a comparison with the analytical prediction especially for different aggregates contents. Note that a comparison with a DNS would not be possible in this case due to the large system size.

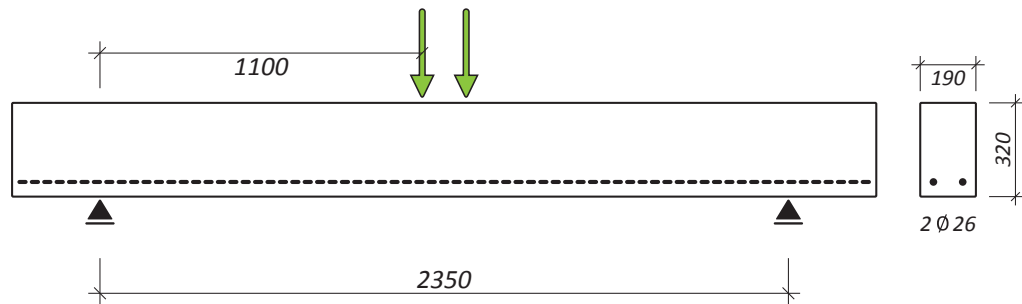


Figure 7.21: A possible future application of interest. Beam geometry of the tested unit by [Leonhardt 62] with boundary conditions (all dimensions in mm).

## 7.4 Conclusions

In this chapter, a multi-scale approach to model cohesive failure for the analysis of concrete has been proposed. The model has been implemented in a displacement-driven 2D FE<sup>2</sup> framework in explicit dynamics. Computational homogenization is applied only for the integration points belonging to macroscopic interface elements. Consequently, the macroscopic debonding behavior is extracted from mesoscopic RVE simulations, in which concrete is represented as a biphasic material made of aggregates embedded in a cement paste matrix. In addition, the fine scale enables an explicit representation of crack propagation. Thus, the homogenized traction separation law depends on damage mechanisms that are governed by the geometry of the meso-structure.

Since propagation of cracks under mode mixity generally entails a misalignment between the RVE boundaries and the development of the localized crack, evolving periodic boundary conditions (which follow the crack orientation) have been adopted. This also reduces the fine scale dependence on coarse scale orientation of the interface elements leading to more realistic failure patterns within the corresponding RVEs.

In order to show the applicability of the proposed computational approach to engineering's problems, the model has been validated by comparison with a reference DNS on a double cantilever beam. Whereas, for the second application a push-off test, which involves shearing between the crack-faces, has been selected.

The numerical results demonstrate the capability of the model to extract the macroscopic fracture behavior from physical mechanisms occurring at the fine scale and thus to predict the structural response of the tested unit.



## 8 Conclusions and Outlook

In the following we summarize the main conclusions that have been reached during this research work. Finally, we give possible directions for future research and development.

### 8.1 Summary and conclusions

In this thesis we have sought to grasp the physics underlying dynamic failure of concrete, a widely used (quasi-) brittle material. This material, which is often modeled as homogeneous at the macro scale, shows a heterogeneous composition at a lower level of observation. Since the macroscopic failure process is strictly related to the material's meso-structure, a meso-mechanical computational approach has been first exploited in this research work. The advantage of this level of observation is that it allows for the representation of the most important concrete constituents (e.g. aggregates and cement paste) as well as to provide information about the spatial arrangement of the phases. This facilitates the physical identification of the material parameters of the model and of the mechanisms (interaction between matrix and inclusions) that characterize its constitutive behavior. Indeed, when subjected to sufficient loading, the material undergoes a non-linear failure process. This involves the opening of local micro-cracks, which propagate, coalesce and subsequently might enter into contact. During the fracturing process, the material phases (bulk elements) are considered to behave elastically, while cracking is explicitly modeled by to dynamically-inserted cohesive elements. This computational framework has been first applied to analyze the dynamic tensile failure of concrete specimens. We focused our investigation on the influence of aggregate properties (internal ordering, size distribution and toughness) on peak strength and dissipated fracture energy.

We showed that with a rate independent constitutive law, used to model the interfacial behavior, the model is able to capture some of the increase in peak strength and strain at failure with increasing rate of loading. Indeed, the increase in strength with the strain rate resides in a more diffuse micro-cracking and is related to the intrinsic characteristic opening time of the cohesive law. This mechanism leads to an increase in the amount of dissipated fracture energy. Nevertheless, our results suggested that the full extent of the high-rate strengthening

of concrete observed experimentally cannot be captured with rate independent constitutive laws.

Therefore, for our meso-mechanical approach, we could not discard the combination of inertial with material rate hardening mechanisms. The introduction of a rate dependent cohesive law increases the difference of the computed peak strength between low and high strain rates, leading to a closer match with experiments. On the other hand, the rate-independent computed amount of dissipated energy seems to be closer to the one recorded experimentally. This means that the tensile strength increase is, probably, mostly due to a material effect (moisture, visco-elasticity, ...) while the dissipated fracture energy, observed in the post-peak part, is mainly due to the increase of the number of micro-cracks with the loading rate.

We have considered different material properties for the concrete constituents. For instance a different toughness of the inclusions affects also the peak strength as well as the dissipated fracture energy. However, simulations carried out for two different types of aggregates (soft and hard) concluded that the peak strength is considerably sensitive to the toughness of the inclusions mostly at low strain rates (different crack paths). While, at high strain rates, inertial forces dominate the overall behavior. Propagation of cracks in the inclusions occurs only after peak strength is reached.

Besides this, the influence of the meso-structure geometry has been quantified too. In general, specimens with heterogeneities following the same grading curve but with a different spatial arrangement, show a difference mostly in their post-peak response. Comparisons between specimens with different alignments of the inclusions revealed that a uniform meso-structure can rise or lower the peak strength depending on the orientations of the inclusions. While, a random distribution increases the probability to have weak zones (interfaces between aggregates and matrix are closer), which reduces the peak strength.

In addition, our results showed that, having two concrete materials with same aggregate volume ratio, the one with smaller inclusions will exhibit a larger strength at low strain rate in case of soft aggregates. Large aggregates facilitate the propagation of cracks within inclusions. This involves a larger area of broken aggregates, which is linked with a lower strength.

In order to be able to model failure of specimens subjected to compressive loading, the cohesive law has been modified to account for path dependent behavior and, therefore, to introduce a mode-dependent fracture energy. To this end a novel explicit traction separation law, based on the popular law proposed by Camacho and Ortiz [Camacho 96], has been introduced into the model. Besides this, to account for the possible interactions between generated rough surfaces during cracking, a contact algorithm that enforces the impenetrability condition has been included too. The formulation proposed in [Cirak 05] has been adopted. We resorted to the classical law of unilateral contact and Coulomb friction. The contact algorithm has been coupled together with the cohesive approach in order to have a continuous transition from crack nucleation to the pure frictional state.

To demonstrate the capability of the proposed approach to provide accurate results, the model has been validated firstly by applying it to two benchmark tests in masonry engineering: a shear test on a wallette and on a wall. The calibration, by comparison with experimental

values, has been carried out for the first application. The calibrated values, of the interfacial transition zone, have been then used to reproduce a test on a masonry wall loaded in compression and shear. The numerical results have shown the capability of the model to represent the physical process involved during cracking in compression and to give a good prediction of the structural response of the tested units.

Afterwards, the developed framework has been applied to the investigation of dynamic compressive failure of meso-scale concrete samples. Simulations in compressive regime with increasing rate of loading showed that the model is able to capture the increase in strength and strain at failure. This rise resides in a more diffuse micro-cracking (as already observed for tensile loading) and is thereby bounded with a higher dissipation of fracture energy as well as the energy dissipated through friction. A comparison, between our simulation results and experimental literature, indicates indeed that inertial forces alone, in case of compressive loading, are sufficient to explain the increase in strength with increasing loading rate conversely to what observed for tensile-loading (where material hardening should be added in order to achieve a higher strengthening).

Specimens subjected to lateral confinement in compression exhibit an increase in peak strength and strain at maximum stress with increasing confining pressure. However, the rise in strength is lower than experimental reported values. It has been observed that an increase in the lateral pressure produces delays in the formation of the first crack cluster and in micro-cracks coalescence. Dissipation of energy through fracture and friction is also an increasing function of the applied confinement. The model also showed the importance of capturing frictional mechanisms, which appear to dissipate a raising amount of frictional energy with increasing strain and applied pressure (the work done by friction is on the same range of magnitude as the energy dissipated through crack opening under compressive loading).

It is however important to emphasize that our model needs further improvement to capture experiments better. In particular, the ductility of the specimen is less affected by the confining pressure than the one measured experimentally and the post-peak behavior remains more brittle. This could perhaps be linked to a yet insufficient increase in the amount of dissipated frictional energy or to the lack of other physical phenomena in the model (such as compaction). Moreover, the limited chosen 2D setting cannot capture the complexity of 3D micro-cracking. The cracks density is underestimated since it is easier to reach percolation in 2D than in 3D.

Finally, the meso-mechanical model has been used in simulations across scales to extract the constitutive behavior avoiding the use of phenomenological macroscopic modeling. In the developed multi-scale framework, the fracture process that undergoes the coarse scale, is strictly linked with micro-cracking and localization experienced at the fine scale. Computational homogenization was indeed applied only for the integration points belonging to macroscopic interface elements. Consequently, the macroscopic debonding behavior was extracted from the mesoscopic behavior. Thus, the homogenized traction separation law depends on damaging mechanisms that are governed by the geometry of the meso-structure.

Since propagation of cracks under mode mixity generally entails a misalignment between the RVE boundaries and the development of the localized crack, evolving periodic boundary conditions (which follow the crack orientation) have been adopted. This also reduces the fine scale dependence on coarse scale orientation of the interface elements, leading to more realistic failure patterns within the corresponding RVEs.

Two applications to show the applicability of the proposed computational approach to macroscopic problems have been selected. The model has been first validated by comparison with a reference direct numerical simulation on a double cantilever beam. Whereas, as second application we have reproduced a push-off test, which involves shear transfer through cracks. The numerical results have shown the capability, of the model, to extract the macroscopic fracture behavior from physical mechanism occurring at the fine scale and, thus, to predict the structural response of the tested unit.

### 8.2 Perspectives

Several aspects, tackled in this thesis, could offer space for further, deeper investigations. One of the most significant possible development would be to extend the proposed computational framework to three dimensions. In particular, the meso-scale model would benefit from this extension. Indeed, as demonstrated by simulations under compressive regime, the proposed two-dimensional model narrows the chances to capture the full development of crack localization. In 2D the density of the cracks is underestimated since it is easier to reach percolation than in 3D. It would be interesting thus to quantify the influence of the third dimension on the simulation results. However, as already observed by other researchers, this extension is bounded with a higher computational cost (if the meso-structure is to be analyzed with the same level of accuracy). Therefore, simulations would most probably require the use of parallel computing.

Besides this, the third dimension might lead us to reconsider the solidity of the assumption of the chosen transition from debonding to pure frictional sliding. To this end, it would be appealing to have recourse to experimental techniques to better characterize the strength of the bonds and the development of cracks at the fine level. For instance X-ray computed tomography, which is a non-destructive technique for gathering information about the internal composition of opaque samples (through X-rays that cross the material in several directions producing a set of digital images), would allow analyzing the particles geometry (surface roughness) and better delineating the ITZs within concrete specimens. In addition, applying this testing technique to damaged samples, would enable to compare the development of micro cracks with subsequent localization between experimental and virtual testing.

Another opportunity to increase the accuracy of the modeling, can be offered by the comparison with experimental measurements of the bond-strength of the interface between cement paste and inclusions. It is widely accepted, indeed, that the interface strength is a very important factor, which is linked with the formation of micro-cracks patterns between aggregates and matrix. The clarification of this damage process can thus provide a better knowledge

about the evolution of the internal structure in concrete during loading. A suitable method, which can be used to deduce the micro-strength of this transition zone, is represented by indentation tests.

Moreover, a statistical distribution of the interface-strengths between constituents could be added into the model in order to represent material defects and thus to get a more pronounced size effect when the specimen dimensions are varied.

There would be also space to further improve some other computational aspects of the meso-model. For instance, the selected contact algorithm, which allows us to handle frictional contact in an explicit dynamic setting through projection of the penetrating nodes, causes an increase in the potential energy of the system. It would be interesting to develop a method that minimizes the amount of injected energy into the system.

Another interesting aspect could be the extension of the model to multi-physics. Including chemical reaction and heat transfer would give, indeed, access to a wider range of applicability for the model. Time dependent phenomena such as creep, shrinkage and aging could be so incorporated in the proposed framework. The effect caused by those time dependent processes in concrete structures is indeed important, since it affects not only the deformations but also the stress field and the strength properties of the material itself. Consequently, the stress redistribution and lower resistance should be considered to make a better assessment of the load carrying capacity of a structural member.

The meso-scale formulation can thus be enriched in order to include various additional capabilities. This improvement would also require the transfer of more information across scales, leading to a parallel enhancement of the up scaling procedure and, subsequently, to the coarse scale behavior too. On the other hand, the adopted concurrent multi-scale scheme also offers plenty of possibilities. The chosen up scaling procedure might be combined with other discretization techniques to enrich the macroscopic displacements field (such as XFEM). This could probably further reduce the coarse-scale crack orientation dependence on the chosen macroscopic mesh.

Space for fine tuning is offered by the calibration of the model and careful investigation of the dynamic effects within the multi-scale framework. This could lead to a possible accurate investigation of virtual testing series on a wide range of sample sizes, assessing the influence of the specimens dimensions on peak strength and brittleness (size effect).

Additional improvement to the model could include the extension to more complicated failure modes and computationally expensive cases. The effect of steel reinforcement on cracks propagation and structural resistance could be assessed. Moreover, the usually assumed perfect bond between concrete and steel-reinforcement could be replaced by a more accurate modeling, which considers the stress field that develops in proximity of the steel-concrete interface. This could be achieved with the help of a multi-scale representation of the steel-bars, which could lead to explicitly model the movement between the reinforcement and the surrounding concrete that can originate in case of severe loading.

To conclude, all the improvements made to the model are aimed to raise the accuracy in predicting the material's behavior. Moreover, this mechanical-framework would certainly

## **Chapter 8. Conclusions and Outlook**

---

benefit of further developments to extend it to model failure of other brittle materials, whose behaviors are clearly influenced by their micro-structural composition. We indeed believe that the understandings, gained through a computer analysis, should be included already during the design phase of a structure. In addition, computational modeling could help engineers, during the conception and development of new advanced structural materials, by offering a virtual testing platform.



# Bibliography

- [Acary 06] V. Acary & Y. Monerie. *Nonsmooth fracture dynamics using a cohesive zone model*. Rapport technique 6032, INRIA, 2006.
- [Alart 91] P. Alart & A. Curnier. *A mixed formulation for frictional contact problems prone to Newton like solution methods*. Computer Methods in Applied Mechanics and Engineering, vol. 92, no. 3, pages 353–375, 1991.
- [Alfano 06] G. Alfano & E. Sacco. *Combining interface damage and friction in a cohesive-zone model*. International Journal for Numerical Methods in Engineering, vol. 68, no. 5, pages 542–582, 2006.
- [Aquino 95] M. J. Aquino, Z. Li & S. P. Shah. *Mechanical properties of the aggregate and cement interface*. Advanced Cement Based Materials, vol. 2, no. 6, pages 211–223, 1995.
- [Barenblatt 62] G. I. Barenblatt. *The mathematical theory of equilibrium of cracks in brittle fracture*. Advances in Applied Mechanics, vol. 7, pages 55–129, 1962.
- [Bathe 96] K.J. Bathe. Finite element procedures. Prentice Hall: Upper Saddle River, NJ, 1996.
- [Bažant 84] Z.P. Bažant. *Size effect in Blunt Fracture: Concrete, Rock, Metal*. Journal of Engineering Mechanics, ASCE, vol. 110, pages 518–535, 1984.
- [Bažant 97] Z.P. Bažant & Y.N. Li. *Cohesive Crack with Rate-Dependent Opening and Viscoelasticity: I. Mathematical Model and Scaling*. International Journal of Fracture, vol. 86, pages 247–265, 1997.
- [Bažant 00] Z. P. Bažant, F. C. Caner, M. D. Adley & S. A. Akers. *Fracturing rate effect and creep in microplane model for dynamics*. Journal of Engineering Mechanics-ASCE, vol. 126, no. 9, pages 962–970, 2000.
- [Bažant 02] Z. P. Bažant & M. Jirásek. *Nonlocal integral formulations of plasticity and damage: Survey of progress*. Journal of Engineering Mechanics, vol. 128, no. 11, pages 1119–1149, 2002.

## Bibliography

---

- [Bazant 86] Z.P. Bazant, F.C. Bishop & T.P. Chang. *Confined compression tests of cement paste and concrete up to 300 ksi*. Journal of the American Concrete Institute, vol. 83, no. 4, pages 553–560, 1986.
- [Beyer 10] K. Beyer, A. Abo-El-Ezz & A. Dazio. *Quasi-static cyclic tests on different types of masonry spandrels*. Rapport technique 327, Institute of Structural Engineering, Swiss Federal Institute of Technology, Zürich, 2010.
- [Beyer 11] K. Beyer & A. Dazio. *Quasi-static monotonic and cyclic tests on composite spandrels*. Earthquake Spectra, vol. in press, 2011.
- [Bi 02] X. Bi, Z. Li, P. H. Geubelle & J. Lambros. *Dynamic fiber debonding and frictional push-out in model composite systems: Numerical simulations*. Mechanics of Materials, vol. 34, no. 7, pages 433–446, 2002.
- [Birkimer 68] D.L. Birkimer. *Critical normal fracture strain of cement portland concrete*. PhD thesis, University of Cincinnati, Ohio, 1968.
- [Bischoff 91] P. H. Bischoff & S. H. Perry. *Compressive behaviour of concrete at high strain rates*. Materials and Structures, vol. 24, pages 425–450, 1991.
- [Bolander Jr. 98] J. E. Bolander Jr. & S. Saito. *Fracture analysis using spring networks with random geometry*. Engineering Fracture Mechanics, vol. 61, no. 5-6, pages 569–591, 1998.
- [Brara 99] A. Brara. *Experimental study of dynamic tension of concrete via spalling*. PhD thesis, Laboratory of Physics and Mechanics of Materials, Metz University, France, 1999.
- [Brara 06] A. Brara & J. R. Klepaczko. *Experimental characterization of concrete in dynamic tension*. Mechanics of Materials, vol. 38, no. 3, pages 253–267, 2006.
- [Brara 07] A. Brara & J. R. Klepaczko. *Fracture energy of concrete at high loading rates in tension*. International Journal of Impact Engineering, vol. 34, no. 3, pages 424–435, 2007.
- [Brühwiler 90] E. Brühwiler & F. H. Wittmann. *Failure of dam concrete subjected to seismic loading conditions*. Engineering Fracture Mechanics, vol. 35, no. 1-3, pages 565–571, 1990.
- [Burlion 01] N. Burlion, G. Pijaudier-Cabot & N. Dahan. *Experimental analysis of compaction of concrete and mortar*. International Journal for Numerical and Analytical Methods in Geomechanics, vol. 25, no. 15, pages 1467–1486, 2001.

- [Caballero 05] A. Caballero. *3D meso-mechanical numerical analysis of concrete using interface elements*. PhD thesis, Universitat Politècnica de Catalunya, Spain, 2005.
- [Caballero 06] A. Caballero, C. M. López & I. Carol. *3D meso-structural analysis of concrete specimens under uniaxial tension*. *Computer Methods in Applied Mechanics and Engineering*, vol. 195, no. 52, pages 7182–7195, 2006.
- [Cadoni 01] E. Cadoni, K. Labibes, C. Albertini, M. Berra & M. Giangrasso. *Strain rate effect on the tensile behaviour of concrete at different relative humidity levels*. *Materials and Structures*, vol. 34, pages 21–26, 2001.
- [Caliskan 02] S. Caliskan, B. L. Karihaloo & B. I. G. Barr. *Study of rock-mortar interfaces. Part II: Strength of interface*. *Magazine of Concrete Research*, vol. 54, no. 6, pages 463–472, 2002.
- [Camacho 96] G. T. Camacho & M. Ortiz. *Computational modelling of impact damage in brittle materials*. *International Journal of Solids and Structures*, vol. 33, no. 20-22, pages 2899–2938, 1996.
- [Camborde 00] F. Camborde, F. V. Donzé & Mariotti. *Numerical study of rock and concrete behaviour by discrete element modelling*. *Computers and Geotechnics*, vol. 27, pages 225–247, 2000.
- [Candappa 01] D. C. Candappa, J. G. Sanjayan & S. Setunge. *Complete triaxial stress-strain curves of high-strength concrete*. *Journal of Materials in Civil Engineering*, vol. 13, no. 3, pages 209–215, 2001.
- [Carol 92] I. Carol, P. C. Prat & Z. P. Bažant. *New explicit microplane model for concrete: Theoretical aspects and numerical implementation*. *International Journal of Solids and Structures*, vol. 29, no. 9, pages 1173–1191, 1992.
- [Carol 01] I. Carol, C. M. López & O. Roa. *Micromechanical analysis of quasi-brittle materials using fracture-based interface elements*. *International Journal for Numerical Methods in Engineering*, vol. 52, no. 1-2, pages 193–215, 2001.
- [Cervenka 98] J. Cervenka, J. M. Chandra Kishen & V. E. Saouma. *Mixed mode fracture of cementitious bimaterial interfaces; part II: Numerical simulation*. *Engineering Fracture Mechanics*, vol. 60, no. 1, pages 95–107, 1998.
- [Chaboche 97] J. L. Chaboche, R. Girard & A. Schaff. *Numerical analysis of composite systems by using interphase/interface models*. *Computational Mechanics*, vol. 20, no. 1-2, pages 3–11, 1997.
- [Chambart 09] M. Chambart. *Endommagement anisotrope et comportement dynamique des structures en béton armé jusqu'à la ruine*. PhD thesis, ENS Cachan, France, 2009.

## Bibliography

---

- [Chandra 95] N. Chandra & C. R. Ananth. *Analysis of interfacial behavior in MMCs and IMCs by the use of thin-slice push-out tests*. Composites Science and Technology, vol. 54, no. 1, pages 87–100, 1995.
- [Cirak 05] F. Cirak & M. West. *Decomposition contact response (DCR) for explicit finite element dynamics*. International Journal for Numerical Methods in Engineering, vol. 64, pages 1078–1110, 2005.
- [Coenen 12] E. W. C. Coenen, V. G. Kouznetsova & M. G. D. Geers. *Novel boundary conditions for strain localization analyses in microstructural volume elements*. International Journal for Numerical Methods in Engineering, vol. 90, no. 1, pages 1–21, 2012.
- [Cotsovos 08] D. M. Cotsovos & M. N. Pavlović. *Numerical investigation of concrete subjected to compressive impact loading. Part 1: A fundamental explanation for the apparent strength gain at high loading rates*. Computers and Structures, vol. 86, pages 145–163, 2008.
- [Cusatis 06] G. Cusatis & D. Pelessone. *Mesolevel simulation of reinforced concrete structures under impact loadings*. In Computational Modelling of Concrete Structures - Proceedings of EURO-C 2006, pages 63–70, 2006.
- [Del Piero 10] G. Del Piero & M. Raous. *A unified model for adhesive interfaces with damage, viscosity, and friction*. European Journal of Mechanics, A/Solids, vol. 29, no. 4, pages 496–507, 2010.
- [Desmorat 10a] R. Desmorat, M. Chambart, F. Gatuingt & D. Guilbaud. *Delay-active damage versus non-local enhancement for anisotropic damage dynamics computations with alternated loading*. Engineering Fracture Mechanics, vol. 77, no. 12, pages 2294–2315, 2010.
- [Desmorat 10b] R. Desmorat, F. Gatuingt & F. Ragueneau. *Nonstandard Thermodynamics Framework for Robust Computations with Induced Anisotropic Damage*. International Journal of Damage Mechanics, vol. 19, no. 1, pages 53–73, 2010.
- [Dollar 93] A. Dollar, P. S. Steif, Y. C. Wang & C. Y. Hui. *Analyses of the fiber push-out test*. International Journal of Solids and Structures, vol. 30, no. 10, pages 1313–1329, 1993.
- [Dongarra 06] J. Dongarra, K. Seymour & A. YarKhan. *Users' Guide to GridSolve, Version 0.15*. Rapport technique, University of Tennessee, Knoxville, TN, USA, 2006.
- [Donzé 99] F. V. Donzé, S. Magnier, L. Daudeville, C. Mariotti & L. Davenne. *Numerical study of compressive behavior of concrete at high strain rates*. Journal of Engineering Mechanics, vol. 125, no. 10, pages 1154–1162, 1999.

- [Dubé 96] J. F. Dubé, G. Pijaudier-Cabot & C. La Borderie. *Rate dependent damage model for concrete in dynamics*. Journal of Engineering Mechanics-ASCE, vol. 122, no. 10, pages 939–947, 1996.
- [Dugdale 60] D. S. Dugdale. *Yielding of steel sheets containing slits*. Journal of the Mechanics and Physics of Solids, vol. 8, pages 100–108, 1960.
- [EN 09] EN 933-1. *Tests for geometrical properties of aggregates - Part 1 : determination of particle size distribution - Sieving method*, 2009.
- [Erzar 10] B. Erzar & P. Forquin. *An Experimental Method to Determine the Tensile Strength of Concrete at High Rates of Strain*. Experimental Mechanics, vol. 50, no. 7, pages 941–955, 2010.
- [Fairhurst 64] C. Fairhurst. *On the validity of the “Brazilian” test for brittle materials*. International Journal of Rock Mechanics and Mining Sciences and, vol. 1, no. 4, pages 535–546, 1964.
- [Falk 01] M. L. Falk, A. Needleman & J. R. Rice. *A critical evaluation of cohesive zone models of dynamic fracture*. In Journal De Physique. IV : JP, volume 11, pages Pr543–Pr550, 2001.
- [Feenstra 96] P. H. Feenstra & R. De Borst. *A composite plasticity model for concrete*. International Journal of Solids and Structures, vol. 33, no. 5, pages 707–730, 1996.
- [Fernández Ruiz 07] M. Fernández Ruiz, A. Muttoni & P. Gambarova. *Relationship between nonlinear creep and cracking of concrete under uniaxial compression*. Journal of Advanced Concrete Technology, vol. 5, pages 383–393, 2007.
- [Feyel 03] F. Feyel. *A multilevel finite element method (FE2) to describe the response of highly non-linear structures using generalized continua*. Computer Methods in Applied Mechanics and Engineering, vol. 192, no. 28-30, pages 3233–3244, 2003.
- [Fouchal 09] F. Fouchal, F. Lebon & I. Titeux. *Contribution to the modelling of interfaces in masonry construction*. Construction and Building Materials, vol. 23, no. 6, pages 2428–2441, 2009.
- [Fuller 06] W. B. Fuller & S. E. Thompson. *The Laws of Proportioning Concrete*. Transactions of the American Society of Civil Engineers, vol. 57, pages 67–143, 1906.
- [Ganz 84] H. Ganz & B. Thürlimann. *Versuche an Mauerwerksscheiben unter Normalkraft und Querkraft*. Rapport technique 7502-4, Institute of Structural Engineering, Swiss Federal Institute of Technology, Zürich, 1984.

## Bibliography

---

- [Gatuingt 02] F. Gatuingt & G. Pijaudier-Cabot. *Coupled damage and plasticity modeling in transient dynamic analysis of concrete*. International Journal for Numerical and Analytical Methods in Geomechanics, vol. 26, pages 1–24, 2002.
- [Gatuingt 08] F. Gatuingt, R. Desmorat, M. Chambart, D. Combescure & D. Guilbaud. *Anisotropic 3D delay-damage model to simulate concrete structures*. Revue Européenne de mécanique numérique, vol. 17, pages 740–60, 2008.
- [Gatuingt 12] F. Gatuingt, L. Snozzi & J. F. Molinari. *Numerical determination of the tensile response and the dissipated fracture energy of concrete: role of the meso-structure and influence of the loading rate*. International Journal for Numerical and Analytical Methods in Geomechanics, 2012. Accepted.
- [Geers 10] M. G. D. Geers, V. G. Kouznetsova & W. A. M. Brekelmans. *Multi-scale computational homogenization: Trends and challenges*. Journal of Computational and Applied Mathematics, vol. 234, no. 7, pages 2175–2182, 2010.
- [Geubelle 98] P. H. Geubelle & J. S. Baylor. *Impact-induced delamination of composites: A 2D simulation*. Composites Part B: Engineering, vol. 29, no. 5, pages 589–602, 1998.
- [Gitman 07] I. M. Gitman, H. Askes & L. J. Sluys. *Representative volume: Existence and size determination*. Engineering Fracture Mechanics, vol. 74, no. 16, pages 2518–2534, 2007.
- [Gitman 08] I. M. Gitman, H. Askes & L. J. Sluys. *Coupled-volume multi-scale modelling of quasi-brittle material*. European Journal of Mechanics, A/Solids, vol. 27, no. 3, pages 302–327, 2008.
- [Grassl 06] P. Grassl & M. Jirásek. *Damage-plastic model for concrete failure*. International Journal of Solids and Structures, vol. 43, no. 22-23, pages 7166–7196, 2006.
- [Grassl 08] P. Grassl & R. Rempling. *A damage-plasticity interface approach to the meso-scale modelling of concrete subjected to cyclic compressive loading*. Engineering Fracture Mechanics, vol. 75, no. 16, pages 4804–4818, 2008.
- [Grassl 10] P. Grassl & M. Jirásek. *Meso-scale approach to modelling the fracture process zone of concrete subjected to uniaxial tension*. International Journal of Solids and Structures, vol. 47, no. 7-8, pages 957–968, 2010.
- [Griffith 20] A. A. Griffith. *The phenomena of rupture and flow in solids*. Philosophical Transactions of the Royal Society of London, vol. 221, pages 163–198, 1920.

- [Guinea 02] G.V. Guinea, K. El-Sayed, C.G. Rocco, M. Elices & J. Planas. *The effect of the bond between the matrix and the aggregates on the cracking mechanism and fracture parameters of concrete*. Cement and Concrete Research, vol. 32, no. 12, pages 1961–1970, 2002.
- [Hervé 05] G. Hervé, F. Gatuingt & A. Ibrahimbegovic. *On numerical implementation of a coupled rate dependent damage-plasticity constitutive model for concrete in application to high-rate dynamics*. Engineering Computations, vol. 22, no. 5-6, pages 583–604, 2005.
- [Hillerborg 76] A. Hillerborg, E. Modéer & P. E. Petersson. *Analysis of crack formation and crack growth in concrete by means of fracture mechanics and finite elements*. Cement and Concrete Research, vol. 6, no. 6, pages 773–781, 1976.
- [Hirai 84] Itio Hirai, Bo P. Wang & Walter D. Pilkey. *Efficient zooming method for finite element analysis*. International Journal for Numerical Methods in Engineering, vol. 20, no. 9, pages 1671–1683, 1984.
- [Horii 85] H. Horii & S. Nematnasser. *Compression-Induced Microcrack Growth in Brittle Solids: Axial Splitting and Shear Failure*. Journal of Geophysical Research, vol. 90, pages 3105–3125, 1985.
- [Janach 76] W. Janach. *The role of bulking in brittle failure of rocks under rapid compression*. International Journal of Rock Mechanics and Mining Sciences and, vol. 13, no. 6, pages 177–186, 1976.
- [Jean 01] M. Jean, V. Acary & Y. Monerie. *Non-smooth contact dynamics approach of cohesive materials*. Philosophical Transactions of the Royal Society A: Mathematical, Physical and Engineering Sciences, vol. 359, no. 1789, pages 2497–2518, 2001.
- [Jerier 12] J. F. Jerier & J. F. Molinari. *Normal contact between rough surfaces by the Discrete Element Method*. Tribology International, vol. 47, pages 1–8, 2012.
- [Jirásek 98] M. Jirásek. *Nonlocal models for damage and fracture: Comparison of approaches*. International Journal of Solids and Structures, vol. 35, no. 31-32, pages 4133–4145, 1998.
- [John 92] R. John, T. Antoun & A.M. Rajendran. *Effect of strain rate and size on tensile strength of concrete*. In APS Topical Conference on Shock Compression of Condensed Matter, Williamsburg, VA, pages 501–504, 1992.
- [Ju 89] J. W. Ju. *On energy-based coupled elastoplastic damage theories: Constitutive modeling and computational aspects*. International Journal of Solids and Structures, vol. 25, no. 7, pages 803–833, 1989.

## Bibliography

---

- [Kaczmarczyk 10] L. Kaczmarczyk, C. J. Pearce, N. Bićanić & E. de Souza Neto. *Numerical multiscale solution strategy for fracturing heterogeneous materials*. Computer Methods in Applied Mechanics and Engineering, vol. 199, no. 17-20, pages 1100–1113, 2010.
- [Kikuchi 88] N. Kikuchi & J.T. Oden. *Contact problems in elasticity: A study of variational inequalities and finite element methods*. SIAM, Philadelphia, 1988.
- [Klein 01] P. A. Klein, J. W. Foulk, E. P. Chen, S. A. Wimmer & H. J. Gao. *Physics-based modeling of brittle fracture: Cohesive formulations and the application of meshfree methods*. Theoretical and Applied Fracture Mechanics, vol. 37, no. 1-3, pages 99–166, 2001.
- [Kormeling 87] H. A. Kormeling & H. W. Reinhardt. *Strain rate effects on steel fibre concrete in uniaxial tension*. Int. Journal of Cement Composites and Lightweight Concrete, vol. 9, no. 4, pages 197–204, 1987.
- [Koutromanos 12] I. Koutromanos & P. B. Shing. *Cohesive crack model to simulate cyclic response of concrete and masonry structures*. ACI Structural Journal, vol. 109, no. 3, pages 349–358, 2012.
- [Kouznetsova 02] V. Kouznetsova, M. G. D. Geers & W. A. M. Brekelmans. *Multi-scale constitutive modelling of heterogeneous materials with a gradient-enhanced computational homogenization scheme*. International Journal for Numerical Methods in Engineering, vol. 54, no. 8, pages 1235–1260, 2002.
- [Kozicki 07] J. Kozicki & J. Teichman. *Effect of aggregate structure on fracture process in concrete using 2D lattice model*. Archives of Mechanics, vol. 59, pages 365–384, 2007.
- [Kraft 08] R. H. Kraft, J. F. Molinari, K. T. Ramesh & D. H. Warner. *Computational micromechanics of dynamic compressive loading of a brittle polycrystalline material using a distribution of grain boundary properties*. Journal of the Mechanics and Physics of Solids 56, vol. 56, no. 8, pages 2618–2641, 2008.
- [Kubair 03] D. V. Kubair, P. H. Geubelle & Y. Y. Huang. *Analysis of a rate-dependent cohesive model for dynamic crack propagation*. Engineering Fracture Mechanics, vol. 70, no. 5, pages 685–704, 2003.
- [Kulkarni 10] M. G. Kulkarni, K. Matouš & P. H. Geubelle. *Coupled multi-scale cohesive modeling of failure in heterogeneous adhesives*. International Journal for Numerical Methods in Engineering, vol. 84, no. 8, pages 916–946, 2010.



- [Lahlou 92] K. Lahlou, P. Aitcin & O. Chaallal. *Behaviour of high-strength concrete under confined stresses*. Cement and Concrete Composites, vol. 14, no. 3, pages 185–193, 1992.
- [Lambert 00] D. E. Lambert & C. A. Ross. *Strain rate effects on dynamic fracture and strength*. International Journal of Impact Engineering, vol. 24, no. 10, pages 985–998, 2000.
- [Langer 09] L. A. Langer, W. C. Carter & E. R. Fuller. *The PPM2OOF manual*. Rapport technique, NIST, 2009.
- [Lemaitre 78] J. Lemaitre & J.L. Chaboche. *Phenomenological approach of damage rupture*. Journal de Mécanique Appliquée, vol. 2, pages 317–365, 1978.
- [Leonhardt 62] F. Leonhardt & R. Walther. *Schubversuche an einfeldrigen stahlbetonbalken mit und ohne schubbewehrung*. Ernst & Sohn, Deutscher Ausschuss für Stahlbeton, Heft 151, 1962.
- [Lin 01] G. Lin, P. H. Geubelle & N. R. Sottos. *Simulation of fiber debonding with friction in a model composite pushout test*. International Journal of Solids and Structures, vol. 38, no. 46-47, pages 8547–8562, 2001.
- [Lourenço 97] P.B. Lourenço & J.G. Rots. *Multisurface interface model for analysis of masonry structures*. Journal of Engineering Mechanics, vol. 123, no. 7, pages 660–668, 1997.
- [Malvar 98] L. J. Malvar & C. A. Ross. *Review of strain rate effects for concrete in tension*. ACI Materials Journal, vol. 95, no. 6, pages 735–739, 1998.
- [Marigo 81] J.-J. Marigo. *Formulation d'une loi d'endommagement d'un matériau élastique*. Compte-Rendus de l'Académie des Sciences de Paris, vol. 292, pages 1309–1312, 1981.
- [Markovic 06] D. Markovic & A. Ibrahimbegovic. *Complementary energy based FE modelling of coupled elasto-plastic and damage behavior for continuum microstructure computations*. Computer Methods in Applied Mechanics and Engineering, vol. 195, no. 37-40, pages 5077–5093, 2006.
- [Mazars 84] J. Mazars. *Application de la mécanique de l'endommagement au comportement non linéaire et à la rupture du béton de structure*. PhD thesis, Laboratoire de Mécanique et Technologie, ENS Cachan, 1984.
- [Mc Vay 88] M.K. Mc Vay. *Spall damage of concrete structures*. Rapport technique SL-88-22, US Army Corps of Engineers, Waterways Experiment Station, Vicksburg, Miss., USA, 1988.

## Bibliography

---

- [Mesarovic 05] S. D. Mesarovic & J. Padbidri. *Minimal kinematic boundary conditions for simulations of disordered microstructures*. Philosophical Magazine, vol. 85, no. 1, pages 65–78, 2005.
- [Miller 99] O. Miller, L. B. Freund & A. Needleman. *Modeling and simulation of dynamic fragmentation in brittle materials*. International Journal of Fracture, vol. 96, no. 2, pages 101–125, 1999.
- [Monteiro 93] P. J. M. Monteiro, P. R. L. Helene & S. H. Kang. *Designing concrete mixtures for strength, elastic modulus and fracture energy*. Materials and Structures, vol. 26, no. 8, pages 443–452, 1993.
- [Murray 79] David W. Murray, Larp Chitnuyanondh & Khazal Y. Rijub-Agha. *Concrete plasticity theory for biaxial stress analysis*. ASCE J Eng Mech Div, vol. 105, no. 6, pages 989–1006, 1979.
- [Muttoni 08] A. Muttoni & M.F. Ruiz. *Shear strength of members without transverse reinforcement as function of critical shear crack width*. ACI Structural Journal, vol. 105, no. 2, pages 163–172, 2008.
- [Muttoni 12] A. Muttoni & M.F. Ruiz. *The Critical Shear Crack Theory as a physical model for punching shear design and its implementation into new Model Code 2010*. Hormigón y Acero, vol. 263, pages 49–63, 2012.
- [Newmark 59] N.M. Newmark. *A method of computation for structural dynamics*. Journal of Engineering Mechanics, ASCE, vol. 85, pages 67–94, 1959.
- [N’Guyen 10a] T. D. N’Guyen, C. Lawrence, C. La Borderie & G. Nahas. *A mesoscopic approach for a better understanding of the transition from diffuse damage to localized damage*. European Journal of Environmental and Civil Engineering, vol. 14, no. 1-10, pages 751–776, 2010.
- [Nguyen 10b] V. P. Nguyen, O. Lloberas-Valls, M. Stroeven & L. Johannes Sluys. *On the existence of representative volumes for softening quasi-brittle materials - A failure zone averaging scheme*. Computer Methods in Applied Mechanics and Engineering, vol. 199, no. 45-48, pages 3028–3038, 2010.
- [Nguyen 11] V. P. Nguyen, O. Lloberas-Valls, M. Stroeven & L. J. Sluys. *Homogenization-based multiscale crack modelling: From micro-diffusive damage to macro-cracks*. Computer Methods in Applied Mechanics and Engineering, vol. 200, no. 9-12, pages 1220–1236, 2011.
- [Nguyen 12] V. P. Nguyen, O. Lloberas-Valls, M. Stroeven & L. J. Sluys. *Computational homogenization for multiscale crack modeling. Implementational and computational aspects*. International Journal for Numerical Methods in Engineering, vol. 89, no. 2, 2012.

- [Oh 90] B. H. Oh. *Fracture behavior of concrete under high rates of loading*. Int. J. Eng. Fract. Mech., vol. 35, no. 1/2/3, pages 327–332, 1990.
- [Ottosen 79] N. S. Ottosen. *Constitutive model for short-time loading of concrete*. Journal of the Engineering Mechanics Division-ASCE, vol. 105, no. 1, pages 127–141, 1979.
- [Ožbolt 94] J. Ožbolt, R. Eligehausen & M. Petrangeli. *The Size Effect in Concrete Structures*. In H. Mihashi, H. Okamura & Z.P. Bažant, editors, Size Effect In Concrete Structures, pages 255–268. E & FN Spon, London, 1994.
- [Ožbolt 01] J. Ožbolt, Y. Li & I. Kožar. *Microplane model for concrete with relaxed kinematic constraint*. International Journal of Solid and Structure, vol. 38, pages 2683–2711, 2001.
- [Palmer 73] A. C. Palmer & J. R. Rice. *The growth of slip surfaces in the progressive failure of over-consolidated clay*. Proceedings of the Royal Society of London, Series A, vol. 332, pages 527–548, 1973.
- [Pandolfi 99] A. Pandolfi & M. Ortiz. *Finite-deformation irreversible cohesive elements for three dimensional crack-propagation analysis*. International Journal for Numerical Methods in Engineering, vol. 74, pages 1393–1420, 1999.
- [Park 09] K. Park, G. H. Paulino & J. R. Roesler. *A unified potential-based cohesive model of mixed-mode fracture*. Journal of the Mechanics and Physics of Solids, vol. 57, no. 6, pages 891–908, 2009.
- [Pedersen 07] R. R. Pedersen, A. Simone, M. Stroeven & L. J. Sluys. *Mesoscopic modelling of concrete under impact*. In 6th International Conference on Fracture Mechanics of Concrete and Concrete Structures - FRAMCOS VI, pages 571–578, 2007.
- [Pedersen 08] R. R. Pedersen, A. Simone & L. J. Sluys. *An analysis of dynamic fracture in concrete with a continuum visco-elastic visco-plastic damage model*. Engineering Fracture Mechanics, vol. 75, pages 3782–805, 2008.
- [Pietruszczak 81] S. Pietruszczak & Z. Mroz. *Finite element analysis of deformation of strain-softening materials*. International Journal for Numerical Methods in Engineering, vol. 17, no. 3, pages 327–334, 1981.
- [Pijaudier-Cabot 87] G. Pijaudier-Cabot & Z.P. Bažant. *Non local damage theory*. Journal of Engineering Mechanics, vol. 113, no. 10, pages 1512–1533, 1987.
- [Pina-Henriques 06] J. Pina-Henriques & P.B. Lourenço. *Masonry compression: A numerical investigation at the meso-level*. Engineering Computations (Swansea, Wales), vol. 23, no. 4, pages 382–407, 2006.

## Bibliography

---

- [Planas 91] J. Planas & M. Elices. *Nonlinear fracture of cohesive materials*. International Journal of Fracture, vol. 51, no. 2, pages 139–157, 1991.
- [Pontiroli 10] C. Pontiroli, A. Rouquand & J. Mazars. *Predicting concrete behaviour from quasi-static loading to hypervelocity impact An overview of the PRM model*. European Journal of Environmental and Civil Engineering, vol. 14, no. 6-7, pages 703–727, 2010.
- [Prado 03] E. P. Prado & J. G. M. van Mier. *Effect of particle structure on mode I fracture process in concrete*. Engineering Fracture Mechanics, vol. 70, no. 14, pages 1793–1807, 2003.
- [Ragueneau 98] F. Ragueneau, J. Mazars & C. La Borderie. *Damage model for concrete including residual hysteretic loops: application to seismic and dynamic loading*. In Framcos 3, editeur, 3d Conference on Fracture Mechanics of Concrete Structures, volume 1, pages 685–696, 1998.
- [Raous 97] M. Raous, L. Cangèmi & M. Cocu. *An adhesion and friction model for the contact between two deformable bodies*. Comptes Rendus de l'Academie de Sciences - Serie IIb: Mecanique, Physique, Chimie, Astronomie, vol. 325, no. 9, pages 503–509, 1997.
- [Raous 09] M. Raous & M. A. Karray. *Model coupling friction and adhesion for steel-concrete interfaces*. International Journal of Computer Applications in Technology, vol. 34, no. 1, pages 42–51, 2009.
- [Reinhardt 81] H.W. Reinhardt. *Similitude of Brittle Fracture of Structural Concrete*. In IABSE Colloquium on Advances in Reinforced Concrete, Delft, pages 175–184, 1981.
- [Renard 87] J. Renard & M.-F. Marmonier. *Etude de l'initiation de l'endommagement dans la matrice d'un matériau composite par une méthode d'homogénéisation*. La Recherche aérospatiale, pages 43–51, 1987.
- [Rice 68] J.L. Rice. *Mathematical analysis in the mechanics of fracture. Chapter 3 of Fracture: An Advanced Treatise*. Academic press, vol. 2, pages 191–311, 1968.
- [Richart 29] F. E. Richart, A. Brandtzaeg & R. L. Brown. *Failure of Plain and Spirally Reinforced Concrete in Compression*. Rapport technique 190, University of Illinois, Urbana, April 1929.
- [Roelfstra 85] P. Roelfstra, H. Sadouki & F. Wittmann. *Le béton numérique*. Materials & Structures - RILEM, vol. 18, pages 309–317, 1985.
- [Ross 95] C. A. Ross, Joseph W. Tedesco & Steven T. Kuennen. *Effects of strain rate on concrete strength*. ACI Materials Journal, vol. 92, no. 1, pages 37–47, 1995.

- [Rosselló 04] C. Rosselló & M. Elices. *Fracture of model concrete: 1. Types of fracture and crack path*. Cement and Concrete Research, vol. 34, no. 8, pages 1441–1450, 2004.
- [Rosselló 06] C. Rosselló, M. Elices & G. V. Guinea. *Fracture of model concrete: 2. Fracture energy and characteristic length*. Cement and Concrete Research, vol. 36, pages 1345–1353, 2006.
- [Rossi 92] P. Rossi, J. G. M. van Mier, C. Boulay & F. Le Maou. *The dynamic behaviour of concrete: influence of free water*. Materials and Structures, vol. 25, pages 509–514, 1992.
- [Rossi 94] P. Rossi, J. G. M. van Mier, F. Toutlemonde & C. Maou Fand Boulay. *Effect of loading rate on the strength of concrete subjected to uniaxial tension*. Materials and Structures, vol. 27, pages 260–264, 1994.
- [Ruiz 00] G. Ruiz, M. Ortiz & A. Pandolfi. *Three-dimensional finite-element simulation of the dynamic Brazilian tests on concrete cylinders*. International Journal for Numerical Methods in Engineering, vol. 48, no. 7, pages 963–994, 2000.
- [Sacco 10] E. Sacco & J. Toti. *Interface elements for the analysis of masonry structures*. International Journal of Computational Methods in Engineering Science and Mechanics, vol. 11, no. 6, pages 354–373, 2010.
- [Sagasetta 11] J. Sagasetta & R. L. Vollum. *Influence of aggregate fracture on shear transfer through cracks in reinforced concrete*. Magazine of Concrete Research, vol. 63, no. 2, pages 119–137, 2011.
- [Schlangen 92] E. Schlangen & J. G. M. van Mier. *Simple lattice model for numerical simulation of fracture of concrete materials and structures*. Materials and Structures, vol. 25, no. 9, pages 534–542, 1992.
- [Sercombe 98] J. Sercombe, F. J. Ulm & F. Toutlemonde. *Viscous hardening plasticity for concrete in high-rate dynamics*. Journal of Engineering Mechanics-ASCE, vol. 124, no. 9, pages 1050–1057, 1998.
- [Sfer 02] D. Sfer, I. Carol, R. Gettu & G. Etse. *Study of the behavior of concrete under triaxial compression*. Journal of Engineering Mechanics, vol. 128, no. 2, pages 156–163, 2002.
- [Sluys 92] L. J. Sluys. *Wave propagation, localization and dispersion in softening solids*. Doct. Dissertation, Delft University of Technologie–Delft, 1992.
- [Snozzi 12a] L. Snozzi, F. Gatuingt & J. F. Molinari. *A meso-mechanical model for concrete under dynamic tensile and compressive loading*. International Journal of Fracture, 2012. Article in Press.

## Bibliography

---

- [Snozzi 12b] L. Snozzi & J. F. Molinari. *A cohesive element model for mixed mode loading with frictional contact capability*. International Journal for Numerical Methods in Engineering, 2012. Article in Press.
- [Stankowski 90] T. Stankowski. *Numerical simulation of progressive failure in particle composites*. PhD thesis, University of Colorado, USA, 1990.
- [Suquet 85] Pierre M. Suquet. *Local and Global Aspects in the Mathematical Theory of Plasticity*. pages 279–310, 1985.
- [Talon 03] C. Talon & A. Curnier. *A model of adhesion coupled to contact and friction*. European Journal of Mechanics, A/Solids, vol. 22, no. 4, pages 545–565, 2003.
- [Terada 00] K. Terada, M. Hori, T. Kyoya & N. Kikuchi. *Simulation of the multi-scale convergence in computational homogenization approaches*. International Journal of Solids and Structures, vol. 37, no. 16, pages 2285–2311, 2000.
- [Tijssens 01] M. G. A. Tijssens, L. J. Sluys & E. Van der Giessen. *Simulation of fracture of cementitious composites with explicit modeling of microstructural features*. Engineering Fracture Mechanics, vol. 68, no. 11, 2001.
- [Toutlemonde 94] F. Toutlemonde. *Shock strength of concrete structures; From material behaviour to structure design*. PhD thesis, E.N.P.C., placeCityParis, 1994.
- [Tsai 05] J. H. Tsai, A. Patra & R. Wetherhold. *Finite element simulation of shaped ductile fiber pullout using a mixed cohesive zone/friction interface model*. Composites Part A: Applied Science and Manufacturing, vol. 36, no. 6, pages 827–838, 2005.
- [Turner 54] M. J. Turner, R. W. Clough, H. C. Martin & L. J. Topp. *Stiffness and deflection analysis of complex structures*. Journal of the Aeronautical Sciences, vol. 23, pages 805–824, 1954.
- [Tvergaard 90] V. Tvergaard. *Effect of fibre debonding in a whisker-reinforced metal*. Materials Science and Engineering A, vol. 125, no. 2, pages 203–213, 1990.
- [Unger 11] J. F. Unger & S. Eckardt. *Multiscale Modeling of Concrete*. Archives of Computational Methods in Engineering, vol. 18, no. 3, pages 341–393, 2011.
- [Van der Pluijm 92] R. Van der Pluijm. *Material properties of Masonry and its Components under Tension and Shear*. In Proceedings of 6<sup>th</sup> Canadian masonry symposium, Saskatoon, Canada, page 1992, 1992.

- [Van Doormaal 94] J. C. A. M. Van Doormaal, J. Weerheijm & L. J. Sluys. *Experimental and numerical determination of the dynamic fracture energy of concrete*. Journal de physique IV, vol. 4, no. C8, pages 501–506, 1994.
- [van Mier 97] JGM van Mier. *Fracture processes of concrete*. USA: CRC Press Inc, 1997.
- [Vegt 06] I. Vegt, R. R. Pedersen, L. J. Sluys & J. Weerheijm. *Modelling of impact behaviour of concrete - An experimental approach*. In Computational Modelling of Concrete Structures - EURO-C 2006, pages 451–458, 2006.
- [Verhoosel 10] C. V. Verhoosel, J. J. C. Remmers, M. A. Gutiérrez & R. de Borst. *Computational homogenization for adhesive and cohesive failure in quasi-brittle solids*. International Journal for Numerical Methods in Engineering, vol. 83, no. 8-9, pages 1155–1179, 2010.
- [Von den Bosch 05] M. J. Von den Bosch, Schreurs P. J. G. & M. G. D. Geers. *A critical evaluation of the exponential Xu and Needleman cohesive zone law for mixed mode decohesion*. Engineering Fracture Mechanics, vol. 72, pages 2247–2267, 2005.
- [Vonk 93] R. A. Vonk. *Micromechanical investigation of softening of concrete loaded in compression*. Heron, vol. 38, pages 5–94, 1993.
- [Walraven 80] J.C. Walraven. *Aggregate interlock: a theoretical and experimental investigation*. PhD thesis, Delft University of Technology, The Netherlands, 1980.
- [Warner 06] D. H. Warner & J. F. Molinari. *Micromechanical finite element modeling of compressive fracture in confined alumina ceramic*. Acta Materialia, vol. 54, no. 19, pages 5135–5145, 2006.
- [Weerheijm 07] J. Weerheijm, I. Vegt & K. van Breugel. *Research developments and experimental data on dynamic concrete behaviour*. In Conference on Advances in Construction Materials, pages 765–773, 2007.
- [Willam 86] K. Willam, N. Bicanic, E. Pramono & S. Sture. *Composite Fracture Model for Strain-Softening Computations of Concrete*. In F.H. Wittmann, editeur, Proc. Fracture Toughness and Fracture Energy of Concrete, volume 45, pages 149–162, 1986.
- [Willam 04] K. Willam, I. Rhee & B. Shing. *Interface damage model for thermomechanical degradation of heterogeneous materials*. Computer Methods in Applied Mechanics and Engineering, vol. 193, no. 30-32, 2004.
- [William 84] K. J. William. *Experimental and computational aspects of concrete fracture*. pages 33–70, 1984.

## Bibliography

---

- [Wittmann 83] F. H. Wittmann. *Structure of concrete with respect to crack formation*. Fracture Mechanics of Concrete, Elsevier Science Publishers, pages 43–74, 1983.
- [Wriggers 06] P. Wriggers & S. O. Moftah. *Mesoscale models for concrete: Homogenisation and damage behaviour*. Finite Elements in Analysis and Design, vol. 42, no. 7 SPEC. ISS., pages 623–636, 2006.
- [Wu 01] K. . Wu, B. Chen, W. Yao & D. Zhang. *Effect of coarse aggregate type on mechanical properties of high-performance concrete*. Cement and Concrete Research, vol. 31, no. 10, pages 1421–1425, 2001.
- [Xu 93] X. P. Xu & A. Needleman. *Void nucleation by inclusions debonding in a crystal matrix*. Modelling and Simulation in Materials Science and Engineering, vol. 1, pages 111–132, 1993.
- [Yan 06] D. Yan & G. Lin. *Dynamic properties of concrete in direct tension*. Cement and Concrete Research, vol. 36, no. 7, pages 1371–1378, 2006.
- [Zhou 05] F. Zhou, J. F. Molinari & T. Shioya. *A rate-dependent cohesive model for simulating dynamic crack propagation in brittle materials*. Engineering Fracture Mechanics, vol. 72, no. 9, pages 1383–1410, 2005.
- [Zubelewicz 87] Aleksander Zubelewicz & Zdenek P. Bazant. *Interface Element Modeling of Fracture in Aggregate Composites*. Journal of Engineering Mechanics, vol. 113, no. 11, pages 1619–1630, 1987.



## LEONARDO SNOZZI



Date of birth: 28.01.1983

Nationality: CH

Laboratoire de Simulation en Mécanique  
des Solides (LSMS)  
École Polytechnique Fédérale de Lausanne  
Bâtiment GC - Station 18  
CH 1015 - Lausanne

Office: A2 475  
Phone: +41 (0)21 693 24 17  
Fax: +41 (0)21 693 63 40  
Email: leonardo.snozzi@epfl.ch  
Web: <http://lsms.epfl.ch>

### Current position

Since September 2008 Ph.D. student at LSMS under the direction of Prof. J.F. Molinari.

### Education

- 2007 Diploma in civil engineering (specialization in structures and hydraulic engineering), ETHZ, Zürich.
- 2002 High school Diploma, Liceo Lugano 1.

### Publications

#### Journal articles

- 1 Snozzi L., Gatuingt F. and Molinari J. F., *A meso-mechanical model for concrete under dynamic tensile and compressive loading*, International Journal of Fracture, 178(1-2):179–194, 2012.
- 2 Snozzi L. and Molinari J. F., *A cohesive element model for mixed mode loading with frictional contact capability*, International Journal for Numerical Methods in Engineering, Article in Press, 2012.
- 3 Gatuingt F., Snozzi L. and Molinari, J. F., *Numerical determination of the tensile response and the dissipated fracture energy of concrete: role of the meso-structure and influence of the loading rate*, International Journal for Numerical and Analytical Methods in Geomechanics, Accepted, 2011.
- 4 Snozzi L., Caballero A. and Molinari J. F., *Influence of the meso-structure in dynamic fracture simulation of concrete under tensile loading*, Cement and Concrete Research, 41(11):1130–1142, 2011.
- 5 Snozzi L. and Molinari J. F., *A multi-scale computational model to dynamic fracture of concrete*, In preparation for submission, 2012.

### Conference and seminar presentations

- 2012 *A Cohesive Element Model for Mixed Mode Loading Applied to Meso-Scale Concrete Specimens*. 8th European. Solid Mechanics Conference, Graz, Austria, 9–13 July, 2012.

- 2011 *Modelling of Brittle Material Fracture with Unilateral Frictional Contact at Contacting Interfaces*. International Conference on Computational Modeling of Fracture and Failure of Materials and Structures (CFRAC), Barcelona, Spain, 6–8 June, 2011.
- 2010 *Influence of the meso-structure in dynamic fracture simulation of concrete under tensile loading*, IV European Conference on Computational Mechanics (ECCOMAS), Paris, France, 16–21 May, 2010.
- 2010 *Influence of Meso-structure on the Dynamic Fracture Simulation of Concrete Under Tensile Loading*, Doctoral Conference in Mechanics, Lausanne, Switzerland, 19 February 2010.
- 2008 *Entwicklung eines nichtlinearen Balkenelements für die Push-over Analyse von Tragwerken unter Verwendung der eXtended Finite Element Methode*, Young Engineers' Symposium (YES), Fribourg, Switzerland, 2 October, 2008.

## Professional Activities

- 2007-2008 Scientific collaborator within research team Prof. M. Fontana, IBK, ETHZ, Zürich.
- 2007 Stage at Muttoni & Grignoli civil engineering office, Lugano.

## Teaching

- 2011 Teaching assistant in Computational Mechanics for Prof. Molinari, EPFL, Lausanne.
- 2010-2011 Teaching assistant in Mechanics for Prof. Molinari, EPFL, Lausanne.
- 2009-2010 Teaching assistant in Structural Analysis for Dr. Davalle, EPFL, Lausanne.
- 2007-2008 Steel Construction assistant for Prof. Fontana, IBK, ETHZ, Zürich.
- 2004-2007 Teaching assistant in Mechanics for Prof. Dual, Mazza and Kaufmann, IMES, ETHZ, Zürich.
- 2005-2006 Teaching assistant in Structural Analysis for Prof. M. Marti, IBK, ETHZ, Zürich.

## Advising

- 2010 Undergraduate project (Spring Semester): Schneuwly A. and Damario A., *Modélisation et simulation numérique appliquées au dimensionnement de barrages*, EPFL, Lausanne.
- 2009 Undergraduate project (Spring Semester): Gavanier G., *Cohesive element modeling at the meso-scale*, EPFL, Lausanne.

## Languages skills

Italian: mother tongue  
 French, German and English: fluent  
 Spanish: proficient

## Grants, honors and awards

- 2007 ETH Medaille (outstanding Diploma Thesis and Studies), ETHZ Zürich.